# Advancement of the Quantitative Blood Oxygenation Level-Dependent (qBOLD) MRI technique to improve clinical feasibility.

**Ahlam Abdullah Alzaidi, BSc,MSc**

**Doctor of Philosophy**

**University of Nottingham**

**2024**

## Abstract

Quantitative Blood Oxygenation Level Dependent (qBOLD) MRI offers a non-invasive method for measuring brain oxygenation, with potential applications in various neurological conditions. However, its clinical implementation has been hindered by methodological inconsistencies and challenges in standardisation. This thesis aims to address these obstacles and advance the clinical applicability of qBOLD techniques through three studies.

First, a comprehensive scoping review of the qBOLD literature was conducted. The review revealed four main qBOLD acquisition methods: multiparametric (mp-qBOLD), asymmetric spin echo (ASE), gradient echo (GRE), and gradient echo sampling of spin echo (GESSE). Notably, mp-qBOLD emerged as the most used technique, likely due to its easier implementation in clinical settings. However, significant variability in the reversible transverse relaxation rate ($R_2'$) measurements across different acquisition techniques was observed, highlighting the need for standardisation.

To address this variability and enable quality assurance, the second study focused on developing and validating a new qBOLD phantom using glass microspheres. A linear relationship between $R_2'$ contrast and glass bubble volume fraction was established, and the phantom demonstrated good reproducibility in construction and MRI measurements. Crucially, $R_2'$ measurements were consistent across different qBOLD acquisitions and MRI vendors and the phantom accurately replicated known in vivo $R_2'$ values for human brain tissue. However, challenges arose in matching the irreversible transverse relaxation rate ($R_2$) values to the human brain range.
tea

The third study explored a combined hyperoxia-BOLD and mp-qBOLD (hmp-qBOLD) approach to improve oxygen extraction fraction (OEF) estimation in a clinically translatable manner. This combined method overestimated OEF compared to an established technique, with values exceeding normal physiological ranges.

In conclusion, this thesis has made important contributions towards addressing key challenges to the clinical implementation of qBOLD imaging, laying a solid foundation for future advancements in quantitative oxygenation imaging and its translation to clinical practice.

## Acknowledgements

First and foremost, I extend my deepest gratitude to Allah, the Lord of the Worlds, for granting me the strength, patience, and knowledge to complete this PhD. This achievement would not have been possible without His endless blessings and guidance.

I would like to express my sincere appreciation to my main supervisor, **Dr. Nicholas Blockley**, for his unwavering support, mentorship, and encouragement throughout my PhD journey. My heartfelt thanks also go to my second supervisor, **Dr. Rafal Panek**, whose insightful feedback and invaluable contributions greatly shaped this work.

I am deeply grateful to my colleagues, **Colette Milbourn**, **Jawaher Alsaiari**, and **Euan Kirkpatrick**, for their support and companionship throughout this journey. I also extend my appreciation to the staff at the Sir Peter Mansfield Imaging Centre, particularly to **Jan Alappadan Paul**, for his assistance with MRI scanning.

I am profoundly grateful to my family for their love and encouragement. To my **parents**, **grandparents**, **sisters**, and **brothers**: thank you for believing in me. To my husband, **Fahad**, who stood by my side while navigating his own PhD journey - your support has been invaluable. And to my beloved daughter, **Sondos**, whose curiosity about my "science stuff" and excitement over my growing word count brought light to even the toughest days - you are my greatest inspiration.

I am also thankful to the University of Nottingham for providing excellent research facilities and to Taif University for its financial support.

Finally, I extend my heartfelt thanks to all the volunteers who participated in this study. Your contributions were essential to making this research possible.

## Table of Contents

## List of Tables

## List of figures

## List of Abbreviations

ASE: Asymmetric spin echo
BOLD: blood oxygen level dependent
CBF: cerebral blood flow
CBV: cerebral blood volume
CMRO2: cerebral metabolic rate of oxygen
$CO_2$: carbon dioxide
CSF: cerebral spinal fluid
DBV: Deoxygenated blood volume
dHb: Deoxyhaemoglobin
DSC: dynamic susceptibility contrast
$ETO_2$: end-tidal oxygen
fMRI: functional magnetic resonance imaging
FOV: field-of-view
GASE: GESEPI asymmetric spin echo
GESEPI: Gradient echo slice excitation profile imaging
GESFIDE: Gradient echo sampling of free induction decay and echo
GESSE: Gradient echo sampling of the spin echo
GM: grey matter
GRE: gradient-echo
HIV: human immunodeficiency viruses
IR: inversion recovery
MRI: magnetic resonance imaging
mp-qBOLD: multiparametric quantitative blood oxygen level dependent
O2: oxygen
OEF: oxygen extraction fraction

PET: positron emission tomography
qBOLD: Quantitative blood oxygen level dependent
$R_1$ : Longitudinal relaxation rate
$R_2$ : Transverse relaxation rate
$R_2^*$: Effective transverse relaxation rate
$R_2'$ : Reversible transverse relaxation rate
RF: radiofrequency
ROI: region of interest
SDR: static dephasing regime
SE: spin-echo
$T_1$:  Longitudinal relaxation time
$T_2$: Transverse relaxation time
$T_2^*$: Effective transverse relaxation time
$T_2'$: Reversible Transverse Relaxation Time
TE: echo time
TR: repetition time
TRUST: $T_2$ relaxation under spin tagging
WM: white matter
2D: two-dimensional
3D: three-dimensional

## Works Arising from this Thesis

**Journal Articles**

Alzaidi, A.A., Panek, R. and Blockley, N.P., 2024. Quantitative BOLD (qBOLD) imaging of oxygen metabolism and blood oxygenation in the human body: A scoping review. Magnetic Resonance in Medicine.

**Conference abstracts**

Alzaidi, A., Panek, R. and Blockley, N.P., Development of a quantitative BOLD phantom for validation of acquisition strategies. ISMRM Annual Meeting 2023, Toronto, Canada.

A.A. Alzaidi, R. Panek, Sebastian Rieger, Susan Francis, G.Hoffmann, S.Kaczmarz, N.Blockley. Preliminary data for using hyperoxia and multiparametric qBOLD to estimate the oxygen extraction fraction. 2023 ICP Network Meeting Utrecht.

## 1.Introduction

The human brain, despite constituting only about 2% of total body mass, consumes approximately 20% of the body's oxygen supply [1]. This high oxygen demand, coupled with the brain's limited capacity to store oxygen, necessitates efficient real-time oxygen extraction from arterial blood. The oxygen extraction fraction (OEF), which quantifies this process, serves as a key physiological parameter in brain energy metabolism and has emerged as a potential biomarker for various neurological conditions, including Alzheimer's disease [2], carotid steno-occlusive disease [3], and brain tumours [4]. Traditionally, measurement of OEF and the related cerebral metabolic rate of oxygen ($CMRO_2$) has been the domain of positron emission tomography (PET) using $^{15}O$-labeled radiotracers [5]. While PET remains the gold standard for OEF and $CMRO_2$ mapping, its widespread clinical application is limited by complex logistics, radiation exposure, and the need for an on-site cyclotron to produce short-lived $^{15}O$ isotopes.

The advent of functional magnetic resonance imaging (fMRI) and the discovery of the Blood Oxygenation Level Dependent (BOLD) effect by Ogawa, Lee, Kay, Tank [6] opened new avenues for non-invasive assessment of brain oxygenation. The BOLD effect arises from the different magnetic properties of oxygenated and deoxygenated haemoglobin, with the latter being paramagnetic and causing local magnetic field inhomogeneities that affect the MRI signal. Building on this foundation, quantitative BOLD (qBOLD) techniques have been developed to provide absolute measures of OEF and related parameters. qBOLD methods aim to separate the contributions of deoxyhaemoglobin concentration and blood volume to the measured BOLD signal, potentially offering a non-invasive, radiation-free alternative to PET for OEF quantification [7]. Despite its promise, the clinical implementation of qBOLD faces several challenges, including the need for standardisation across different acquisition methods, the development of reliable quality assurance tools, and the refinement of OEF estimation techniques. Addressing these challenges is crucial for advancing qBOLD towards routine clinical use.

## 1.1.Aims and Objectives

This thesis aims to contribute to the advancement of qBOLD techniques for clinical applications through three main objectives. First, to comprehensively map the current landscape of qBOLD research through a scoping review, identifying prevalent acquisition methods, analysis techniques, and clinical applications. This review will provide a critical foundation for understanding the state of the field and identifying areas requiring further development. Second, to develop and validate a novel phantom for qBOLD measurements, addressing the crucial need for standardised quality assurance tools. This phantom will enable reproducibility testing across different sites and scanners, a key step towards clinical implementation. Third, to explore a combined hyperoxia-BOLD and multiparametric qBOLD (mp-qBOLD) approach for improving OEF estimation. This novel combination aims to enhance the accuracy and reliability of OEF measurements in a clinically translatable manner.

## 1.2.**Thesis Outline**

The subsequent chapters are organised as follows:

Chapter 2 provides a thorough background on MRI principles and qBOLD theory. It covers fundamental concepts of MRI physics, including spin dynamics, relaxation processes, and pulse sequences. The chapter then delves into the theoretical underpinnings of qBOLD, explaining how the technique quantifies OEF and related parameters based on the BOLD effect.

Chapter 3 presents a systematic scoping review of qBOLD literature, providing a comprehensive overview of the state of qBOLD research and identifying key challenges and opportunities in the field.

Chapter 4 details the development of the qBOLD phantom, including its design, validation, and potential applications for quality assurance.

Chapter 5 explores the combined hyperoxia-BOLD and mp-qBOLD approach, assessing its potential for improving OEF estimation and discussing the challenges encountered.

Chapter 6 summarises the findings from all three studies (chapter 3,4,5), discusses their contributions to the field of qBOLD research, addresses the limitations of the work, and proposes directions for future research.

By addressing these objectives, this thesis aims to contribute to the ongoing efforts to advance qBOLD methodology towards clinical implementation. This work focuses on improving the standardisation, reliability, and accuracy of qBOLD techniques, which are crucial steps in developing qBOLD as a potential tool for non-invasive assessment of brain oxygenation.

# 2.Background

## 2.1.Magnetic Resonance imaging

### Origin of the MR signal

The nuclear spin is an intrinsic property possessed by specific atomic nuclei. Nuclei with an odd number of protons or neutrons exhibit a non-zero spin, which arises from the presence of unpaired protons or neutrons. These nuclei with a non-zero total spin possess a magnetic moment m. Although the nuclei spin property exists in certain elements such as hydrogen ($^{1}H$), fluorine ($^{19}F$) and carbon ($^{13}C$), almost all clinical images come from hydrogen nuclei due to their abundance in biological tissue. The magnetic moments of the protons are normally randomly orientated. However, in the presence of a static external magnetic field $B_0$, the protons align either with (parallel) or against (antiparallel) the external field. The preferred state of alignment is the one that requires the least energy: that is, parallel to $B_0$. Hence, more protons align with $B_0$ than against it, forming a net magnetization known as $M_0$ which is parallel to $B_0$ (Figure. 2.1.a). However, due to the proton's magnetic moment, the proton will also experience a torque perpendicular to its magnetic moment, μ, and to the magnetic field, $B_0$. The resulting movement is known as precession which is analogous to a gyroscope. The frequency of this precession, known as the Larmor frequency,
is given:

$$\omega_0 = \gamma B_0 \quad \textbf{Equation 2.1}$$

The Larmor frequency ($\omega_0$ in MHz) is dependent on the strength of the magnetic field ($B_0$) and the gyromagnetic ratio (γ) of the nuclei, where γ for hydrogen protons is 42.6 MHz/T.

### RF pulse and Excitation

When the spin ensemble aligns with $B_0$, their magnetic moments are distributed at random angles around that direction, only when the spin ensemble is perpendicular to $B_0$ can it be detected. To measure the spins precession and generate a signal, a radiofrequency pulse (RF) is applied perpendicular to $B_0$. By applying an RF pulse with a frequency matching the Larmor frequency of the protons, i.e. at the spins resonant frequency,  the net magnetisation $M_0$ can be "flipped" away from $B_0$ (Figure 2.1.a and c). The degree that the net magnetization (M) is tipped by the RF pulse is called the flip angle, which depends on the magnitude and duration of the RF pulse. For example, a 90-degree flip angle tips the magnetization completely from the longitudinal axis into the transverse plane. The application of the RF pulse has two main effects. First, to tip $M_0$, the longitudinal magnetization, into the transverse plane M. Second, this causes the protons to precess coherently or spin "in-phase" with each other.

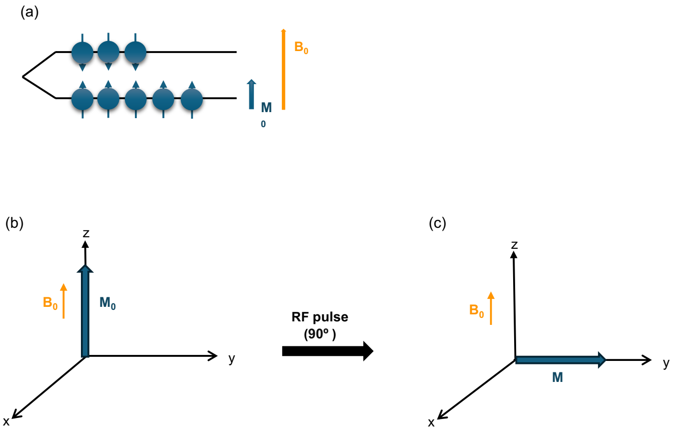

**Figure 2.1. Formation of the net magnetisation and excitation.** a) Illustration of the energy levels of the protons split into two due to the magnetic field $B_0$. b) Net magnetisation $M_0$ of the protons in the $B_0$ field. (c) Net magnetisation M after a 90° pulse is applied.

## Relaxation

After the RF pulse is switched off, the protons start to fall out of phase with each other and return to their original state in which the net magnetisation M aligns with $B_0$. This is driven by two processes. First, spin-lattice relaxation in which the longitudinal component of the magnetisation, M or ($M_z$), returns to it is initial magnitude $M_0$. The rate of this process is determined by the rate at which the water molecules tumble and rotate, and is expressed as,

$$\boldsymbol{M_z\,(t) = M_0\left(1 - e^{-\frac{TI}{T_1}}\right)} \quad \textbf{Equation 2.2}$$

where $T_1$ is the longitudinal relaxation time constant and TI is the inversion time.

The second process is known as spin-spin relaxation, which causes a decay in the transverse component of the magnetisation, $M_{xy}$. During this process, protons exchange energy with neighbouring spins. This is described by the transverse relaxation time constant, $T_2$, which is dependent on the local magnetic field $B_0$ and other tissue properties, known as the spin-spin interaction. The decay in the transverse magnetisation is expressed as,

$$\boldsymbol{M_{xy}\,(t) = M_0\, e^{-\frac{TE}{T_2}}} \qquad \textbf{Equation 2.3}$$

where $T_2$ is the transverse relaxation time constant and TE is the echo time.

However, spins are highly impacted by inhomogeneities in the magnetic field $B_0$, leading to a loss of phase coherence. This effect results in transverse relaxation decay with a shorter time constant called $T_2^*$. $T_2^*$ is a time constant that takes into account the effects of these inhomogeneities. The relationship between $T_2^*$ and $T_2$ is described in Equation 2.4, where $T_2'$ is the component of the $T_2^*$ signal decay caused by these magnetic field inhomogeneities.

$$\boldsymbol{\frac{1}{T_2^*} = \frac{1}{T_2} + \frac{1}{T_2'}} \qquad \textbf{Equation 2.4}$$

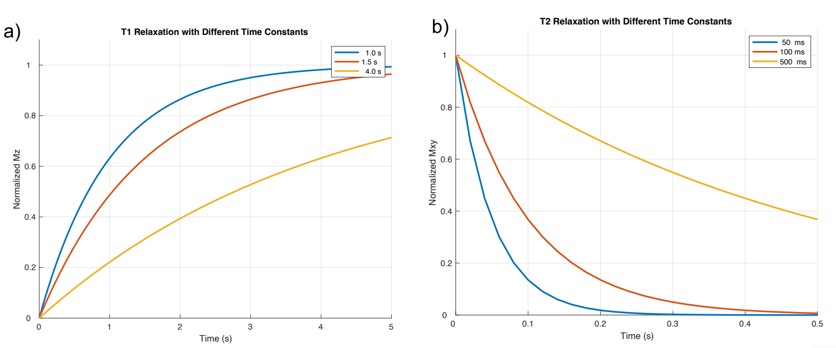

**Figure 2.2 Evolution of normalised Mz/Mxy caused by T1 and T2 relaxation.** Differences in magnetisation for different time constants are displayed using different colours**.**

### Free induction decay

When an RF pulse is switched off, $T_1$ and $T_2$ relaxation occur simultaneously and independently. As the protons continue to precess, the total magnetization vector follows a spiralling path, constantly changing in both direction and magnitude. As a result, an electric signal is produced which is measured by an MRI receive coil, and it results in a decreasing oscillation called the free induction decay (FID).

### Image formation

To form an image in MR, three magnetic field gradients are applied to localize and encode MR signals: the slice-selection gradient, the phase-encoding gradient, and the frequency-encoding gradient. This allows the MR signal to be pinpointed in three dimensions (x, y and z).

### Slice-selection gradient

To selectively excite a slice of a certain thickness, a gradient field known as the slice-selection gradient is applied along a chosen axis (for example z), which changes the strength of $B_0$ in that direction. This variation in $B_0$ strength causes the Larmor frequencies of protons in the gradient field to differ. Rather than using a single frequency, a narrow range of frequencies (bandwidth) is utilized to excite the slice. The thickness of the slice can be adjusted by changing both the RF pulse's bandwidth and the steepness of the gradient field. Once the slice has been selectively excited, spatial encoding within the slice is performed to localize the MR signal. This is done using gradients that encode phase and frequency.

**Phase encoding gradients**

Following the RF pulse, the protons spin in phase. When a new magnetic field gradient is applied, the speed of rotation of protons differs depending on their position in the gradient. After the gradient is turned off, all protons will precess at the same Larmor frequency again, but their phase will differ allowing them to be differentiated based on location. The gradient used is known as the phase encoding gradient. Typically, it is applied along the y-axis to induce linear changes in phase in that direction.

**Frequency encoding gradient**

A frequency-encoding gradient is applied throughout the readout time. This causes the protons to spin at different frequencies according to their position along the direction the gradient is applied. By doing so, the frequency-encoding gradient permits spatial localisation in a third axis (x).

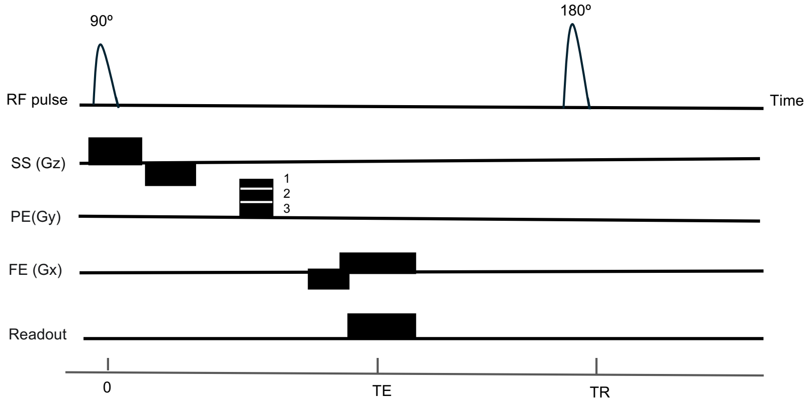

**Figure 2.3 Example MRI pulse sequence.** A slice-selective Gz gradient is applied simultaneously with a 90° excitation RF pulse. A Gy phase-encoding gradient blip then introduces a fixed phase shift along the y-axis. Following this, a frequency-encoding gradient (Gx) is applied, causing protons to precess at different Larmor frequencies depending on their position along the x-axis. By creating this spatial variation in precession frequencies, the Gx gradient enables spatial localisation

along the third axis (x) as the signal is collected at time TE. The sequence then repeats after time TR, with the amplitude of Gy changed in each repetition to increment the phase encoding gradient.

### K-space

K-space refers to a raw data matrix that stores the spatial frequencies of the image being acquired. Each K-space point contains spatial frequency and phase information about the image. In Figure 2.4 Kx represents the frequency encoding information, whereas Ky is the phase encoding data. Different areas of K-space hold different information about the resultant image. The centre of K-space provides the contrast of the image. On the other hand, the outer edges of K-space store information on the high spatial frequency characteristics of the image corresponding to small details in the image. The raw data in K-space is then transformed using the inverse Fourier Transform (FT) to create the final image by converting the data from the time domain to the spatial domain.

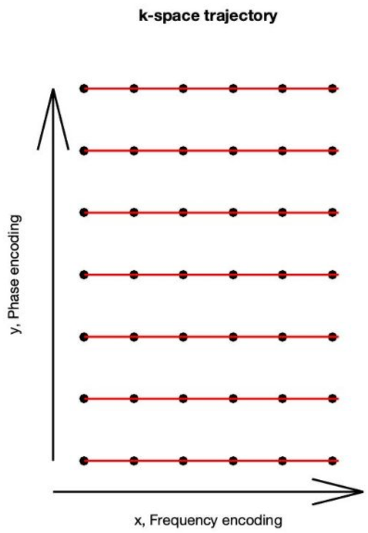

**Figure 2.4 The K-space trajectory.**

## Acquisition techniques: Pulse Sequence

Each MR image contrast uses a unique combination of radiofrequency pulses (RF) and magnetic field gradients to alter image contrast and acquisition time, depending on the sample being investigated. The following sections outline the fundamental MRI pulse sequences with a specific focus on sequences used in qBOLD acquisitions.

### Spin Echo

The conventional spin echo (SE) pulse sequence begins with a 90° RF excitation pulse followed by a 180° rephasing pulse, applied at time TE/2 (where TE is the echo time), which serves to refocus the spins, effectively eliminating the dephasing effects caused by magnetic field inhomogeneities. This refocusing results in the formation of a spin echo at time TE, which is then read out. Figure 2.5 shows an example single SE pulse sequence diagram.

The conventional SE pulse sequence can be used in one of two ways: single spin echo or multiple spin echoes per repetition time (TR) interval. Multiple spin echo sequences consist of two or more 180° rephasing pulses applied to produce multiple spin echoes per TR, allowing acquisition of multiple contrast weightings in a single scan. While SE sequences are robust against field inhomogeneities, they are limited by relatively long acquisition times. To address this, Fast Spin Echo (FSE) or Turbo Spin Echo (TSE) sequences were developed. These techniques employ a train of 180° refocusing pulses after a single 90° excitation pulse, acquiring multiple echoes per TR. Each echo fills a different line of k-space for a single image, significantly reducing scan time.

It is possible to quantify the relaxation rate ($R_2$) by obtaining a sequence of SE images with varying TE and fitting an exponential decay function of the form.

$$\boldsymbol{S(TE) = M_0 e^{-R_2 . TE}} \qquad \textbf{Equation 2.5}$$

where $M_0$ is the equilibrium state of magnetization.

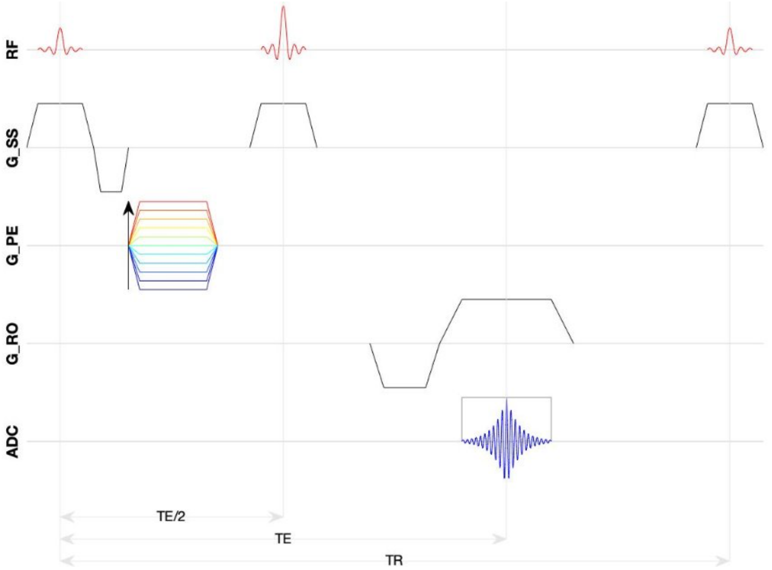

**Figure 2.5. Spin echo pulse sequence diagram.** G_SS (slice-selection gradient), G_PE (phase encoding gradients), G_FE (frequency encoding gradient), TE (echo time), TR (repetition time).

### Gradient Echo

The gradient echo (GRE) pulse sequence uses an RF pulse and magnetic field gradients with opposite polarity to rephase spins and produce an echo as opposed to the 180° pulse used in the SE pulse sequence. A GRE typically uses flip angles that are less than or equal to 90°. The optimal flip angle for maximizing SNR for a given $T_1$ and TR can be calculated using the Ernst angle formula:

$$\cos(\alpha) = e^{(-\frac{TR}{T1})} \qquad \textbf{Equation 2.6}$$

where α is the flip angle of the RF pulse. Using a lower flip angle allows for shorter TR times, as less longitudinal magnetization is tipped into the transverse plane, requiring less time to recover before the next excitation pulse. This can lead to faster acquisition times compared to SE sequences. While the signal from a single excitation might be lower due to the smaller flip angle, the ability to use shorter TR times can potentially improve the SNR per unit time. Figure 2.6 shows a basic sequence diagram for GRE pulse sequences. After an initial RF pulse is applied, a negative gradient pulse is used to dephase spins along the direction of the gradient. This dephasing causes a rapid decline in the FID signal. However, this loss of phase coherence can be reversed by applying a positive magnetic field gradient with a slope of equal amplitude but in the opposite direction to the first. This gradient causes the spins to move back into phase, resulting in a signal called a gradient echo. This bi-polar application gradient is usually performed by the frequency encoding gradient, enabling the spins to be rewound back into phase in the middle of the application of the positive lobe of the frequency encoding gradient when the system is reading out the echo.

Gradient rephasing is less effective than RF rephasing as it does not rephase the magnetic moment of the spins that are dephased due to magnetic field inhomogeneities. Hence, the signal from GRE is mainly dominated by the effect of $T_2$* and local magnetic field susceptibility ($T_2$').  Thus, the relaxation rate measured in the GRE sequence is the sum of both effects and can be expressed mathematically as:

$$\boldsymbol{\frac{1}{T_2^*} = \frac{1}{T_2} + \frac{1}{T_2^{'}} = R_2^* = R_2 + R_2^{'}} \qquad \textbf{Equation 2.7}$$

where the transverse relaxation rate $R_2$ is the inverse of the relaxation time $T_2$.

**GRASE**

Gradient and spin echo (GRASE) is a hybrid MRI pulse sequence that is a combination of gradient echoes and spin echoes. Typically, a 90° RF pulse is followed by a train of refocusing 180° pulses, but for each spin echo of the readout, there are additional gradient recalled echoes. The GRASE sequence benefits from combining both the scan time reduction of using a GRE, and RF compensation for magnetic field inhomogeneity from SE. The contrast achieved by the GRASE sequence is more like $T_2$ weighted MRI [8] and can be used to quantify $T_2$ in a time efficient way.

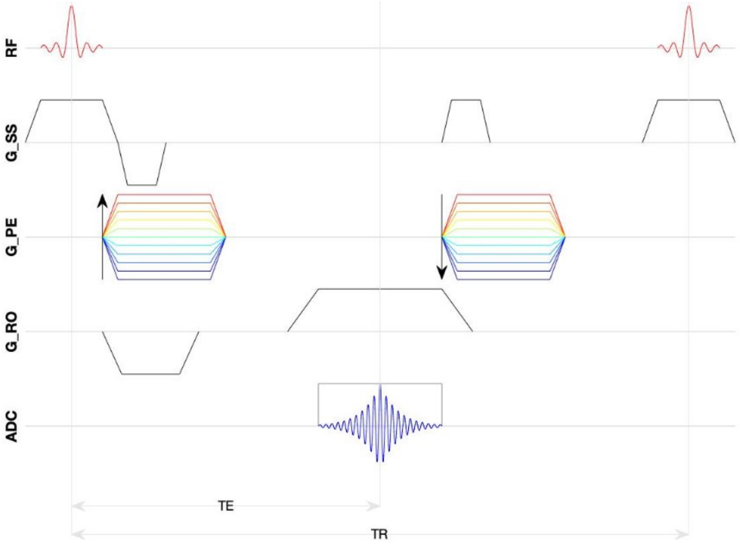

**Figure 2.6. Gradient echo pulse sequence.** G_SS (slice-selection gradient), G_PE (phase encoding gradients), G_FE (frequency encoding gradient), TE (echo time), TR (repetition time).

**GESSE and GESFIDE**

The gradient echo sampling of the spin echo (GESSE) sequence was proposed by Yablonskiy, Haacke [9] as a development of the gradient echo sampling of the FID and echo (GESFIDE) sequence by Ma, Wehrli [10]. By applying the GESSE sequence, it is possible to measure $R_2'$ and $R_2$ in one sequence.

GESFIDE is based on incorporating two sets of gradient echoes in a standard SE sequence to sample both the dephasing $R_2^*$ (before the 180° RF pulse) and rephasing $R_2$ (between the 180° RF pulse and the spin echo) components of the signal. Since $R_2' = R_2^* - R_2$, these measurements can be used to determine both $R_2'$ and $R_2$. A main drawback of this approach is that it sensitive to slice profile imperfection effects [9].

In contrast, the GESSE sequence consists of sets of gradient echoes acquired before and after the echo time of an SE sequence and hence does not suffer from slice profile imperfection problems. The signal can be sampled using both positive and negative gradients which provide the advantages of increasing the number of sampling points and the signal-to-noise ratio, but can lead to an apparent image shift between odd and even echoes. The signal decay before and after the spin echo is then used to compute the best-fitting $R_2$ and $R_2'$ values.

### ASE

Another way to measure $R_2'$ directly is by applying an asymmetric spin echo (ASE) sequence [11]. This approach is similar to an SE, but the timing of the 180° pulse is shifted relative to the readout time. This results in the spins coming back into phase at an effective echo time (TE + τ), where the refocusing pulse is displaced by τ/2. When the signal is acquired at TE, it can be written as,

$$S(T) = S_0 \, . \, e^{-R_2'.\tau} \, e^{-R_2.TE} \qquad \textbf{Equation 2.8}$$

where $S_0$ $S_0$ is the signal measured when τ=0 assuming a fixed TE. Because $R_2$ is constant, there is no need to subtract the $R_2$ contribution to the data, making this approach easier to fit.

### Inversion recovery pulse sequence

Inversion Recovery (IR) pulse sequence is a versatile MRI technique that can be used for various purposes, including $T_1$ measurement and tissue signal suppression. This is typically done by beginning with a 180° RF pulse to invert the longitudinal magnetisation (Mz). Then, there is a delay known as the inversion time (TI); during this time, the longitudinal magnetisation (Mz) of different tissues recovers at different rates according to their $T_1$ relaxation times. At the end of TI, a 90° RF pulse is applied to convert the recovered longitudinal magnetization into transverse magnetization, which can then be measured. For $T_1$ measurement, images are acquired at multiple TI values, allowing the plotting of signal recovery curves and calculation of $T_1$ values as:

$$s(TI) = M0\left(1 - 2\exp\left(-\frac{1}{(T1)}\right)\right) \quad \textbf{Equation 2.9}$$

For tissue suppression, a specific TI is chosen to null the signal from a particular tissue, as exemplified by FLAIR sequences where the CSF signal is suppressed in brain imaging.

## 2.2.Measuring the Oxygen Extraction Fraction

The brain is highly dependent on oxygen for its energy metabolism and has limited oxygen storage, making it highly vulnerable to hypoxia and ischaemia. Even a few minutes of interruption of oxygen supply to the brain can lead to irreversible damage to the brain if prompt intervention does not occur [12]. The oxygen extraction fraction (OEF) provides a direct and quantitative measure to assess the viability and function of brain tissue. When oxygenated blood passes through capillaries, it releases oxygen into the surrounding tissues. Hence, OEF represents the percentage of oxygen extracted by the tissue. Mathematically OEF is described as:

$$\boldsymbol{OEF} = \frac{\boldsymbol{Y_a - Y_v}}{\boldsymbol{Y_a}} \times \mathbf{100}\,\%, \qquad \textbf{Equation 2.10}$$

where $Y_a$ is the arterial oxygenation and $Y_v$ is the venous oxygenation, measured as the fraction of oxygenated haemoglobin ($HbO_2$, where $HbO_2$ refers to haemoglobin molecules bound with oxygen). In normal physiological conditions, $Y_a$ is around 98 % $HbO_2$ for healthy adults. Thus, OEF can typically be simplified as:

$$\boldsymbol{OEF} \approx \mathbf{1} - \boldsymbol{Y_v} \qquad \textbf{Equation 2.11}$$

$Y_a$ can be measured using a digital pulse oximeter, particularly in cases when abnormalities are anticipated such as in patients with respiratory disorders or severe anaemia. However, quantifying $Y_v$ is challenging due to the mixing of venous blood with blood from other regions and the risks associated with invasive measurement techniques such as jugular bulb oximetry [13].

In the bloodstream, oxyhaemoglobin and deoxyhaemoglobin have different magnetic properties. Oxyhaemoglobin is diamagnetic, while deoxyhaemoglobin is paramagnetic. When there is a higher concentration of deoxyhaemoglobin in the vessels, it causes a decrease in blood $T_2$ due to water diffusion and exchange, which is similar to the BOLD effect (more discussion about BOLD in the next section). The increased levels of deoxyhemoglobin also enhance the magnetic susceptibility of blood-containing voxels. The presence of paramagnetic deoxyhemoglobin creates field inhomogeneity, leading to further signal decay in the surrounding tissue. Moreover, changes in the BOLD signal during hypercapnic and hyperoxic gas inhalations can be interpreted based on deoxyhemoglobin levels. The non-linear relationship between deoxyhemoglobin concentration and MRI signal intensity enables the differentiation of various factors and the estimation of OEF and other physiological parameters. The OEF assessment methods mentioned in this thesis depend on the above-mentioned effects.

Once the OEF and arterial blood oxygenation are measured, it can be combined with the CBF to calculate the cerebral metabolic rate of oxygen consumption ($CMRO_2$) which refers to the oxygen metabolism of brain tissue and reflects the absolute value of the oxygen consumption of brain tissue. This can be calculated based on Fick's principle:

$$\boldsymbol{CMRO_2 = CBF \cdot (Y_a - Y_v) \cdot C_a \cdot [Hb] = CBF \cdot OEF \cdot Y_a \cdot C_a \cdot [Hb]} \quad \textbf{Equation 2.12}$$

The concentration of haemoglobin in the blood is represented by [Hb] and is measured in gram haemoglobin/dL blood e.g in the range 13–16 gHb/dL in males and 12–15 gHb/dL in females [14]. The oxygen-carrying capacity of haemoglobin is denoted by $C_a$ and is equal to 1.34 mL or 59.8 μmol $O_2$/gram haemoglobin. The expression $(Ya - Yv) \cdot C_a \cdot [Hb]$ is sometimes called the arterio-venous difference in oxygen content (AVDO2). Cerebral blood flow (CBF) can be measured using phase-contrast MRI to accurately assess blood flow in the arteries that supply the brain. Alternatively, arterial spin labelling (ASL) MRI can be employed to measure regional CBF.

Understanding the physiology and pathophysiology of OEF is crucial for interpreting its changes across various physiological and pathological conditions. OEF is intricately linked with CBF and $CMRO_2$ through their physiological relationships. Under normal resting conditions, healthy brain tissue maintains an OEF of approximately 30-40%, reflecting a balanced relationship between oxygen delivery and consumption. This relationship can be better understood through the oxygen-hemoglobin dissociation curve (Figure 2.7), which demonstrates how oxygen saturation varies with partial pressure of oxygen ($PO_2$).

**Commented [AA1]:** Comment 1.

**Commented [NB2]:** Don't forget to subscript 2s like this one throughout this paragraph and the thesis

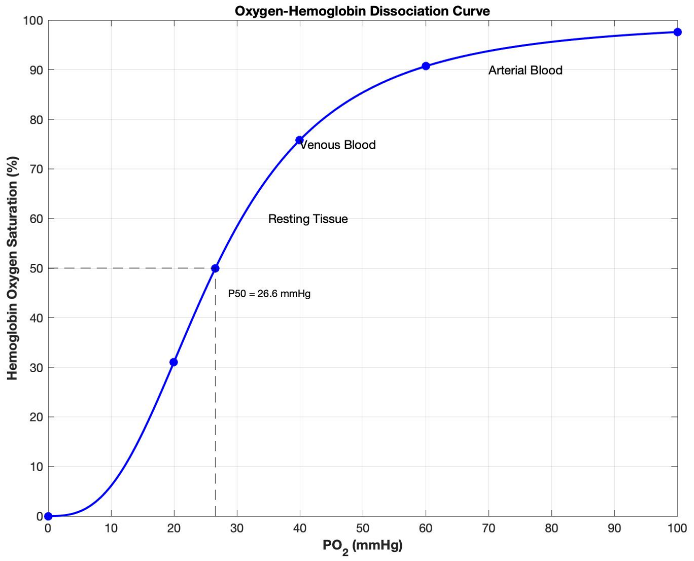

Figure 2.7. The oxygen-hemoglobin dissociation curve.

The oxygen-hemoglobin dissociation curve demonstrates the relationship between partial pressure of oxygen ($pO_2$) and haemoglobin saturation. The sigmoidal shape facilitates oxygen loading in lungs (high $pO_2$) and unloading in tissues (low pO2). This S-shaped curve is physiologically advantageous, allowing for efficient oxygen loading at the pulmonary level (arterial $pO_2$ ~95-100 mmHg) and optimal unloading at the tissue level (pO2 ~20-40 mmHg). Key physiological modulators such as pH, temperature, and $CO_2$ can shift this curve, affecting oxygen delivery to tissues.

During neural activation, a complex physiological response occurs where CBF increases disproportionately compared to $CMRO_2$. The initial response involves an increase in $CMRO_2$ by 15-20% to meet heightened energy demands, followed by a larger increase in CBF of 30-50% above baseline. This mismatch between flow and metabolism results in a counterintuitive decrease in OEF from the baseline 40% to approximately 30-35% during peak activation. This "luxury perfusion" represents an overcompensation mechanism ensuring adequate oxygen delivery during periods of increased neural demand.

In response to CBF challenges, OEF demonstrates remarkable adaptability. During hypercapnia (increased CO2 in blood), CBF increases substantially while metabolism remains stable, leading to a decrease in OEF. Conversely, during hypocapnia (decreased CO2), CBF reduces, causing an increase in OEF as the brain attempts to maintain adequate oxygen extraction from reduced blood flow.

In pathological conditions, particularly in cerebrovascular diseases, OEF changes become more significant. In acute ischemic stroke, as perfusion pressure declines and CBF drops to 30-50mL/100g/min, OEF increases from its baseline of 40% to 50-60%. This compensatory mechanism, known as "misery perfusion," maintains normal CMRO2 despite reduced CBF [15,16]. As CBF further decreases to 20-30mL/100g/min in the ischemic penumbra, OEF reaches values of 70-80%. This marked elevation in OEF allows tissue to maintain viability despite critically reduced perfusion. However, when CBF falls below approximately 20mL/100g/min and tissue pO2 drops below 20 mmHg, compensatory mechanisms fail despite maximal OEF, placing tissue at significant risk for infarction[16]. At this critical threshold, cells shift from aerobic to anaerobic metabolism, rapidly depleting energy reserves and triggering ischemic cascade pathways.

Conversely, in conditions such as gliomas, the relationship between CBF, OEF, and $CMRO_2$ can be more complex. Tumour tissues often exhibit increased $CMRO_2$ due to their high metabolic demands, but they may also have altered vascularization and perfusion [17]. In these cases, measuring the combination of CBF and OEF can help identify areas of increased oxygen metabolism, which can be useful for tumour grading and assessing treatment response [17,18].

The next section will discuss the BOLD signal, its origin, how it is employed in fMRI, calibrated BOLD and finally, the quantitative BOLD (qBOLD) method, which is the method used in this thesis.

### The BOLD signal

**Commented [AA3]:** Comment 2.

The BOLD signal was discovered in 1990 by Ogawa and colleagues [6,19,20] as an increase in $T_2$* with neural activation. Since then, it has been the mainstay of functional MRI (fMRI) studies [21] to map patterns of activation in the human brain during functional stimulation [22] or in the absence of an external stimulus (as in resting-state fMRI) [23,24].

Fundamentally, neural activation requires energy, and this is supplied through the vascular system by glucose and oxygen, which together are essential for the synthesis of adenosine triphosphate (ATP), the cells' energy currency in the human body. This process results in increased oxygen delivery by the vascular system to the region of neural activation [25]. The relationship between neural activity and the vascular response is characterised by neurovascular coupling, which is quantified by the neurovascular coupling constant n. This constant represents the ratio of the fractional change in cerebral blood flow (CBF) to the fractional change in cerebral metabolic rate of oxygen ($CMRO_2$), as defined in equation 2.13.

$$\mathbf{n = \frac{f-1}{m-1}} \quad \textbf{Equation 2.13}$$

where f is the normalized CBF and m is the normalized $CMRO_2$[26]. In healthy tissue, the coupling constant n typically ranges from 2 to 3, indicating that the blood flow response is considerably larger than the metabolic response. This disproportionate increase in blood flow relative to oxygen metabolism forms the fundamental basis of the BOLD contrast mechanism used in functional MRI. If n were equal to 1, the fractional changes in CBF and $CMRO_2$ would be exactly equal, resulting in no BOLD response, as the increased oxygen delivery would be precisely matched to increased oxygen consumption.

About 2% of the oxygen in the blood is dissolved in the plasma, and the rest is bound to haemoglobin (Hb) molecules within the red blood cells [27]. Hb is an iron-containing protein and has different magnetic properties depending on its oxygenation status. When oxygen molecules are bound to its haem protein, it is diamagnetic; whereas, when its oxygen has been released, the deoxyhaemoglobin (dHb) is paramagnetic [6,28].

When the oxygen in the capillaries is extracted by adjacent neurons from the blood plasma supporting the active neural tissue, more oxygen dissociates from Hb, leaving dHb behind. These changes in the local concentration of paramagnetic dHb lead to a change in local magnetic susceptibility, χ, which in turn affects the time constant of transverse dephasing of spins, $T_2^*$. A magnetic resonance acquisition protocol sensitive to $T_2$*, can then track local changes in the amount of dHb, which is the product of its concentration and the blood volume.

The magnitude of the BOLD signal is strongly dependent on magnetic field strength, with higher field strengths producing larger BOLD signals due to increased susceptibility effects. At 3T, which is now the most common field strength for fMRI studies, typical BOLD signal changes for standard motor or visual tasks are in the range of 1-4% in gray matter. This represents a significant improvement over 1.5T, where signal changes are typically 1-2%. The increased BOLD sensitivity at 3T arises from both the stronger susceptibility effects of deoxygenated blood and improved signal-to-noise ratio (SNR).

In functional MRI, neural activation leads to changes in CBF, $CMRO_2$, and CBV, with the CBF change much larger than the $CMRO_2$ change [29,30]. These changes result in a disproportionate increase in blood oxygenation. For instance, when the body responds to task-specific activation in healthy conditions by overcompensating with increased oxygenated blood flow to the relevant region of the brain, a local decrease in dHb concentration occurs. As deoxyhaemoglobin concentration reduces due to the increase of CBF and CBV, the $T_2^*$ increases, giving rise to the classic BOLD signal of an increase of a $T_2$*-weighed signal with neural activity. The temporal characteristics of this response are well-characterized, with a typical hemodynamic response function showing a peak response at 4-6 seconds post-stimulus, followed by a return to baseline over 12-15 seconds.

Mapping the BOLD signal as a local change in the $T_2^*$-weighted signal relative to the baseline is not a quantitative measurement; hence it cannot be compared directly between subjects, different sites and time [31]. This limitation arises from the complex relationship between the measured BOLD signal and the underlying physiological changes, which are influenced by baseline blood volume, haematocrit, and vessel geometry, among other factors.

**Calibrated BOLD**

One way to compensate for the lack of quantitative information offered in fMRI is the calibrated BOLD method which was first described by Davis, Kwong, Weisskoff, Rosen [32]. This was initially developed to provide quantitative measurements of essential physiological variables that would be comparable between subjects and sites.

The central idea for calibrated BOLD is measuring the maximum possible signal change denoted by the symbol M that would be done by eliminating all dHb from a voxel. This can be measured by manipulating CBF and $CMRO_2$, assuming that the change in CBV (ΔCBV) is tightly coupled with the change in CBF (ΔCBF) by Grubb's power law [33,34].

$$\Delta CBV = \Delta CBF^{\alpha} \qquad \textbf{Equation 2.14}$$

The exponent α value is assumed to be 0.38 based on early, whole-brain measurements in monkeys (Grubb Jr et al. 1974), but it has been quantified more recently in humans, applying hypercapnic and hypocapnic stimuli, with MRI, as 0.18. [34].

To manipulate CBF, a $CO_2$ inhalation experiment is performed, which causes hypercapnia, which in turn elevates CBF throughout the brain but is assumed to leave $CMRO_2$ unchanged. The resulting change to the measured BOLD signal ΔBOLD is described by the Davis model:

$$\frac{\Delta BOLD}{BOLD} = M\left(1 - \left(\frac{CBV}{CBV_0}\right)\left(\frac{[dHb]}{[dHb]_0}\right)^{\beta}\right) \qquad \textbf{Equation 2.15}$$

$[dHb]$ is the dHb concentration in veins, 0 indicates the baseline (normocapnic) state, and β depends on the diameter of the blood vessels where β=1 for large vessels and β=2 for small vessels. Investigation with Monte Carlo simulations to determine the correct β value for 1.5T suggested a value of 1.5 [32], with a lower value of 1.3 being use at 3T [35].The maximum possible BOLD signal change is given by:

$$M = A.TE.CBV_0.[dHb]_0^{\beta} \qquad \textbf{Equation 2.16}$$

Note that M depends on the magnetic field strength via parameter A, the pulse sequence through TE, the baseline of the physiological state of the blood volume ($CBV_0$), and the dHb concentration of the voxel.

Following both Grubb's power law and Fick's principle (described above) the complete form of the hypercapnia calibration model, including a term for metabolic changes, is thus given by:

$$\frac{\Delta BOLD}{BOLD} = M\left(1 - \left(\frac{CMRO_2}{CMRO_{2,0}}\right)^{\beta}\left(\frac{CBF}{CBF_0}\right)^{\alpha-\beta}\right) \qquad \textbf{Equation 2.17}$$

This model reveals the fundamental dependence of the BOLD signal on CBF, which is modulated by the maximum signal change (M) and CBF–CMRO$_2$ coupling. Because of the established relationship between end-tidal CO$_2$ and CBF [32], M can be calculated using a hypercapnic stimulus and acquired BOLD and ASL data. Then, when the neuronal activity or a change in physiology results in a change in CMRO$_2$, the change can be quantified in a way that is independent of other variables such as blood volume and oxygen saturation. It is based on the notion that all oxygen extracted from the vascular system by a specific voxel is metabolised locally (supplying the local CMRO$_2$) instead of transported out [32].

To quantify absolute changes in cerebral metabolism, rather than merely relative changes, another calibration is required. Whilst M is most commonly calculated using a hypercapnia experiment (Equation 2.14), a similar experiment can also be performed using hyperoxia induced changes in venous oxygen saturation [36] without significantly altering cerebral blood flow [37,38]. The relationship between the BOLD signal change during hyperoxia, CBF, and [dHb] is described by:

$$\frac{\Delta BOLD}{BOLD} = M\left(1 - \left(\frac{CBF}{CBF_0}\right)^{\alpha}\left(\frac{[dHb]}{[dHb]_0} + \frac{CBF_0}{CBF} - 1\right)^{\beta}\right) \quad \textbf{Equation 2.18}$$

By utilizing the hypercapnia M value and the known change in [dHb] from the hyperoxia experiment, derived from changes in partial pressure of end-tidal oxygen (PETO$_2$), [dHB$_0$] can be calculated. This approach enables a quantitative assessment of OEF.

Calibrated BOLD techniques are generally constrained by the demands for controlled gas delivery. The efficacy of gas delivery systems is crucial, asimproperly fitted masks or imprecise quantification of administered or end-tidal gas concentrations can introduce significant errors. Prolonged exposure to elevated CO$_2$ levels during the hypercapnic challenge cannot be sustained, and some studies have indicated that hypercapnia may induce changes in CMRO$_2$ [39] . Likewise, hyperoxia not only impacts oxygen saturation but also CBF [38], which can potentially undermine the accuracy of calibration using Equation 2.15.

### Quantitative BOLD

The quantitative BOLD (qBOLD) method seeks to measure physiological parameters such as OEF and deoxygenated blood volume (DBV) based on the transverse relaxation decay process without the need for gas challenges or an exogenous contrast agent. This was first proposed by Yablonskiy, Haacke [7] and, in broad terms, describes the signal evolution from two compartments. The bulk compartment refers to tissue, and the minor compartment represents several paramagnetic susceptibility-altering objects, such as blood vessels and red blood cells. An important parameter characterising the magnetic properties of all tissue is the magnetic susceptibility, χ, a proportionality constant between the tissue magnetisation M and the magnetic field strength $B_0$.

$$\boldsymbol{M = \chi . B_0} \qquad \textbf{Equation 2.19}$$

Due to the paramagnetic structure of haem complexes in deoxygenated red blood cells, the inclusion of a blood vessel network adds another decay mechanism for tissue-originated MR signals. This mechanism is caused by the inhomogeneous magnetic fields produced by the red blood cells in the blood and the inhomogeneous magnetic fields generated by the blood vessels in the surrounding tissue. In the qBOLD model, it is assumed that the blood vessels can be described as a set of randomly orientated cylinders which contain paramagnetic particles. This leads to an MR signal that can be characterised as

$$\boldsymbol{S(t) = \rho . (1 - \zeta) . e^{-\zeta . f(\delta\omega . t)}} \qquad \textbf{Equation 2.20}$$

where ρ is the spin density, ζ is the volume fraction of the cylinders and the function $f(\delta\omega . t)$ is defined as:

$$\boldsymbol{f(\delta\omega . t) = \frac{1}{3} \cdot \int_0^1 (2 + u) \cdot \sqrt{1 - u} . \frac{1 - J_0\left(\frac{3}{2} . \delta\omega . t . u\right)}{u^2} . du} \qquad \textbf{Equation 2.21}$$

where $J_0\,(\delta\omega\,.\,t)$ is the zero-order Bessel function, and $\delta\omega$ is the characteristic frequency shift induced by deoxyhaemoglobin.

Assuming that the arterial blood is fully oxygenated, then ζ represents the deoxygenated blood volume (DBV), with the understanding that the veins are typically the major contributor to ζ (sometimes also referred to as the venous blood volume) and $\delta\omega$ is the deoxyhaemoglobin-induced frequency shift, which corresponds to the change in nuclear precession frequency in the equatorial magnetic field of a red blood cell. This frequency shift arises due to the difference in magnetic susceptibility between deoxygenated and oxygenated haemoglobin, which creates local magnetic field inhomogeneities. It is described as [7],

$$\boldsymbol{\delta\omega = \gamma \,.\, \frac{4}{3} \,.\, \pi \,.\, \Delta\chi_0 \,.\, Hct \,.\, OEF \,.\, B_0} \qquad \textbf{Equation 2.22}$$

where $\gamma$ is the gyromagnetic ratio which is equivalent to 2.68 x $10^8$ rad/sec/Tesla, $B_0$ is the main magnetic field strength, Hct is the fractional haematocrit and is proportional to the haemoglobin concentration, Y is the blood oxygenation fraction, and $\Delta\chi_0$ is the susceptibility difference between fully deoxygenated and fully oxygenated blood that has been measured to be 0.27 ppm per unit Hct [40]. To obtain a quantitative measurement for OEF, δω must be extracted from Equation 2.17.

Yablonskiy and Haacke observed that Equation 2.17 has two asymptotic forms; namely short-time scale and a long-time scale.For the short-time scale, where data acquisition is within $t \leq 1.5\ t_c$ of the spin-echo formation, Equation 2.17 becomes:

$$\boldsymbol{S(t) = exp\ \left(\frac{3}{10} \,.\, \zeta \,.\, (\delta\omega . t)^2\right)} \qquad \textbf{Equation 2.23}$$

where $S(t)$ is normalised to the spin-echo signal $S(t = 0)$, and the characteristic time $t_c$ is dependent on $\delta\omega$ as

$$\boldsymbol{t_c = \frac{1}{\delta\omega}} \qquad \textbf{Equation 2.24}$$

In contrast, for a long-time scale, where $t \geq 1.5\ t_c$, the MR signal can be approximated as

$$\boldsymbol{S(t) = exp(\zeta)\ exp(-\zeta \,.\, \delta\omega . t)} \qquad \textbf{Equation 2.25}$$

During the short timescale of Equation 2.20, the signal decay is quadratically exponential, whereas in the long-time scale in Equation 2.22 it is linearly exponential. From this long timescale, it is possible to characterise the rate of reversible dephasing $R_2{}'$ as

$$\boldsymbol{R_2' = \zeta \,.\, \delta\omega} \qquad \textbf{Equation 2.26}$$

Substituting in Equation 2.19 gives

$$\boldsymbol{R_2' = \gamma \cdot \frac{4}{3} \cdot \pi \cdot \Delta\chi_0 \cdot Hct \cdot OEF \cdot B_0 \cdot \zeta} \qquad \textbf{Equation 2.27}$$

It is therefore possible to re-write Equation 2.20 and 2.22 in terms of $R_2'$ and $\zeta$ as:

$$\boldsymbol{S(t) = exp\left(\frac{3}{10} \cdot \frac{(R_2'.t)^2}{\zeta}\right) \qquad t \leq \frac{1.5.\zeta}{R_2'}} \qquad \textbf{Equation 2.28}$$

$$\boldsymbol{S(t) = exp(\zeta)\, exp\,(-R_2'.t) \quad t \geq \frac{1.5.\zeta}{R_2'}} \qquad \textbf{Equation 2.29}$$

OEF can be recovered by solving Equation 2.24:

$$\boldsymbol{OEF = \frac{3 \cdot R_2'}{4 \cdot \gamma \cdot \pi \cdot \Delta\chi_0 .Hct .B_0 .\zeta}} \qquad \textbf{Equation 2.30}$$

The model described above is based on several assumptions. First, the static dephasing regime for MRI signal formation in the presence of the blood vessels network assumes the diffusion effect is negligible. However, this assumption may not be applicable for capillaries, and hence, the measured $R_2'$ is possibly lower than predicted by Equation 2.19. According to Kiselev, Posse [41] and Fujita, Shinohara, Tanaka, Yutani, Nakamura, Murase [42], water diffusion may play a significant role in producing extravascular MR signals from the capillary network, mainly when extended SE durations are utilised. Several studies have proposed methods to account for this issue, including new qBOLD models such as the alternative dephasing model proposed by Kiselev, Posse [41]. In their model, they account for both the static dephasing regime and the diffusion narrowing regime. The advantage of such a model is the potential to dissociate the effect of OEF and DBV in the short-time regime [43]. Other authors have also used the Gaussian phase approximation [44] and a phenomenological model derived from simulated data [45].

The second assumption relates to describing the brain tissue as a one component structure. In fact, it is known that the brain tissue displays multicomponent MR behaviour. For instance, a voxel may contain both cerebral spinal fluid (CSF) and grey matter, where both have a significantly different $R_2$, which in turn, will result in a biexponential decay. Additionally, the intravascular effect is ignored in this simple model, despite the fact that it contributes significantly to the BOLD signal at 3.0 T and lower [31]. Although, recent simulations suggest that for Asymmetric Spin Echo (ASE) sequences, the intravascular effect may have minimal impact on the BOLD signal (Stone et al., 2019b).

## Validation studies

Several studies have been conducted to validate the qBOLD model in a range of conditions. At first, Yablonskiy [46] used a phantom vascular network to quantify volume fraction (equivalent to DBV) and $R_2$' consistently using GESSE qBOLD. Later, Sedlacik, Reichenbach [47] conducted similar phantom experiments and demonstrated OEF and DBV with in vivo measurements in healthy subjects. They found that although estimating OEF and DBV simultaneously was unreliable, by setting one of the parameters to a physiologically reasonable value, the other parameter can be estimated correctly.

He, Zhu, Yablonskiy [48] assessed qBOLD estimations of OEF in rats versus oxygen saturation measurements obtained using a blood gas analyser, showing a significant correlation between the two measures.

In 2015, [4948484848485150494848]Ni and colleagues conducted a comparison study of $R_2$' methods, including GESSE and ASE which are both utilized in the qBOLD literature [50-52]. They reported differences in grey matter $R_2$' estimations between methods, with GESSE resulting in a lower $R_2$' estimation.

## Other qBOLD approaches

Including further information has been shown to enhance model fitting. An, Lin [53] demonstrated that $B_0$ inhomogeneities resulted in an overestimation of $R_2$' , but that this effect could be minimised by a retrospective correction approach such as using a field map. This was extended to a prospective correction approach in the streamlined qBOLD technique using the gradient echo slice excitation profile imaging (GESEPI) technique [51].

In addition, Christen and colleagues have demonstrated the possibility of using arterial spin labelling and dynamic susceptibility contrast methods to obtain measurements of CBF and CBV, then combine these results with $R_2^*$ and $R_2$ measurements to derive maps of OEF and $CMRO_2$ . This method, termed multiparametric qBOLD, was validated against other qBOLD approaches in healthy volunteers. It is theoretically less sensitive to diffusion effects, owing to the short echo time needed to determine $R_2^*$ [54] . However, it depends on the same assumptions as the SDR qBOLD model.

The development of rapid OEF mapping techniques addresses a critical unmet need in acute stroke care. Current standard stroke imaging protocols in the UK typically include non-contrast CT to rule out haemorrhage, followed by CT perfusion or MR diffusion-weighted imaging (DWI) and perfusion-weighted imaging (PWI) to identify potentially salvageable tissue. While these methods provide valuable information about tissue perfusion and irreversibly damaged tissue, they do not directly measure tissue oxygen metabolism, which could provide crucial additional information about tissue viability.

**Commented [AA4]:** Comment 3.

The time-sensitive nature of acute stroke treatment, where "time is brain", necessitates rapid imaging protocols. The current 4.5-hour window for intravenous thrombolysis and 6-hour window for mechanical thrombectomy in standard practice highlight the critical importance of quick decision-making. Traditional OEF measurement techniques, such as 15O-PET, are impractical in this setting due to their lengthy acquisition times and complex logistics. Therefore, a fast OEF mapping technique that could be integrated into existing stroke protocols could potentially improve patient selection for acute interventions by providing direct information about tissue metabolic status.

Beyond the hyperacute stroke setting, where acquisition speed is less critical, quantitative OEF measurements offer several potential clinical applications. In chronic cerebrovascular disease, such as carotid stenosis, OEF mapping could help identify patients at increased risk of stroke due to compromised cerebral hemodynamic. This information could guide decisions about preventive interventions such as carotid endarterectomy. In neuro-oncology, OEF measurements could provide insights into tumour metabolism and oxygenation status, potentially aiding in treatment planning and monitoring response to therapy.

Another approach to advancing qBOLD techniques is to combine qBOLD with quantitative susceptibility mapping (QSM). This method is beneficial because the QSM, which is highly repeatable [55], may be used to regularise the less robust qBOLD reconstruction [56].

These approaches represent ongoing efforts to refine qBOLD techniques and address the limitations of the basic model. A more comprehensive discussion of these and other qBOLD variants, including their strengths, limitations, and clinical applications, will be presented in the following chapter, which provides an extensive scoping review of the current state of qBOLD research.

# 3. Quantitative BOLD (qBOLD) imaging of oxygen metabolism and blood oxygenation in the human body: A scoping review

This chapter presents a systematic scoping review of the qBOLD technique in MRI. It aims to comprehensively analyse qBOLD acquisition methods, processing techniques, and clinical applications reported in the literature. The review identifies recent practices, trends, and clinical evidence, offering insights into the evolving methodologies and potential of qBOLD in both research and clinical settings.

## 3.1.Introduction:

Baseline oxygen metabolism and blood oxygenation are thought to be affected in a variety of diseases. The gold standard technique for mapping oxygen metabolism is triple oxygen positron emission tomography (PET), which utilizes $^{15}$O-labelled $H_2O$, $O_2$ and CO to measure oxygen extraction fraction (OEF), cerebral blood flow (CBF) and cerebral metabolic rate of oxygen consumption ($CMRO_2$) [2,5]. PET studies using this technique have shown metabolic changes in ageing [57] , dementia [58], and Alzheimer's disease [2]. However, the complicated logistics, radiation exposure, and requirement for an onsite cyclotron to create the $^{15}$O isotope, which has a short half-life of 2 minutes, have limited its broad clinical usage [59] .

In recent years, advanced MR techniques have been developed to quantify baseline oxygen metabolism. Some of those techniques are based on respiratory calibration of the BOLD signal [60,61], whereas other non-respiratory techniques include $T_2$-based methods [62,63], susceptibility based methods [64-66] and quantitative BOLD (qBOLD) and $R_2$' (reversible transverse relaxation rate) mapping [52,67]. Some of these techniques try to estimate oxygen metabolism in specific brain regions, while others provide a global or whole-brain assessment of oxygen metabolism and have been discussed broadly in a recent review [59], which provides an overview of all MRI-based OEF measurements. However, this review is distinct in two ways. Firstly, the scoping review is a methodology to "systematically map the literature available on a topic, identifying key concepts, theories, sources of evidence and gaps in the research" [68]. Secondly, this review focuses specifically on the quantitative BOLD technique for mapping OEF and $R_2$' for assessment of relative tissue oxygenation rather than OEF measurement techniques in general.

### qBOLD theoretical underpinning

The qBOLD technique establishes a relationship between OEF and the observed MRI signal [7], and has been shown to be a valid approach for estimating blood oxygenation in preclinical studies [48] and healthy human subjects [47]. More recently it has been used in investigating patients with stroke [43,51] and glioma [69].

The qBOLD model focuses on signal decay in the “extravascular” tissue space caused by local magnetic field inhomogeneities surrounding the blood vessel network and induced by paramagnetic deoxyhaemoglobin. Traditionally, models of the BOLD signal are unable to separate the contributions of blood oxygenation level (i.e., OEF) and blood volume to the transverse signal decay. Therefore, a faster BOLD signal decay (i.e., a greater value of $R_2'$) might be caused by either decreased blood oxygenation or increased blood volume. However, Yablonskiy and colleagues developed a model of the BOLD signal in the static dephasing regime (SDR), by modelling the blood vessels as a network of randomly oriented cylinders. This SDR model has the advantage of being able to separate experimentally the oxygenation and blood volume effects. Particularly, two asymptotic equations can be derived to describe the signal behaviour in the short and the long-time scales [7,46,51]:

$$\boldsymbol{S_s = S_0\, exp(-TE \cdot R_2)\, exp\left(-0.3 \cdot \frac{(R_2' . \tau)^2}{DBV}\right) \qquad \tau < \frac{1.5\, DBV}{R_2'}} \qquad \textbf{Equation 3.1}$$

$$\boldsymbol{S_L = S_0\, exp(-TE \cdot R_2)\, exp(-\tau \cdot R_2')\, exp(DBV) \qquad \tau > \frac{1.5\, DBV}{R_2'}} \qquad \textbf{Equation 3.2}$$

where $\tau$ is defined as the *spin echo displacement time* which controls the $R_2'$-weighting of the signal, TE is the echo time and $R_2$ is the irreversible transverse relaxation rate. DBV represents the deoxygenated blood volume with the understanding that the veins typically are the major contributor to it. During the short timescale of Equation 3.1 the signal decay is quadratically exponential, whereas in the long-time scale in Equation 3.2 it is linearly exponential. From this long timescale, it is possible to characterise $R_2'$ ($R_2' = R_2^* - R_2$) as,

$$\boldsymbol{R_2' = DBV \cdot \gamma \cdot \frac{4}{3}\pi \cdot \Delta\chi \cdot Hct \cdot OEF \cdot B_0} \qquad \textbf{Equation 3.3}$$

where $\gamma$ is the gyromagnetic ratio ($2.68 \times 10^8$ rad/s/T), $B_0$ is the main magnetic field strength, Hct is the fractional haematocrit, and $\Delta\chi$ is the susceptibility difference between fully deoxygenated and fully oxygenated blood (0.27 ppm per unit Hct [40]).

Therefore, measurements of $R_2'$ are proportional to deoxyhaemoglobin content i.e. the product of haematocrit and OEF. DBV can be calculated via comparison of the measured signal at the short timescale $S_{s(\,meas)}$ with the intercept extrapolated from long timescale data $S_{L(extrap)}$ using Equation 3.4.

$$\boldsymbol{DBV = ln\, S_{L(extrap)}\,(0) - \;ln\, S_{S(meas)}\,(0)} \qquad \textbf{Equation 3.4}$$

Therefore, when $R_2'$ and DBV are known, OEF can be estimated from Equation 3.3.

To assess OEF using the qBOLD model, many studies have used a Gradient Echo Sampling of Spin Echo (GESSE) sequence, in which multiple gradient echoes are obtained with varying values of $\tau$ [46] . However, one disadvantage of this sequence is that the $R_2$-weighting of the gradient echo signals also varies with $\tau$ and must be taken into account when estimating $R_2'$ [52,53,67]. The Asymmetric Spin Echo (ASE) sequence in which the refocusing pulse of a spin echo pulse (SE) sequence is shifted by $\tau$ /2 to produce various degrees of $R_2'$-weighting while keeping the TE constant has also been used. This enables $R_2'$ to be estimated directly without the confounding effects of $R_2$-weighting. Both the GESSE and ASE methods require roughly 5-10 minutes to map the OEF [50]. Since the qBOLD model relies on small differences in the signal decay to distinguish the DBV and OEF effects (Equation 3.1 and 3.2), a high signal to noise ratio (SNR) is required to estimate them from GESSE or ASE data [46,47,70]. To overcome this issue, the multiparametric-qBOLD (mp-qBOLD) approach was devised, in which CBV is evaluated using dynamic susceptibility contrast (DSC) MRI and $R_2'$ is estimated by separately mapping $R_2$ with a multiple spin-echo sequence and $R_2^*$ with a multi-echo GRE sequence [54,71]. Nonetheless, the CBV measured by DSC is the total CBV, not the DBV required for qBOLD. As a result, the OEF produced by mp-qBOLD is a relative measure of OEF [71,72].

The qBOLD model described in Equations 3.1 and 3.2 considers a single extravascular tissue compartment and assumes that $R_2'$ is only associated with deoxygenated blood. However, $R_2'$ is susceptible to macroscopic magnetic field inhomogeneity, which must be addressed either prospectively with techniques like z-shimming [73] or the use of exponential excitation pulses [74], retrospectively with a high-resolution field map or by modelling the voxel spread function [52,75,76]. If not, then $R_2'$ will be increased leading to an overestimation of OEF.

Other compartments, such as intravascular blood and cerebral spinal fluid (CSF) or interstitial fluid (ISF), can be found in an in vivo imaging voxel, in the latter case resulting in an increase in $R_2'$. He and Yablonskiy explain the CSF effect as being caused by its differing protein and lipid content with respect to tissue, resulting in frequency shifts and phase differences in its MR signal relative to the tissue component [52]. To address this, the qBOLD model was expanded to include contributions from GM, WM, CSF, and blood [52]. However, implementing this multi-compartmental model demands prior tissue composition knowledge and involves a large number of fitting parameters [52]. Otherwise, to simplify the model, it is possible to reduce the contributions from other compartments. For instance, it has been proposed that the intravascular contribution can be minimised by employing flow crushing gradients [50], and the CSF/ISF signal suppressed utilising a Fluid Attenuated Inversion Recovery (FLAIR) preparation pulse [51]. Another key assumption of the qBOLD model is SDR for MRI signal formation in the presence of the blood vessels network which assumes the diffusion effect is negligible. However, it has been demonstrated that diffusion has a vessel size-dependent effect on signal decay, and that disregarding this effect may result in systematic underestimation of OEF[77-79].

### Aims of the review

To the best of our knowledge, there is no systematic review detailing the breadth of qBOLD acquisition, processing methods and clinical applications that have been presented and used in the literature. Therefore, the aim of this study is to perform a systematic scoping review of papers which employ the qBOLD technique. We present an overview of the different aspects of the qBOLD experiments reported and applied in the literature, describing the methods and clinical research applications. We classified and analysed the acquisition, data processing and populations employed and based on these findings we identified recent practices, trends, technical findings and evidence from clinical studies.

## 3.2.Methodology

A scoping review is defined as an exploratory project that aims to rapidly map the literature available on a subject and can be implemented when a certain subject or area is complex or not extensively reviewed in previous studies [80]. This approach differs from the systematic reviews because authors do not typically assess the quality of included studies [81,82], they also differ from the literature reviews in that the scoping process needs analytical reinterpretation [83]. Researchers can undertake a scoping study to meet various objectives, including examining the extent, nature, and range of research activities in a specific area, determining the value of undertaking a full systematic review, identifying the research gap, and summarising and disseminating the research finding [68]. Moreover, scoping studies can be valuable tools to investigate how research is conducted on a particular topic. Therefore, the evidence on the applications of the qBOLD approach in the literature was mapped in this systematic scoping review, in order to reveal the depth and breadth of that topic. These findings are reported based on the Preferred Reporting Items for Systematic Review and Meta-Analysis Extension for Scoping Review (PRISMA- ScR), which also guided the protocol for this scoping review [84].

### Search strategy

A systematic search was performed in the following databases: Medline, Embase and Web of Science. The search strategy combined terms relating to “quantitative BOLD”, “qBOLD”, “oxygen extraction”, “oxygen extraction fraction”, “oxygen saturation”, “oxygen metabolism”, “magnetic resonance”, “MRI”, “MR imaging”, “MR measurements”, and “Quantitative measurements of cerebral blood oxygen”. The search was constrained to English-language literature and date of publication from 1994, the year in which the theory underlying qBOLD was first reported [7]. Full details of the search strategy are provided in the Appendix (A). The last updated search was conducted in August 2023.

### Eligibility criteria

The following inclusion criteria were applied: studies that have been conducted on humans including healthy volunteers or patients. Studies that reported measurement outcomes of oxygenation using qBOLD such as deoxyhaemoglobin concentration, deoxyhaemoglobin content, oxygen extraction fraction or OEF, oxygenation, oxygen saturation, $R_2'$. Studies which only report $T_2'/R_2'$ were also included. $T_2'$ is the reversible transverse relaxation time which is the inverse of $R_2'$ i.e., $T_2'= 1/R_2'$. A decrease in $T_2'$ indicates an elevation in deoxyhaemoglobin which is equivalent to an increase in $R_2'$. As shown by Equation 3.3 , $R_2'$ is proportional to the product of OEF and CBV.

The following exclusion criteria were used: calibrated BOLD or dual calibrated FMRI or $QUO_2$ using hypercapnia and/or hyperoxia, $T_2$ Relaxation Under Spin Tagging (TRUST), Susceptibility Based Oximetry (SBO), VAscular Space Occupancy (VASO), Velocity-selective Excitation with Arterial Nulling (VSEAN ), Quantitative Imaging of eXtraction of Oxygen and TIssue Consumption (QUIXOTIC), reviews, simulation studies and preclinical studies.

### Selection of sources of evidence

The search records from the three databases were transferred to the Endnote (Clarivate, Philadelphia, PA) reference tool, where duplicates were identified and removed. Records were then screened by title and abstract by two researchers (A.A., N.B.). The included studies were transferred to the Rayyan software tool (Rayyan Systems, Inc., Cambridge, MA) and screened independently by title and abstract according to the inclusion and exclusion criteria by two researchers (A.A., N.B.). Disagreements were resolved by consensus. Two researchers (A.A., N.B) went through the full text of the included papers in a second step checking for their eligibility for final inclusion.

### Data charting

Data were extracted from each of the selected articles and tabulated. The following characteristics were extracted: study characteristics, such as: author, year, methods, and aim/objective of the study; population characteristics, including sample size, age, pathology. MRI acquisition parameters were recorded including magnetic field strength and type of pulse sequence. The technique for measuring CBV and OEF were documented. Finally, information on the analysis was extracted. Data extraction of all included studies was performed by the lead author (A.A.) and a sample of these data were checked by the senior author (N.B.).

## 3.3.Results

### Study selection and population characteristics

The electronic search of the three databases retrieved 5,172 studies of which 2,469 studies remained after checking for duplicates. After screening of abstracts and full texts for eligibility, 119 studies remained for full-text assessment according to the inclusion and exclusion criteria. Finally, 93 studies met the inclusion criteria and were included in the scoping review. Figure 3.1 presents a Prisma Flow Diagram illustrating the search results [85]. The studies included a total of 3,239 participants, comprised of 1,809 patients and 1,432 healthy participants. Twelve papers did not provide any age information, a further 34 papers reported only the age range. The mean participant age, computed as the group mean weighted by the number of participants in each study, was 43.3 years for healthy participants, while for patients it was 53.1 years.

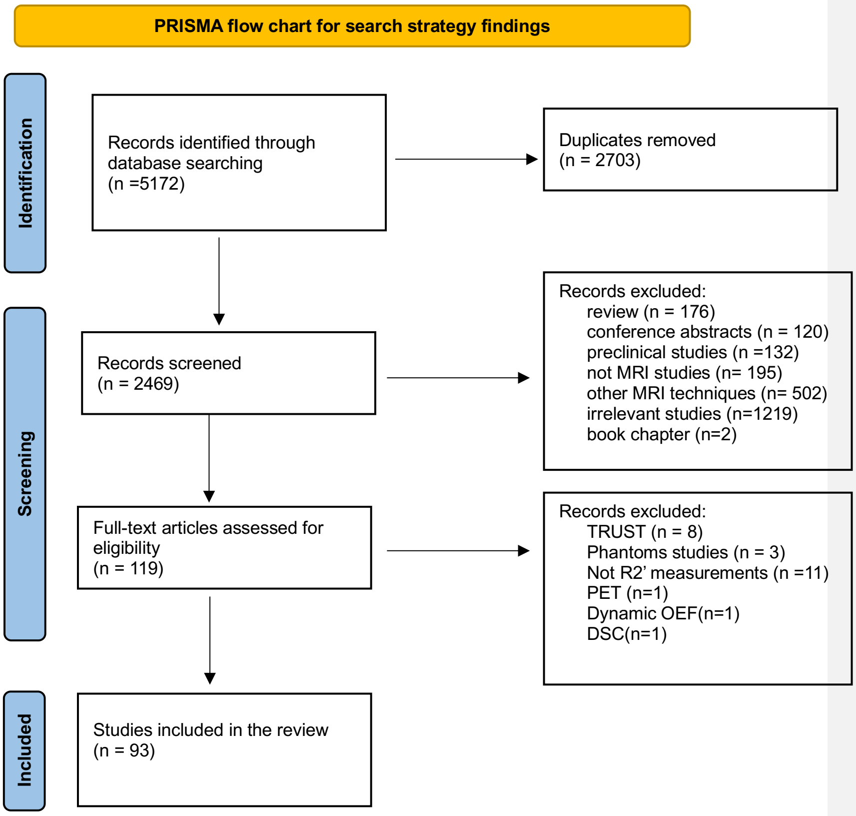

**Figure 3.1. PRISMA flow chart for search strategy findings.**

### Acquisition and Analysis

The number of included studies that were conducted at 3T is 78/93, where the remainder were acquired at 1.5T (15/93). In this review we identified many studies of qBOLD with different names such as qBOLD, multiparametric qBOLD (mqBOLD), quantitative susceptibility mapping combined with qBOLD (QQ), interleaved (iqBOLD) and streamlined qBOLD (sqBOLD). Despite the fact these techniques have different names, some of them are based on the same or similar acquisition methods. Thus, categorising the included studies based on acquisitions methods revealed 4 main acquisition methods: multiparametric acquisitions (mp-qBOLD) consisting of separate acquisitions of $R_2$* and $R_2$, which is the most common approach in the literature (36 studies) and has been applied in a slightly diverse way regarding the pulse sequence applied and the approach for measuring CBV; followed by ASE (21) which has been applied mainly using the basic ASE pulse sequence, and other branches pulse sequences of ASE, such as MASE used in one study and GASE in two studies; gradient-echo (GRE) (19); GESSE (12); spin and gradient echo (SAGE) (2); and gradient-echo sampling of free induction decay and echo (GESFIDE) (2) (see Table 3.1 for a full reference list and Figure 3. 2). Median and range of MRI parameters of the most common qBOLD acquisitions are presented in Table 3.2. On the clinical side, the most commonly used acquisition is the multiparametric approach, specifically mp-qBOLD (GRE and SE), followed by ASE, GRE, GESSE and mp-qBOLD (GRE and Gradient and spin-echo (GRASE)), then mp-qBOLD (SE and Echo planar imaging (EPI)), and finally SAGE.

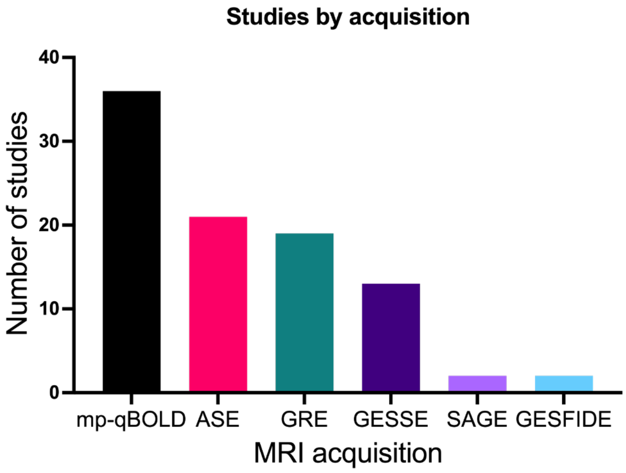

**Figure 3.2 Studies by acquisitions.** Acquisitions used for acquiring qBOLD data by number of studies mp-qBOLD: multiparametric qBOLD, ASE: Asymmetric spin

echo, GRE: Gradient echo, GESSE: Gradient Echo Sampling of Spin Echo , SAGE: spin and gradient echo, GESEFIDI: a gradient-echo sampling of free induction decay and echo.

| **Pulse sequence** | **Number of studies** | **CBV/DBV via** |
|---|---|---|
| | References | |
| | ***mp-qBOLD*** | |
| **Multi gradient echo /multi spin echo** | 15 [18,53,54,69,86-96] | DSC[18,53,54,69,86-96] |
| **Multi gradient echo /Fast-spin echo** | 4 [97-100] | DSC[100] |
| Multi-gradient echo /Gradient and Spin Echo (GRASE) | 7 [71,72,101-105] | DSC[71,72,101-105] |
| **Gradient echo-EPI/Fast-spin echo** | 6 [106-111] | DSC[109] |
| Multi gradient echo/Fast-multi spin echo | 2[112,113] | - |
| **Fast-gradient echo /Fast-spin echo** | 2[114,115] | - |
| | ***ASE*** | |

| | | |
|---|---|---|
| **ASE** | 11 [51,116-126] | Yablonskiy and Haacke qBOLD model[7] |
| Triple-echo ASE | 4[127-130] | Yablonskiy and Haacke qBOLD model[7] |
| **Multi-echo-ASE** | 1[131] | Yablonskiy and Haacke qBOLD model[7] |
| ASE- velocity-selective spin-labelling (VSSL) | 1[132] | Yablonskiy and Haacke qBOLD model[7] aided with VSSL maps |
| **ASE-VASO** | 1[133] | Yablonskiy and Haacke qBOLD model[7] |
| Electrocardiogram-triggered ASE | 1[134] | Yablonskiy and Haacke qBOLD model[7] |
| | ***GESSE*** | |
| Gradient Echo Sampling of Spin Echo (GESSE) | 12[47,52,67,79,135-140] | Yablonskiy and Haacke qBOLD model[7] |
| | ***Multi- gradient echo*** | |
| Multi- gradient echo | 19[47,56,76,141-156] | QQ model[56,131,141-147,149,152,153,155]<br>Yablonskiy and Haacke qBOLD model[7,76,148,150,151] |
| | ***GESFIDE*** | |
| Gradient Echo Sampling of FID and Echo (GESFIDE) | 2[42] | Yablonskiy and Haacke qBOLD model[7] |
| | | |
| | ***SAGE*** | |
| **SAGE** | 2[157,158] | Yablonskiy and Haacke qBOLD model[7] |

**Table 3.1 mp-qBOLD approach.** Pulse sequences applied in mp-qBOLD acquisition and the way of measuring CBV or DBV.

| **Techniques**<br>**Parameters** | **ASE** | **GESSE** | **mp-qBOLD(SE)** | **mp-qBOLD(GRE)** |
|---|---|---|---|---|
| **Number of echoes** | N/A | 26 [10-89] | 8 [4-32] | 8 [8-28] |
| **TR (ms)** | 5000 [3000-5000] | 5000 [3000-5000] | 2600 [1000-10000] | 1210[67-75000] |
| **TE (ms)** | 62 [62-82] | 62 [62-82] | 16 [8.8-17] | 5 [5-10] |
| **Delta TE (ms)** | N/A | 4 [2-4.96] | 15 [6.43-42.75] | 6 [5-7] |
| **Time of SE (ms)** | N/A | 64 [32.8-133.29] | N/A | N/A |
| **$\tau$ (ms)** | 10[-16-22.5] | - | N/A | N/A |
| **D $\tau$ (ms)** | 0.5[0.5-8] | - | N/A | N/A |
| **Spatial resolution (mm)** | 3 x 3 [2.29-3 x 2.29-3] | 3 x 3 [2.29-3 x 2.29-3] | 1.8 x 1.8 [0.86-2.5 x 1-2.5] | 1.25 x 1.3 [0.86-2.5 x 1-2.5] |
| **Field of view (mm)** | 192x192 [192-220x-192-220] | 248 x256 [160-256 x 192-256] | 240 x 203[208-320 x 156-256] | 240x182 [200-240 x160-240] |
| **Number of slices** | 16 [9-19] | 1 [1-9] | 25 [4-50] | 27 [8-75] |
| **Slice Thickness (mm)** | 3 [3-5] | 7.5 [3-8] | 4 [2-6] | 2[0.8-6] |
| **Acquisition time (mins:sec)** | 5:48 [3:48-9:36] | 12.54 [8:30-21:07] | 3.5[2.5-12.14] | 3:36[1:05-8:00] |
| **No of studies** | 7 | 10 | 24 | 24 |
| **References** | 86,116,117,120-124 | 52,53,56,67,79,135-137,159 | 18,54,69,86-97,99,100,110,112,114,115,160-162 | 42,63,86,93,108,109,111,127,128,132,137,139,140,142,149,159,160,163-166 |

**Table 3.2. qBOLD acquisition parameters.** Median and range (in square brackets) for MRI parameters used in qBOLD or $R_2$' mapping studies. Only studies with mostly complete descriptions of the relevant parameters were included.

| qBOLD acquisition | $R_2$' (Hz) | DBV (%) | OEF (%) |
|---|---|---|---|
| **GESSE** | 4.69 [2.90-6.70] [52,53,79,136] | 4.56 [1.75-4.59] [52,53,56,67,79,89,136,137] | 37.16 [31.60-46.30] [47,52,53,56,67,79,136-140] |
| **ASE** | 3.10 [2.60-3.60] [51 119] | 5.9[3.10-6.70] [51,119,131,132] | 32.66 [21.0-40.0] [51,118,119,123,131,132,167,168] |
| **mp-qBOLD** | 6.76 [4.43-8.10] [54,71,107,108,115,136,169,170] | 6.21 [4.30-9.20] [54,136] | 52.0 [29.10-60.0] [54,71,102-104,136] |
| **GRE (QQ)*** | N/A | 2.8 [1-4.5] [141,143,145,147] | 36.4 [30.6-43.8] [141,143,145,147] |

**Table 3.3. R2', DBV and OEF values.** Mean and range of in brain tissue for healthy volunteers across studies categorised by acquisition type. Means are weighted by the number of participants in each study. *Only values from the QQ approach are included for the GRE acquisition.

Table 3.3 presents the mean of $R_2'$, DBV and OEF values for healthy volunteers across studies characterised by acquisition type. The mp-qBOLD acquisition seems to provide higher values overall compared to ASE and GESSE. Accounting for magnetic field inhomogeneity (MFI) was performed in 41% of the included studies with different approaches, including prospective correction using exponential excitation pulses (12%)[, 92,96,103,104,112,115,171] or z-shimming (5%) [51,87,119,124,165], model fitting (1%) [137], slice averaging (1%) [54], voxel spread function (4%) [76,141,144,151], projection onto dipole field (12%) [56,141-143,145-147,149,153-155,163], and retrospective correction using field maps (8%) [52,53,79,132,136,148]. In addition, approximately 6% of the studies used FLAIR to suppress the CSF/ISF signal [51,113,119,124,132,165].

Common pre-processing steps that were reported were motion correction, spatial smoothing and registration to MNI or subject space. However, twenty-one studies did not report pre-processing steps [42,53,67,86,107-109,111,115,127-129,136,137,139,140,142,143,159,160,163]. The method of the analysis was mostly region of interests (ROIs), including white matter, grey matter and whole brain analysis (63 studies) or ROIs combined with voxel-wise analysis (5 studies) [104,112,120,125,168]. OEF maps were mostly computed by using least squares fitting (18 studies) [51-53,67,72,76,79,102,118,122-124,130,131,134,136,148,151,158], but in one study, Bayesian inference was used [119]. Further advanced analysis approaches such as cluster analysis of time evolution (CAT) and artificial neural network (ANN) have been applied in nine studies [56,137,143,145,149,150,152,154,155]. The main principle behind the CAT method is that voxels with a similar mGRE signal evolution have similar model parameter values, and the number of clusters as defined by machine learning is less than the number of voxels. Hence, averaging over a cluster can substantially improve SNR for a cluster-wise inverse solution that can be utilised as a robust initial estimate for voxel-wise QSM+qBOLD optimization [145]. Alternatively, ANN is a machine learning tool used to recognise patterns and classify data. It has proven to be an effective alternative approach for robust curve fitting, with good noise and outlier resilience and faster computational processing compared to least squares fitting [137]. Some of the studies did not provide detailed information about the fitting procedure that was used [88,127-129,138,140,159,168]. The most common software tools used for analysis are MATLAB (Mathworks, Natick, MA), FSL [172] and SPM [173].

**Applications**

The most investigated human organ was the brain (84 studies) followed by lower extremity muscle (4 studies)[52,127,129,130], breast (2 studies) [86,92], liver (1 study)[148], spinal cord (1 study) [157] and heart (1 study) [102]. The majority of brain studies used the mp-qBOLD approach for acquisition (34 studies) [18,53,54,69,71,72,86-92,97,99-104,106-112,114,115,159-161,171], followed by GESSE acquisition (12 studies) [47,52,67,79,135-140], then ASE (11 studies) [47,51,116,118-122,124,131,132,168]. Studies conducted on the breast used the mp-qBOLD approach [86,92]. However, in the lower extremities, all the studies used ASE [127-130].

Twenty-eight studies explored using qBOLD methods on healthy subjects for various aims, such as to assess the technical feasibility of the qBOLD method [52,54,79,117,130,134,141], and to develop a new related qBOLD technique [51,132]. Furthermore, validation studies were also performed to investigate the validity of the technique and the model [47,53,163] as well as making MRI versus PET comparisons [104,146]. On the other hand, sixty-four out of ninety-three studies (64/93) investigated diseases to measure tissue haemodynamic parameters, such as blood volume, deoxyhaemoglobin concentration, and OEF as well as measuring $T_2'$ or $R_2'$ as a surrogate marker of local oxygenation. Cerebrovascular diseases, e.g. stroke, carotid stenosis/occlusion, mitochondrial myopathy, encephalopathy, lactic acidosis, and stroke-like episodes (MELAS), were the most investigated diseases (28 studies), followed by glioma and brain tumour (17), diabetes (3) [47,127,128], haemoglobinopathies (4) [47,120,125], breast tumour (2) [86,92], multiple sclerosis (MS) (2) [107,142], clinically isolated syndrome (CIS) (2) [47,108], pre-eclampsia (PE) (2) [153,155], neurodegenerative disease (2) [47,154], human immunodeficiency virus (HIV) (2) [123,126] and one study for the following diseases: cervical spondylosis [157], retinal vasculopathy with cerebral leukoencephalopathy and systemic manifestations (RVCL-S) [121] (Figure 3.3). Table 3.4 lists the most common pathologies investigated along with clinical finding related to oxygenation parameters.

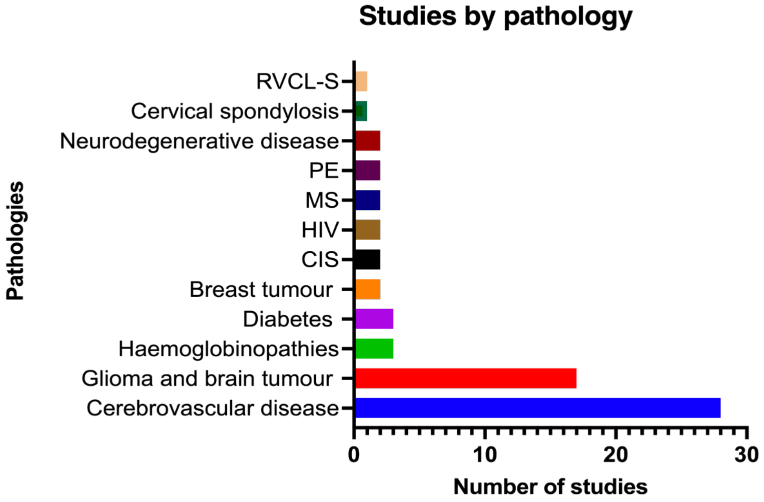

**Figure 3.3. Number of studies for each of the pathologies investigated using qBOLD or R2' mapping.** RVCL-S: cerebral leukoencephalopathy and systemic manifestations, PE: pre-eclampsia, MS: multiple sclerosis, HIV: human immunodeficiency virus, CSI: clinically isolated syndrome.

| **Pathology** | **Number of studies** | **Findings** |
|---|---|---|
| **Cerebrovascular diseases** | 28 | - Low OEF in DWI-defined lesions in ischaemic stroke patients[143,145].<br>- Different OEF histogram compared to the contralateral side in ischaemic stroke patients[145].<br>- Lower OEF in the ipsilateral side compared to the contralateral side in ischaemic stroke patients[149].<br>- Infarct core OEF value showed decreasing trend from acute to early subacute to late subacute phases of ischemic stroke[150]<br>- rCBV and OEF were unchanged, whereas $rCMRO_2$ and CBF had a relative reduction in the affected side with the stenosed carotid artery[170].<br>- rOEF was unchanged in asymptomatic internal carotid artery stenosis (ICAS) patients[103]<br>- Elevation of rOEF and CBF preoperatively which reduced to normal range following surgery in patients with severe cerebrovascular stenosis or occlusive disease[139].<br>- Decrease in the $T_2$' value in the affected side compared to the contralateral in acute stroke patients[106]<br>- Lower $T_2$' values within hypoperfused tissue in acute ischaemic stroke patients[99,106] [97].<br>- Higher $T_2$' values in hyperperfused area in acute ischaemic stroke patients[99,106].<br>- $T_2$' values in Clinically Isolated Syndrome (CIS) did not differ significantly from healthy control[111] |

| | | |
|---|---|---|
| **Glioma and brain tumour** | 17 | • Higher OEF in ipsilateral side and suspected tumour area[18,69,100,112,136,137,158,171].<br>• Low-grade glioma showed areas with increased OEF, whereas anaplastic glioma (grade III) and glioblastoma (grade IV) showed decreased OEF when compared with normal brain tissue[18,171].<br>• OEF distinguishing Isocitrate dehydrogenase IDH1 status and mutant gliomas in the tumour area[162].<br>• OEF was lower in glioblastomas than metastases[93,152]. |
| **Diabetes** | 3 | • Diabetic patients had lower OEF and oxygen consumption compared to healthy controls[128,129,174]. |
| **Haemoglobinopathies** | 4 | • Sickle Cell Anaemia (SCA) patients showed variation in whole-brain OEF and decreased values of OEF in white matter at higher risk of stroke under different treatment options[120,175].<br>• Increase OEF within normal appearance white matter of SCA patients compared to healthy control[168].<br>• Whole brain OEF values was higher in SCA patients compared to healthy control[125]. |

**Table 3.4. List of pathologies.** Findings of most common pathologies investigated using qBOLD or $R_2'$ mapping

Studies have also been performed outside of the brain. Oxygenation parameters have been measured in lower body extremities, in particular in the calf muscle, using qBOLD in patients with diabetes[127-129]. The measurements were performed at rest and during an isometric plantar flexion muscle contraction, Zheng and colleagues reported an attenuated oxygenation response during isometric calf muscle exercise in people with diabetes mellitus compared to a non-diabetic group [127-129]. In breast cancer, two studies have been conducted using the mp-qBOLD acquisition approach with DSC to assess the viability of using qBOLD as a non-invasive way to assess the tumour microenvironment (TME), hypoxia and induced neovascularization. It aimed to differentiate between aggressive and less aggressive breast cancer [86,92]. Findings from these studies suggested that mp-qBOLD can aid in the non-invasive identification of aggressive breast cancer. Two studies [153,155] have been conducted to investigate brain oxygen metabolism in pregnant women with pre-eclampsia, which causes high blood pressure. The studies found that women with pre-eclampsia had higher OEF values than healthy pregnant women.

## 3.4.Discussion

We identified ninety-three papers which used qBOLD to quantify oxygenation related parameters which together included 3,239 subjects. Multiple approaches to qBOLD acquisition and analysis were included in this review, of which 41% reported performing correction for magnetic field inhomogeneity (prospective or retrospective) and 6% reported performing correction for the presence of CSF. Studies were conducted in six organs, although 91% studied the brain, and twelve different pathologies, with the vast majority investigating cerebrovascular disease (44%) or glioma and brain tumours (27%).

### Reporting standards

Most studies reported the acquisition details except seven ASE studies which referred to other papers for more details, this leaves room for ambiguity on how the actual data were acquired. Another three ASE studies reported using triple-echo ASE but did not give enough details on how these data were analysed. Seven mp-qBOLD papers and two GESSE papers reported incomplete information about MRI acquisition parameters. Oxygenation maps were mainly computed using simple iterative least-squares regression [136]. However, in studies using the QSM+qBOLD technique, machine learning algorithms such as artificial neural networks (ANNs) have been applied with the aim of improving the robustness of curve-fitting [137,142,143,145,147]. More than half of studies did not report the fitting method details clearly. Reporting more details about both acquisition and processing methods would enable more reliable replication and comparisons of these methods.

### Acquisition and Analysis

The majority of qBOLD studies were performed at 3T using the mp-qBOLD approach (GRE and SE) for data acquisition, followed by the ASE sequence. While qBOLD can be performed using different sequences to measure oxygenation parameters, all have limitations. Because the qBOLD signal is a function of $R_2$' and DBV, alterations in acquiring these parameters can affect the final outcomes i.e. OEF. For instance, acquiring $R_2$' with different acquisitions has been shown to produce significantly different values [49]. This is particularly the case for the mp-qBOLD approach due to the multiple techniques in use to measure $T_2$, each with different sensitivities to RF pulse errors leading to overestimation of $T_2$ and underestimation of $R_2$' [71]. However, from the literature reviewed in this review, there was a notable difference in the estimate of $R_2$' between the GESSE and ASE techniques which both have a direct sensitivity to $R_2$'. When compared with GESSE measurements of $R_2$', mp-qBOLD measurements of $R_2$' are 47% higher whilst ASE measurements are 34% lower. Simulations have shown that the differences in measurements of $R_2$' using GESSE and ASE may be due to the effect of diffusion. In the GESSE technique the amount of time for protons to diffuse around the blood vessels increases with TE which flattens the signal decay around the spin echo [79]. In contrast, this time for proton diffusion is fixed for the ASE technique and equally affects all of the t values ($R_2$'-weightings) [77]. Whilst for mp-qBOLD, the higher $R_2$' measurements are believed to be due to stimulated echoes due to slice-selection pulse imperfections in 2D-GraSE and 2D-TSE imaging that lead to $T_2$ overestimations, hence higher $R_2$' measurements. To overcome these issues, it is advisable to use non-slice selective and 3D acquisition techniques, such as 3D-GraSE, to reduce $T_2$-related bias in mp-qBOLD [71]. $R_2$' values for the QQ approach are not available since this model fits directly for OEF and DBV. The $R_2$' measurements reported from the included studies highlighted the notion that $R_2$' measurements are clearly influenced by the acquisition method (Table 3.3), which also has been reported previously [49]. This is an important consideration for designing and evaluating research studies that use $R_2$' measurements. In addition, $R_2$' measurements are influenced by the orientation of the white matter fibers [74] and the existence of the myelin, which has a high diamagnetic susceptibility. Each voxel's signal decay becomes multiexponential due to the presence of extracellular, intracellular, and myelin water compartments. Previous studies have shown that a significant frequency shift is caused by the water compartmentalization in the myelin, which increases the $R_2^*$ decay during gradient echoes[176,177].

It is crucial to distinguish between the susceptibility effects caused by deoxyhemoglobin and those caused by static field inhomogeneities to get a more accurate estimation of $R_2$'. To recover signal loss or separate the impacts of these two field fluctuations, a number of techniques have been applied in the included studies. The most common ways were as follows, applying an exponential excitation pulse [72,92,96,103,104,112,115,171], using high-resolution field maps [52,53,79,136], and voxel spread function [76,141,144,151]. Each of these approaches presents distinct advantages and limitations in practice. The exponential excitation pulse technique, while effective at compensating for magnetic field distortions occurring across different slice levels, can increase RF power deposition and acquisition times. High-resolution field maps provide detailed field inhomogeneity information but remain susceptible to motion artifacts. The voxel spread function approach successfully addresses magnetic field distortions both within each brain slice and between different slice levels, though it requires more sophisticated post-processing protocols. Furthermore, accounting for the presence of partial volumes of cerebrospinal fluid (CSF) is important. This consideration is particularly crucial as CSF contamination can significantly impact $R_2'$ quantification accuracy, especially in regions adjacent to CSF-filled spaces. However, few studies considered suppressing CSF/ISF signal by using a FLAIR preparation pulse [51,113,119,124,132,165]. The limited implementation of CSF suppression represents a significant methodological gap in the field. For optimal accuracy in $R_2'$ quantification, particularly in cortical regions or areas near ventricles, CSF suppression should be considered essential despite the additional scan time required. Moving forward, researchers should prioritize combining appropriate susceptibility compensation techniques with CSF suppression, with the specific choice guided by the balance between precision requirements and practical constraints such as available scan time. There remains a clear need for comparative studies that evaluate these various techniques, particularly in combination with CSF suppression, to establish more definitive methodological guidelines for different research and clinical applications.

**Commented [AA5]:** Comment 5.

The deoxygenated blood volume (DBV) is similarly measured in different ways (Table 3.3). In the qBOLD model, the DBV is estimated from the transverse signal decay, but this method has potential issues, including signals from intravascular blood [50], diffusion narrowing effects [77], and signals from macromolecules [52]. On the other hand, in mp-qBOLD, the DBV measure is replaced by the dynamic susceptibility contrast (DSC) measure of cerebral blood volume (CBV). This CBV measure is combined with a separate measurement of $R_2'$ to estimate oxygen extraction fraction (OEF). However, it is important to note that DBV in the qBOLD model specifically refers to the percentage of CBV that contains deoxyhaemoglobin. This leads to a discrepancy between DBV, which is specific to vessels carrying deoxygenated blood, including veins, and CBV from DSC, which is sensitive to all vessel types and represents total blood volume.  Although estimating CBV separately results in a relative measure of OEF [72], it is perhaps a more pragmatic approach for clinical settings. However, when compared with GESSE measurements of DBV, mp-qBOLD measurements of DBV are 48% higher, ASE measurements are 9% higher and GRE measurements using QQ analysis are 39% lower (Table 3.3). It is worth noting that the QQ approach derives its sensitivity to DBV from the same source as GESSE and ASE measurements (Equation 3.4). One of the included studies introduces a new approach which relies on velocity selective spin labelling (VSSL) pulses to measure DBV non-invasively [132]. For comparison, the only other technique for measuring DBV, which uses the BOLD response to a hyperoxia challenge, estimates DBV to be between 2.2 and 8.2% [38,164].

Regarding the QQ approach, by integrating both qBOLD and QSM there is the potential to counterbalance each of their limitations. One of the drawbacks of the qBOLD model, which neglects non-blood sources of magnetic susceptibility (e.g. myelin), is addressed by QSM, which is able to measure the total magnetic susceptibility regardless of its origin. Conversely, QSM does not directly factor in deoxygenated blood volume (DBV) and assumes a linear relationship with cerebral blood flow (CBF). In this symbiotic relationship, both approaches complement each other, potentially resulting in a more comprehensive methodology where the strengths of one method offset the weaknesses of the other[59,146]. This method has recently been validated against PET. Findings showed the average OEF values across subjects did not significantly differ between QSM+qBOLD and $^{15}$O-PET[146], but the study did not assess the correlation between individual measurements from the two techniques, leaving uncertainty about their agreement on a subject-by-subject basis.

**Commented [AA6]:** Comment 6

The considerably higher proportion of studies (40%) using the mp-qBOLD approach is likely due to its reliance on pulse sequences that are already available on the scanner (i.e., SE or GRE). This makes it easier to implement in a clinical setting whereas techniques like ASE and GESSE require custom pulse sequences. This is also true for the QQ approach which utilises a standard multiecho GRE pulse sequence, so long as magnitude and phase data can be reconstructed on the scanner. mp-qBOLD approaches are also the most common in the brain and ASE is the only technique used in the lower extremities. This is likely due to slow changes in OEF in the clinical brain applications listed in the results, which are suited to the multishot approaches used in mp-qBOLD acquisitions. Whilst ASE is a much more rapid acquisition aiding the measurements of the transient changes in muscle during hyperaemia. It is important to note that for fMRI studies of changes in brain oxygen metabolism the calibrated BOLD technique is more suited due to its higher temporal resolution. Studies using qBOLD on other parts of the human body were limited. Nonetheless, existing studies outside of the brain and muscle demonstrate the potential for investigating diseases elsewhere in the human body using qBOLD. Although qBOLD provides a non-invasive approach for assessing OEF, in the context of a clinical setting, it might be impractical to apply. However, mp-qBOLD provides great applicability in clinical settings due to the MRI protocol availability.

### Applications

**Commented [AA7]:** Comment 7.

qBOLD was used to measure baseline oxygenation parameters in several pathologies including steno-occlusive diseases, stroke, and small vessel disease (Figure 3.3 and Table 3.4). While these investigations showed that ischaemic stroke patients had lower OEF in the core infarcted region (tissue that is unsalvageable) than the contralateral region of the brain and a decreasing trend from acute to early subacute to late subacute phases of ischemic stroke, it is important to note that calculating OEF in severely compromised tissue presents fundamental challenges. In regions where blood flow and metabolism are markedly reduced, the interpretation of OEF becomes problematic as it represents a ratio between these impaired parameters. In contrast, an OEF elevation was observed in the penumbral region (tissue that may be salvageable with treatment), which typically surrounds the core infarct, compared with healthy tissue in the contralateral hemisphere was also reported [143,149,150]. The penumbra region suffers from a lack of blood flow and can recover if the blood supply can be restored in a timely manner [178].

In terms of $T_2$’, it has been observed to be reduced in the infarct core, as defined by a thresholded ADC map, when compared with healthy tissue [97,106]. Similar but smaller reductions are seen within hypoperfused tissue regions of interest defined by time-to-peak (TTP) by DSC [99]. These decrease in $T_2$’, or equivalently increases in $R_2$', suggest a more rapid signal decay due to the higher than normal deoxyhaemoglobin content of the tissue, which is a consequence of elevated OEF caused by hypoperfusion and/or an increase in DBV[97,106]. However, these $T_2$' measurements in the core require careful interpretation, as the signal changes may also reflect tissue degradation, alterations in magnetic susceptibility, or residual deoxyhaemoglobin in poorly perfused vessels rather than active oxygen metabolism.

These findings are consistent with our current understanding of the pathophysiology from PET imaging. According to PET studies, there should be a significant rise in OEF in the penumbra [179]. However, within the core infarct there is the potential for disagreement with PET. In PET imaging oxygen metabolism is observed to be reduced within the core [180], whilst $T_2$' has been observed to decrease consistent with an increase in oxygen metabolism [100]. However, Geisler et al. were able to reconcile this discrepancy in the following way[106]. PET relies on an intravascular tracer which cannot reach the core due to a compromised blood supply yielding a negligible oxygen metabolism [97]. Whilst measurements of $R_2'$ do not rely on the delivery of a tracer and hence remain directly sensitive to any residual deoxyhaemoglobin, regardless of whether it reflects active metabolism or stagnant blood in severely compromised tissue.

Obtaining qBOLD-based OEF measurements for ischemic stroke is particularly challenging due to two main reasons. Firstly, it requires a long acquisition time to obtain high spatial resolution images or many echo times, which can lead to patients moving during the process. This is a common issue with stroke patients that requires motion correction, resulting in additional data acquisition[99,124,159] or image artifacts[124]. Secondly, using the same Hct value for ischemic and non-ischemic regions can lead to an overestimation of OEF [124,159]. It is also important to note that certain factors such as necrosis, bleeding, iron deposition, fibre orientation cerebral spinal fluid or macroscopic magnetic susceptibility gradients may cause artificially high OEF values field[51,106,110,124].

Studies conducted in patients with glioma and brain tumours, reported consistent results of higher OEF in the ipsilateral side and suspected tumour area[100,136,137]. Moreover, high-grade glioma revealed higher OEF values than lower-grade glioma[18,69,112,158,171]. However, the heterogeneous nature of gliomas, with different cellular densities, and blood flow patterns, represent a source of bias when merging all types of gliomas into the same group-grade[109,158]. Moreover, it is possible that the necrotic tissue in tumours is susceptible to haemorrhage in the necrotic core, which may result in high $R_2'$ values[112]. Even if there is no bleeding, necrotic tissue can still be problematic because its relative cerebral blood volume (rCBV) is zero. Therefore, OEF may increase above any physiologically significant threshold [112].

In patients with MS, the reported finding indicated higher OEF values in the rim area compared to the lesion and lower OEF for the whole brain in MS patients compared to healthy control patients [142]. Two studies attempt to evaluate hypoxia in breast cancer, which is a prevalent feature of malignant tumours and is associated with poor treatment outcomes using qBOLD [86,92]. They calculated various quantitative MRI biomarker maps, such as OEF and metabolic rate of oxygen ($MRO_2$), using histopathology as a standard of reference. The findings demonstrated that invasive ductal carcinomas (IDCs) were more hypoxic than benign tumours [92]. Also, aggressive malignancies had a greater oxygen consumption than less aggressive cancers [86]. It seems qBOLD is a promising technique for measuring baseline oxygenation parameters in a broad range of pathologies and promising direction for some clinical populations.

### 3.5.Implications for future research

The application of qBOLD experiments can vary substantially, particularly in the sequence chosen i.e. ASE, GESSE and mp-qBOLD. This induces heterogeneity in the outcome measurements of $R_2'$ making it difficult to compare the results of different studies. As yet, there does not seem to have been a direct comparison of a variety of these techniques to assess any systematic differences. However, it should be noted that this is difficult to achieve in human participants due to the normal variation in OEF which can be caused by natural variations in blood carbon dioxide levels [181]. Therefore, phantom based comparisons may be needed. Amongst the included studies phantoms were used for several purposes including testing post-processing techniques for correcting for macroscopic magnetic field inhomogeneity [72,79]. One study used Gadolinium doped agar gel phantoms to produce a range of $T_2$ values to test the accuracy of an improved $T_2$ measurements as part of an mp-qBOLD approach [71]. However, these kinds of phantoms are not useful for comparing techniques for measuring $R_2'$ because they have little to no $R_2'$ contrast. One further study sought to introduce $R_2'$ contrast by randomly coiling polypropylene strings in mineral oil to generate the mesoscopic magnetic field inhomogeneity that underlies the qBOLD signal [47]. This scoping review was not targeted at phantom comparisons and so the literature captured may be incomplete. However, these studies provide a future direction for phantoms to compare qBOLD variants or between scanners, which might be particularly important for multicentre studies. In addition, validation with the gold standard PET imaging is important; however, this is challenging due to the invasive nature involved in applying PET when using the radioactive agents and its limited availability.

In addition, as noted above, there are multiple techniques in use for estimating DBV, which are not directly comparable. Thus, caution must be taken when reporting OEF results, which are greatly reliant on the pulse sequence and the way in which DBV is estimated. This is true in the case of mp-qBOLD, which does does not exactly reflect the deoxygenated blood which qBOLD measures. However, since the mp-qBOLD approach is more applicable in clinical settings, it would be worth investigating a more precise way to measure the DBV; one alternative option to DSC-based measurements of CBV is to use hyperoxia-BOLD contrast to measure venous CBV (CBVv) [164]. Preliminary work has been presented to demonstrate this approach [182].

When using qBOLD to measure the oxygen extraction fraction (OEF) in conditions such as stroke and glioma, it is important to consider several factors that can impact the accuracy of OEF and $R_2$' measurements. These factors may include bleeding and necrosis. Using multiple MRI sequences, such as diffusion-weighted imaging (DWI) and perfusion-weighted imaging (PWI), can help provide additional information and enable differentiation between various tissue compartments, including areas that may be affected by bleeding or necrosis. In addition, correlating findings from different qBOLD approaches with histopathological analysis of tissue specimens can validate the accuracy of OEF measurements and help interpret discrepancies arising from factors like necrosis, haemorrhage, or cellular infiltration

Public availability of analysis tools is currently limited, with only a single example identified Quantiphyse [119,183]. However, this tool is only optimised for the ASE acquisition. In future, greater availability of these tools would help to promote reproducibility and harmonisation.

**Limitations of the review**

This review was limited to human studies. Therefore, it does not present detail regarding preclinical qBOLD methodologies. However, the basic processing techniques are similar. In addition, it only included studies in the English language due to the long process of translation and time limitations. To date, there has not been a systematic review of the use of qBOLD techniques for measuring blood oxygenation in the human body. Therefore, this review is the first to cover this topic and highlight the use of qBOLD in clinical populations.

### 3.6.Conclusion

While qBOLD for measuring oxygen metabolism is a relatively underdeveloped technique we identified applications in several clinical populations including cerebrovascular diseases, brain tumour and glioma, multiple sclerosis, breast cancer and diabetes mellitus. This highlights the value of qBOLD oxygenation measurements in clinical research. However, acquisition techniques and analysis methods all varied substantially. Future work ought to aim towards consensus recommendations to facilitate more reliable and harmonised qBOLD measurements for use in clinical research and trials of new therapies.

# 4.Development of a quantitative BOLD phantom for validation of acquisition strategies.

In this chapter a phantom to produce $R_2'$ (reversible transverse relaxation rate) contrast was developed by inducing subvoxel magnetic susceptibility variation that mimics the quantitative Blood Oxygenation Level Dependent (qBOLD) MRI signal. Microscopic glass bubbles were used for this purpose and it was demonstrated that they offer a cheaper option for making large volume phantoms than existing phantoms that used precision polystyrene microspheres. A linear relationship between the $R_2'$ contrast and the glass bubble volume fraction was found for the constructed test object. The phantom was subsequently used for a comparison of multiparametric qBOLD acquisitions between two MRI vendors.  In future, phantoms such as this could facilitate quality assurance for qBOLD acquisition strategies and assist with multicenter harmonization.

Acknowledgements:  We thank Prof. Dr Klaus Scheffler and Dr Jörn Engelmann from the Department of Biomedical Magnetic Resonance, University of Tübingen, Germany, for sharing their phantom recipe using hydroxyethylcellulose (HEC) gel.

## 4.1.Introduction

Quantitative BOLD (qBOLD) aims to estimate the oxygen extraction fraction (OEF) from the reversible transverse relaxation rate $R_2'$. This has applications in the diagnosis of cerebrovascular diseases such as stroke [124] and glioma [69]. $R_2'$ can be measured in multiple ways, but these measurements may not be equivalent. The multiparametric mp-qBOLD technique [184] uses separate sequences to measure the irreversible transverse relaxation rate $R_2$ and $R_2^*$ ($R_2^* = R_2 + R_2'$) independently before calculating $R_2'$. However, there are multiple sequences used to make these measurements, such as GESSE (Gradient Echo Sampling of Spin Echo) and ASE (Asymmetric Spin Echo) which are single-sequence methods that attempt to measure $R_2'$ more directly. GESSE acquires multiple gradient echoes around a spin echo. This sequence produces signal affected by both $R_2$ and $R_2'$, requiring complex analysis to separate these effects, often using symmetry properties of the signal decay [67], or quadratic exponential decay of the signal around the spin echo [52]. ASE, on the other hand, manipulates $R_2'$ weighting while maintaining constant $R_2$ weighting by shifting the refocusing pulse relative to the readout. This allows for more direct estimation of $R_2'$ without the need to simultaneously fit $R_2$ [50] . As per the sc-review chapter $R_2'$ measurements across these multiple acquisition approaches vary slightly ranging from 3-6 Hz. It is essential to show minimal bias and high consistency across pulse sequences and various vendors systems. Regarding the latter, the literature appears sparse regarding systematic comparisons of $R_2$' measurements across different manufacturers' systems, suggesting a potential area for future investigation.

After a method is introduced in a clinical trial or clinical practice, it is essential to prove its ongoing ability to be replicated at several locations, over a period of time, and even after any alterations to the system. This is particularly important in the case of multicenter and longitudinal trials. An MRI phantom, frequently known as a reference object or test object, acts as a useful tool for assessing bias and reproducibility in quantitative data. Researchers employ phantoms to verify the accuracy of new MRI techniques and carry out assessments of bias and reproducibility across several sites [185,186]. Additionally, phantoms play an essential role when performing quality control (QC) measurements on scanners and act as valuable educational tools. Regular use of phantoms is crucial for ensuring the reproducibility of MRI data, as they help verify that scanners are functioning properly and that the necessary hardware and software are in place at various sites to produce the required imaging. Building an MRI phantom involves choosing the right substance that can replicate the magnetic properties of human tissue. Common materials include water-based gel, oil, or organic liquids that can be doped with substances like nickel chloride ($NiCl_2$), copper sulfate ($CuSO_4$), or manganese chloride ($MnCl_2$) to adjust $T_1$ and $T_2$ values [187]. Phantoms should ideally be stable over time with known expiry periods or aging decay properties. It is recommended that these phantoms should be simple to assemble and can be reproduced consistently [188] to ensure reliable results across various studies and research locations.

One of the main challenges for the qBOLD technique is achieving consistent and reliable values across different acquisition methods, sites, and vendors to facilitate its use in clinical settings and enhance its reliability. This highlights the need for developing an MRI phantom for the $R_2$' parameter. Generating $R_2$' contrast in a phantom requires creating microscopic magnetic susceptibility variations at the scale of the microvasculature (subvoxel level). Previous studies have used precision polystyrene microspheres to demonstrate the generation of microscopic susceptibility variation in a phantom [189]. However, polystyrene microspheres are expensive and only suitable for creating small-volume phantoms. Other studies have attempted to simulate the magnetic susceptibility distribution of a vascular network within a phantom using polyethene fishing lines and filament strands [46], as well as coiled polyamide strings [190]. However, the relatively large size of these fishing lines and polyamide strings may not accurately replicate the subvoxel susceptibility variations that are intended to be represented. Therefore, this study aims to explore the use of glass bubbles as a more cost-effective alternative with a more reasonable suitable median diameter of 60µm and easily reproducible $R_2'$ phantom. Spherical particles offer several advantages over filament-based models. Firstly, they can be more easily and uniformly distributed throughout a phantom, potentially providing a more realistic representation of randomly distributed susceptibility sources. Additionally, while spheres do not approximate infinite cylinders like blood vessels, Yablonskiy, Haacke [7] demonstrated that both geometries produce similar effects on the reversible transverse relaxation rate ($R_2'$). Specifically, their theoretical model showed that spherical objects tend to produce a more pronounced $R_2'$ effect than randomly oriented cylinders, indicating that spheres can serve as a reasonable proxy for cylindrical structures in many scenarios. Therefore, the goal of this study is to produce a phantom that can be used for quality assurance and facilitate standardization across multiple centers. Hence, the primary objective for this study was to develop an $R_2'$ phantom using glass bubbles. A secondary objective was to make a comparison of multiparametric qBOLD acquisitions between two MRI vendors (Philips Achieva 3T and GE SIGNA Premier 3T). Additionally, the longitudinal relaxation rate ($R_1$) was also investigated using the produced phantom. In future, phantoms such as this could facilitate quality assurance for qBOLD acquisition strategies and assist with multicenter harmonization.

### 4.2.Materials and methods

In the search for a suitable gelling agent to create a uniform phantom, several initial trials were conducted testing a few gelling agents: agar, sodium alginate, and hydroxyethylcellulose (HEC). Agar, although commonly used in phantom studies, was found to be problematic for our specific application. It requires heating to high temperatures, typically using an autoclave, which led to undesirable reactions with the glass microbubbles. Attempts to mix the microbubbles into the gel after heating resulted in poor uniformity. Sodium alginate demonstrated problems related to viscosity, posing challenges to achieve the desired structural stability and uniform distribution of glass bubbles throughout the phantom. Hydroxyethylcellulose (HEC) was identified as the best option for our $R_2$' phantom due to its unique advantages. It easily dissolves in water at room temperature, eliminating heating-related risks to the glass microbubbles. Additionally, it provides excellent viscosity control, allowing us to fine-tune the phantom's consistency while maintaining long-term stability. The high compatibility of HEC with glass bubbles helps to create the desired uniformity. These properties make HEC an ideal choice for our research.

**Sample preparation**

Phantom samples were prepared using a HEC solution. First, sodium chloride (NaCl) was dissolved in deionized water with vigorous stirring until fully dissolved. Gradually, HEC (Sigma-Aldrich, 09368) was added to the NaCl solution while maintaining continuous stirring to prevent clumping. Once the HEC was fully mixed in, K20 glass bubbles (3M, MN, USA) were introduced to achieve specific volume fractions. The mixture was then stirred at medium speed for an appropriate duration based on the observed quality of the gel, with longer stirring times required for lower glass bubble fractions to ensure even dispersion. This preparation method ensured consistent concentrations of HEC and NaCl, as well as a uniform distribution of glass bubbles across all samples. For the full Standard Operating Procedure (SOP) used in the preparation of these phantoms, please refer to the Appendix (B).

**Stage 1: Glass Bubble Effects**

In the first stage, an experiment was conducted to assess the impact of different concentrations of glass bubbles on the MRI signal of the phantom, in particular the $R_2$' contrast at 3T. Four 30ml vials were filled with HEC gel with randomly selected volume fractions of K20 glass bubbles at 0%, 1%, 2%, and 3%. These preliminary trials allowed us to evaluate the effect of varying glass bubble concentrations on $R_2$' and establish a baseline relationship between volume fraction and $R_2$'. The gel for each vial was prepared as described above. The mixture was then stirred with a magnetic stirrer at room temperature until it thickened, which took approximately 10-40 minutes depending on the volume fraction of glass bubbles.

**Stage 2: Reproducibility & repeatability:**

This stage aimed to evaluate the reproducibility of phantom construction and the repeatability of MRI measurements. Four 30 mL vials were prepared with

HEC gel with 0%, 1%, 2%, and 3% volume fractions of K20 glass bubbles, stirred as before. Two sets of vials (Set A and Set B) were produced to test the reproducibility of the construction process, and one set (Set A) of vials was scanned twice to assess the repeatability of the MRI measurements.

### Stage 3: Sequence comparison and Phantom stability

The objective of this stage was to produce a phantom that would match the expected $R_2$' values in the human brain to enable the comparison of rapid clinical protocols with a reference scan. A MultiSample 190F (Gold Standard Phantoms, Rochester, UK) was filled with twelve 50 ml vials containing HEC and a range of volume fractions (0 to 1 % in steps of 0.1% and 2%) following the procedure above for producing HEC phantoms. The whole phantom was filled with deionized water, Nickel Chloride (1mM) and Sodium Chloride (0.5%) (Figure 4.1). This phantom was scanned twice, within a week from preparation and after a month to assess phantom stability over time.

In order to determine the volume fraction of glass bubbles needed to match the expected range of $R_2$' in the human brain, we used a linear equation derived from our data in stage 1, which focused on the effects of glass bubble volume fraction. The equation takes the form:

$$\boldsymbol{R_2' = mVf + b} \quad \textbf{Equation 4.1}$$

Where Vf is the volume fraction of glass bubbles m is the slope (in Hz per unit of volume fraction) b is the y-intercept (in Hz). By plotting the $R_2$' values against the volume fractions of glass bubbles, we obtained a linear relationship. The slope ($m$) and intercept ($b$) from this plot were then used to calculate the required volume fraction of glass bubbles to achieve the desired $R_2$' values. This approach ensured that the phantom accurately represented the $R_2$' relaxation rates expected in human brain grey matter.

**Figure 4.1 The phantom picture.** The MultiSample 190F from Gold Standard Phantoms contains twelve 50 ml Falcon tubes filled with a range of glass bubble volume fractions from 0 to 2% in hydroxyethylcellulose gel.

### Stage 4: $R_2$ Adjustment with Gadolinium

This stage aimed to optimize the transverse relaxation rate ($R_2$) of the phantom by adding gadolinium to achieve $R_2$ values that closely match those of human brain grey matter at 3T. Initial measurements revealed that the $R_2$ ($1/T_2$) values of the phantom were too small and fell outside the expected range for human brain tissues. To address this, gadolinium was introduced to improve the susceptibility and adjust the $R_2$ relaxation rates accordingly. Initially, an experiment was conducted using gadolinium alone, without glass bubbles, to determine its effect on $R_2$ values at different concentrations. The gadolinium concentrations used were 0%, 0.3%, 0.6%, 0.9%, and 1.2%. This data was used to derive a linear equation:

$$\boldsymbol{R_2 = m[Gd] + b.} \quad \textbf{Equation 4.2}$$

Where [Gd] is the gadolinium concentration (in %) m is the slope (in Hz per % of Gd) b is the y-intercept (in Hz). By plotting the $R_2$ values against the gadolinium concentrations, a linear relationship was established. The slope ($m$) and intercept ($b$) from this plot were then used to calculate the desired gadolinium concentration needed to match the expected $R_2$ values in human brain grey matter. Following the same procedure as in Stage 3, a MultiSample 190F (Gold Standard Phantoms, Rochester, UK) was filled with twelve 50 mL vials containing HEC and varying volume fractions of glass bubble (ranging from 0% to 1% in increments of 0.1%, plus an additional 2% volume fraction). Each vial received 436.15 microliters of gadolinium per 80mL. The gel was stirred using a magnetic stirrer at room temperature until it thickened, ensuring a uniform distribution of gadolinium within the gel. This adjustment aimed to bring the $R_2$ values within the desired range, thus making the phantom a more accurate model for simulating the relaxation properties of human brain.

**Imaging Protocol**

Reference Scan

Initial images were acquired on a 3T Achieva (Philips Healthcare, Best, The Netherlands) to serve as a benchmark. This reference scan utilized turbo spin echo (TSE) and multi-echo gradient echo (mGRE) sequences with single-slice acquisition. The TSE sequence included echo times of 9, 12, 15, 20, 30, 40, 50, 100, and 150 ms, with a TR of 3000 ms. The mGRE sequence had 20 echoes (TE1 = 6 ms, ΔTE = 5 ms) and a TR of 500 ms, all acquired with a resolution of 2x2x3 mm for a single central slice. This setup ensured high accuracy and precision in $T_2$ and $T_2$* measurements, albeit with longer acquisition times, making it ideal for a controlled research environment. In addition, $T_1$-weighted turbo spin-echo (TSE) sequence with 12 inversion times were acquired using the following parameters: inversion times (TI) ranged from 50 ms to 5000 ms, TR=10000ms, TE=7 ms.

Clinical Adaptation on Philips Scanner

To transition towards more clinically applicable imaging protocols, the mGREsequence on the Philips scanner was adapted to include 30 slices with a TR of 1950 ms. Additionally, a 3-dimensional gradient- and spin-echo (3D-GRASE) multiple echo sequence was implemented, featuring 16 echoes (TE1 = 10 ms, ΔTE = 10 ms, TR = 486 ms) across 30 slices with a resolution of 2x2x3 mm. These modifications aimed to balance the need for detailed relaxation time measurements with the practical requirements of clinical imaging, ensuring comprehensive coverage and reduced acquisition times. In addition, gradient echo sampling of spin echo (GESSE) was acquired. The sequence parameters were 2 x 2 x 2 mm, TE = 55 ms, TR = 2000 ms, gradient echo spacing (ΔT) = 0.89 ms, and number of slices = 30.

Clinical Adaptation on GE Scanner

Similarly, a protocol was designed for the 3T SIGNA Premier (GE Healthcare, Waukesha, WI). The mGRE sequence was configured with 16 echoes (TE1 = 3.12 ms, ΔTE = 2.7 ms, TR = 1950 ms) and a T2MAP multiple echo spin echo sequence with 8 echoes (TE1 = 5.5 ms, ΔTE = 5.5 ms, TR = 1200 ms). Both sequences were acquired with 30 slices and a resolution of 2x2x3 mm. This approach ensured that the imaging protocols were consistent across different scanners, facilitating comparability and reproducibility.

**Imaging analysis**

Data Preparation

All MRI images were first converted from DICOM to NIFTI format using MRIcroGL software [191]. Subsequently, individual echo images were integrated into a 4D dataset using tools from the FMRIB Software Library (FSL) [172] enhancing data management efficiency. Square regions of interest (ROIs) ( 6 × 6 pixels) were placed in the centre of each tube also in FSLeyes, part of the FSL suite [172], Figure 4.2.

Data Analysis

Custom made MATLAB scripts (Mathworks, Nattick, MA) were employed to analyze the MRI signal data and extract the transverse relaxation rate ($R_2$), the apparent transverse relaxation rate ($R_2$*), and the longitudinal relaxation rate ($R_1$). MRI data and corresponding masks were loaded and reshaped for further processing. For each ROI, defined by the mask, the mean signal intensity was calculated across all voxels within that ROI. This preprocessing step ensured that the analysis was based on averaged signals, reducing the impact of noise and providing a more robust estimate of the relaxation rates.

The analysis of $R_2$ involved fitting a mono-exponential decay model to the signal intensity data at various echo times (TEs). The selected echo times and corresponding mean signals for each ROI were used in the fitting process. The model used was:

$$\boldsymbol{S(TE) = S_0\, exp\,(-TE\, R_2)} \quad \textbf{Equation 4.3}$$

where S(*TE*) is the signal intensity at echo time *TE*, $S_0$ is the initial signal intensity, and $R_2$ is the transverse relaxation rate. By log-transforming the signal intensities, the model was linearized to:

$$\boldsymbol{ln\big(S(TE)\big) = ln(S_0) - TE\,R_2} \quad \textbf{Equation 4.4}$$

Linear regression was then applied to the log-transformed data to estimate $R_2$. This method simplified the fitting process and improved robustness. The resulting $R_2$ values, along with their standard errors, were subsequently used for further statistical analysis and visualization. The apparent transverse relaxation rate ($R_2$*) was analyzed similarly to $R_2$, but with adjustments to account for magnetic field inhomogeneities. The signal decay was modeled as:

$$\boldsymbol{S(TE) = S_0\, exp\,(-TE\, R_2^*)}. \quad \textbf{Equation 4.5}$$

A log-linear regression approach was also employed, where the signal intensities were log-transformed and linearly regressed against the echo times. This allowed for the estimation of $R_2$*, capturing the effects of both intrinsic tissue properties and magnetic field inhomogeneities. The resulting $R_2$* values were then used for comparative analysis.

The longitudinal relaxation rate ($R_1$) was derived from the inversion recovery MRI data. The fitting model for longitudinal relaxation was based on the inversion recovery equation:

$$\boldsymbol{S(TI) = M_0\,(1 - 2\,exp\left(-\frac{TI}{T_1}\right)}. \quad \textbf{Equation 4.6}$$

where $S$(TI) is the signal intensity at inversion time $TI$, $M_0$ is the equilibrium magnetization, and $T_1$ is the longitudinal relaxation time. Initial estimates for $M_0$and $T_1$ were provided, and a non-linear least squares fitting method was used to minimize the sum of squared differences between the measured and model-predicted signal intensities. The optimization was performed using the fminsearch function in MATLAB. Once $T_1$ values were obtained, they were converted to $R_1$ using $R_1$=1/$T_1$. The resulting $R_1$ values were used for further statistical analysis and visualization.

For TSE measurements, the first 3 echoes were excluded from the analysis due to instability in the signal decay. For the Philips mGRE data, 10 initial echoes were used to avoid the noise floor. All echoes were utilized for the Philips 3D-GRASE and GE data. Subsequently, the calculated values for the relaxation rate $R_2$, $R_2$*, $R_2$' and $R_1$ were exported to Prism [192] for statistical analysis and figure generation.

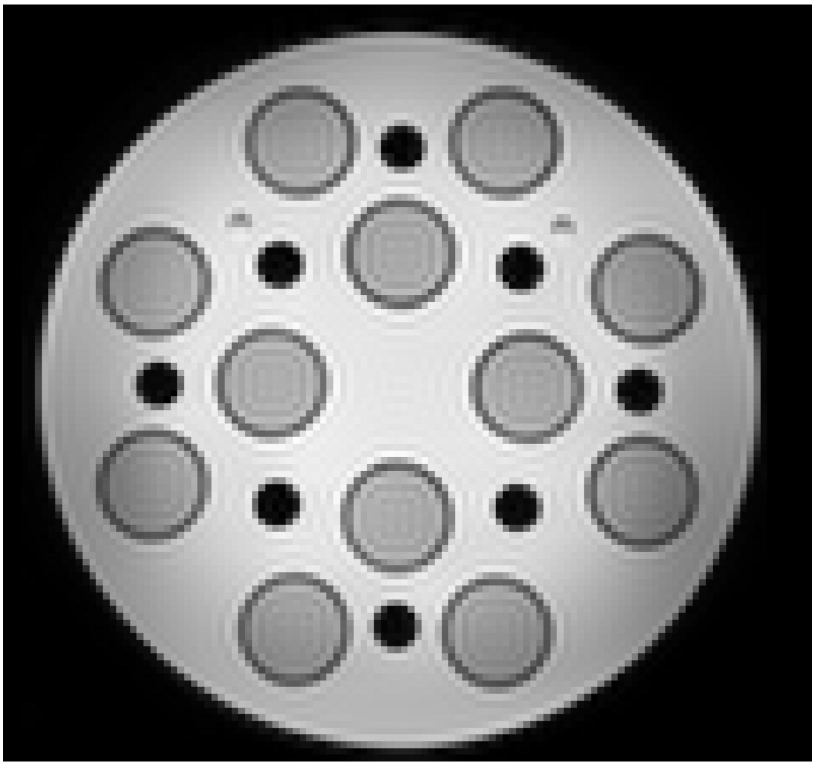

Figure 4.2 $T_2$ **weighted image of the phantom.** Image of The MultiSample 190F from Gold Standard phantom). Twelve ROIs were created manually in FSLeyes positioned centrally for each of 50 mL vials with varying volume fractions of K20 glass bubbles.

**Commented [AA8]:** Comment 9.

## 4.3.Results

### Glass Bubble Effects, Reproducibility and Repeatability

The scatter plot in Figure 4.3a shows the effect of microscopic glass bubbles on the $R_2'$ contrast in the phantom. A strong $R_2'$ contrast was found as a function of glass bubble volume fraction, with a minimum value of $R_2' = 1.34$ Hz, and a maximum value of 56.39 Hz. Moreover, the phantoms demonstrated good reproducibility in both phantom construction (Figure. 4.3b) and MRI measurements (Figure. 4.3c). In Figure 4.3b the scatter plot compares $R_2'$ values between Set A and Set B, illustrating the consistency in phantom construction. The data points closely align with the unity line, suggesting minimal variation in $R_2'$ measurements across both sets ($R^2 = 0.99$), indicating that the phantoms can be reproducibly constructed. Similarly, Figure 4.3c evaluates MRI measurement repeatability by comparing $R_2'$ values from two scans of Set A ('scan1' and 'scan2'). The data points in Figure 4.3c also closely align with the unity line (y = x), implying high consistency in $R_2'$ values between scans ($R^2 = 0.99$).

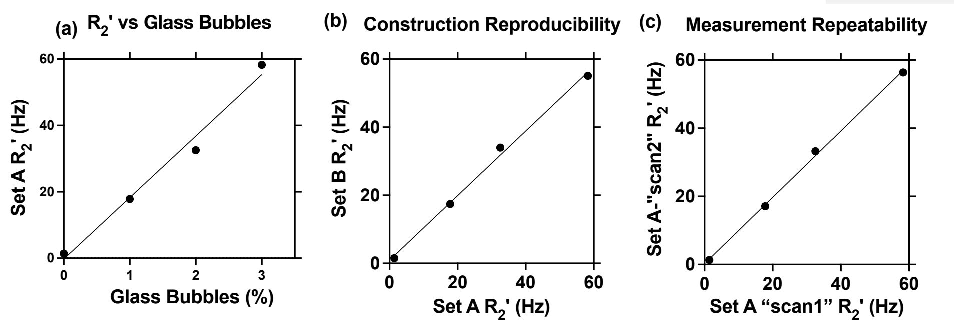

**Figure 4.3 $R_2'$ measurements for glass bubble.** The results of the glass bubble volume fraction on $R_2'$, construction reproducibility and measurement repeatability experiments. (a) A linear relationship between $R_2'$ and glass bubble fraction is found, (b) good reproducibility of both phantom construction and (c) the MRI measurement repeatability.

**Commented [AA9]:** Comment 10.

### Sequence comparison and Phantom stability

The targeted value of $R_2'$ was achieved at very low volume fractions of glass bubbles, around (0.1% - 0.3 %), Table 4.1. Figure 4.4 shows the comparison between measured values of $R_2'$, $R_2$, and $R_2^*$ against the reference data for sequence comparison between qBOLD acquisitions and different vendors. The data showed reasonable agreement between the measured $R_2^*$ and reference values across different datasets. Specifically, the $R^2$ values were 0.9985 for mGRE-Philips, 0.9873 for mGRE-GE, and 0.9805 for GESSE, indicating high levels of consistency. However, poor agreement is found between the measurements of $R_2$ for different datasets. The $R^2$ values are 0.6924 for 3D-GRASE-Philips, 0.4647 for mSE-GE, and 0.2970 for GESSE, indicating weak consistency (Figure 4. 3b). Despite this, the $R_2'$ values demonstrate a consistent trend across various datasets, with strong agreement evidenced by $R^2$ values of 0.9970 for mp-Philips, 0.9856 for mp-GE, and 0.9729 for GESSE (Figure 4. 3c).

The stability of the MRI phantom was evaluated by comparing the $R_2$' values measured within a week of preparation to those measured one month later (Figure 4.5). The scatter plot illustrates to some extent a good agreement between the two sets of $R_2$' measurements for the lower volume fraction of glass bubble but slightly lower $R_2$' values for the high glass bubble volume fraction. Additionally, the statistical analysis reveals an $R^2$ value of 0.9361, indicating that approximately 93.61% of the variance in the post-month measurements is explained by the week-one measurements. However, five ROIs (Vf=0.3,0.4,0.5,0.6 and 2%) were excluded from this analysis due to the presence of artefacts or noise that distorted the $R_2$ measurements (see Table 4.2 for volume fraction of sample included in figure 4.5).

| **Glass bubble Vf %** | **Reference $R_2$' Hz** | **mp-Philips $R_2$' Hz** | **mp-GE $R_2$' Hz** | **GESSE $R_2$' Hz** |
|---|---|---|---|---|
| **0** | 3.01 | 3.90 | 0.19 | 3.80 |
| **0.1** | 3.02 | 5.00 | 1.07 | 1.57 |
| **0.2** | 4.11 | 5.95 | 0.67 | 2.34 |
| **0.3** | 7.61 | 9.00 | 3.22 | 4.78 |
| **0.4** | 11.90 | 13.09 | 5.54 | 5.31 |
| **0.5** | 11.17 | 12.98 | 7.40 | 7.21 |
| **0.6** | 11.26 | 14.15 | 10.05 | 9.41 |
| **0.7** | 14.81 | 17.07 | 12.17 | 12.24 |
| **0.8** | 15.91 | 19.11 | 12.19 | 15.01 |
| **0.9** | 20.54 | 24.02 | 16.25 | 19.29 |
| **1** | 24.04 | 25.76 | 19.84 | 18.91 |
| **2** | 45.96 | 51.06 | 38.12 | 42.49 |

**Table 4.1 $R_2$' values.** Measurements across different acquisition approaches and vendors**.** Reference $R_2$’ refers to the single-spin echo turbo spin echo (TSE) and multi-echo gradient echo (mGRE) sequences with a single-slice acquisition. mp-Philips $R_2$’, refers to the 3-dimensional gradient- and spin-echo (3D-GRASE) and multi-echo gradient echo (mGRE) sequences. The mp-GE $R_2$’ is from the T2MAP multiple spin echo and mGRE sequences. $R_2$’ GESSE, refer to the $R_2$’ measurement from the gradient echo sampling of spin echo (GESSE) pulse sequence.

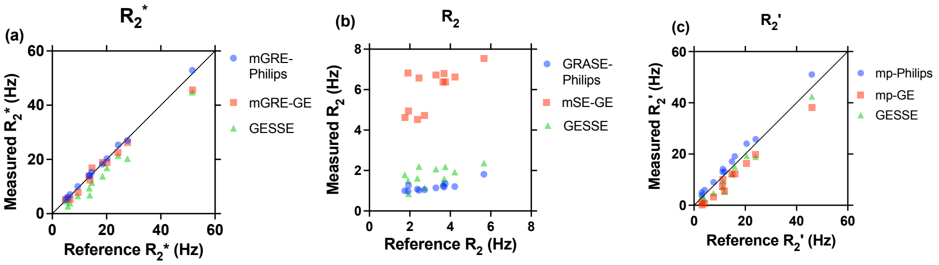

**Figure 4.4 MRI Sequence comparison measurements.** Plots of the measurements of $R_2^*$, $R_2$ and $R_2'$ from the reference data (SE and mGRE Philips) against the 3D-GRASE-mGRE Philips and mSE-mGRE GE data and GESSE Philips data. (a) Reasonable agreement is seen between mGRE datasets, but (b) poor agreement is found between the measurements of $R_2$. (c) Despite this the $R_2'$ values show a similar trend for both 3D-GRASE-mGRE Philips and mSE-mGRE GE (Figure 4.3c).

| Glass Bubble % | $R_2'$ (Hz) within week | $R_2'$ (Hz) after month |
|---|---|---|
| **0** | 3.01 | 4.73 |
| **0.1** | 4.10 | 3.62 |
| **0.2** | 11.26 | 10.86 |
| **0.7** | 14.81 | 11.83 |
| **0.8** | 15.90 | 12.41 |
| **0.9** | 20.53 | 14.13 |
| **1** | 24.04 | 15.09 |

**Table 4.2 . Phantom stability.** $R_2'$ values measured within a week of preparation of the phantom to those measured one month later. Measurements were taken from the reference scan single-spin echo turbo spin echo (TSE) and multi-echo gradient echo (mGRE) sequences with a single-slice acquisition.

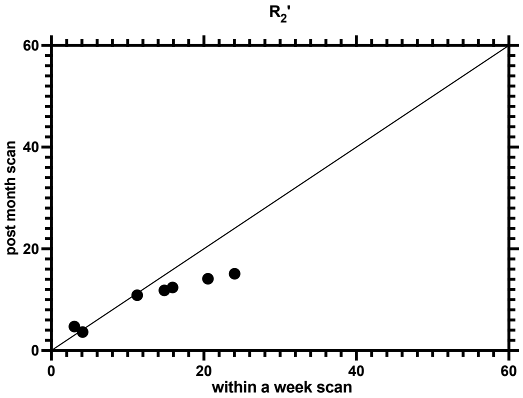

**Figure 4.5 Phantom stability.** Scatter plot comparing $R_2'$ values measured within a week of the phantom preparation to those measured one month later. Measurements were taken from the reference scan single-spin echo turbo spin echo (TSE) and multi-echo gradient echo (mGRE) sequences with the single-slice acquisition.

**Adjustment with Gadolinium**

The addition of gadolinium brought $R_2$ values close to the expected human grey matter values in the phantoms, resulting in a wider range from 12.68 Hz to 29.77 Hz, where typical $R_2$ values for human grey matter are approximately 12.5 Hz. To assess the comparability of the phantoms across different clinically relevant acquisition sequences with the new adjustments, the $R_2$ measurements from the reference data were compared against the 3D-GRASE-Philips, GESSE and mSE-GE data, as shown in Figure 4.6. While the $R_2$ values illustrated better agreements between GESSE, 3D-GRASE-Philips and mSE-GE datasets, as evidenced by the tight clustering of their data points at each reference $R_2$ value, they showed apparent poor agreements with the reference dataset (figure 4.6c). The standard deviations (s.d.) of $R_2$ measurements reveal distinct patterns with and without gadolinium. Without gadolinium, the s.d. values are: reference (1.15 Hz), 3D-GRASE (0.23 Hz), mSE-GE (1.04 Hz), and GESSE (0.46 Hz). This indicates moderate variability in reference (TSE) and mSE-GE, while 3D-GRASE shows high consistency. With gadolinium, the s.d. values change considerably: reference (5.43 Hz), 3D-GRASE (0.51 Hz), mSE-GE (0.43 Hz), and GESSE (0.86 Hz).

For the measurements of $R_2$' across the dataset, a similar trend for the phantom was observed across different sequences (mp-Philips, mp-GE, and GESSE) when compared to the reference measurements (Figure 4.6), with $R^2$ values indicating moderate agreement: 0.6683 for for mp-Philips, 0.6774 for mp-GE, and 0.6397 for GESSE (see Figure 4.6). Similarly, comparison of $R_2$* values from different datasets (mGRE-Philips, mGRE-GE, and GESSE) to the reference $R_2$* values showed good agreement between the measured and reference $R_2$* values (Figure 4.6b), with $R^2$ values of 0.9489 for mGRE-Philips, 0.9569 for mGRE-GE, and 0.8405 for GESSE.

| **Glass bubble Vf %** | **$R_2$ without Gd** | **$R_2$ with Gd** |
|---|---|---|
| **0** | 1.93 | 13.82 |
| **0.1** | 2.72 | 23.49 |
| **0.2** | 2.38 | 29.77 |
| **0.3** | 1.75 | 16.77 |
| **0.4** | 1.91 | 12.68 |
| **0.5** | 2.45 | 13.51 |
| **0.6** | 3.29 | 19.07 |
| **0.7** | 3.70 | 22.40 |
| **0.8** | 4.22 | 22.50 |
| **0.9** | 3.75 | 25.15 |
| **1** | 3.65 | 15.10 |
| **2** | 5.66 | 15.88 |
| **mean** | 3.12 | 19.18 |
| **standard deviation** | 1.15 | 5.43 |

**Table 4.3 $R_2$ with and without gadolinium.** $R_2$ values for the reference scan single-spin echo turbo spin echo (TSE) sequence with the single-slice acquisition for the phantom with and without gadolinium for each region of interests. The addition of the gadolinium elevates the $R_2$ values significantly.

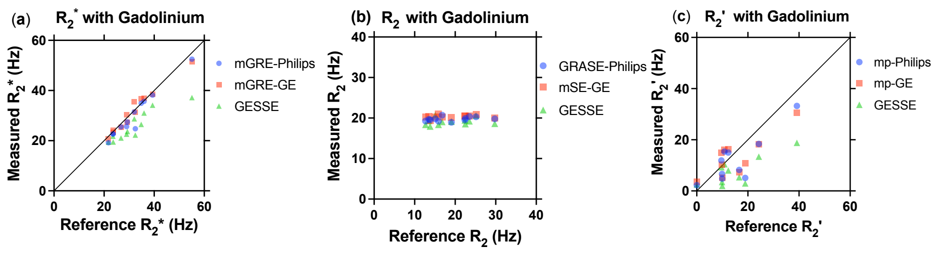

**Figure 4.6 Phantom with gadolinium values across MRI sequence.** The measurements of $R_2$', $R_2$* and $R_2$ from the reference data against the 3D-GRASE - mGRE Philips and mSE-mGRE GE data with added gadolinium to the phantom. (a) $R_2$' values demonstrate a similar trend across different sequences (mp-Philips, mp-GE, and GESSE) when compared to the reference measurements, with a notable deviating more from the reference as $R_2$' increases. (b) $R_2$* data displayed good agreement. (c) $R_2$ data points show a cluster around the reference values with minimal spread, indicating some consistency in measurements across 3D-GRASE-Philips, mGE-GE, and GESSE but exhibiting apparent differences from the reference dataset.

**Commented [AA10]:** Comment 12.

### Characterising $R_1$ in the phantom with and without Gadolinium.

$R_1$ was assessed in the phantom with and without gadolinium. $R_1$ without gadolinium was in the range of 0.44-0.46 Hz, which is equivalent to $T_1$ between 2220 ms to 2170 ms. However, with the addition of the gadolinium, $R_1$ is increased to be in the range of 17.92-19.16 Hz, equivalent to $T_1$=52.17 ms to 57.64 ms. While the primary aim for adding gadolinium to the phantom was to improve $R_2$ values, the impact on $R_1$ was also assessed. The addition of gadolinium significantly increased the relaxation rate $R_1$ and decreased $T_1$ across all measured phantoms. Specifically, the mean $R_1$ without gadolinium was 0.45 Hz (equivalent to $T_1$ = 2220 ms), with a standard deviation of 0.01 Hz, while the mean $R_1$ with gadolinium was 18.23 Hz (equivalent to $T_1$ = 54.9ms), with a standard deviation of 0.45 Hz. This represents an increase by a factor of approximately 40 times for the mean $R_1$ value with gadolinium and shows higher variability in the presence of gadolinium. However, both datasets show poor correlation of $R_1$ with beads percentage, as evidenced by extremely low $R^2$ values (0.05 without Gd, 0.00 with Gd). Figure 4.7. illustrates $R_1$ values with and without Gd versus glass bubble fraction, showing consistently low $R_1$ values without gadolinium across all ROIs.

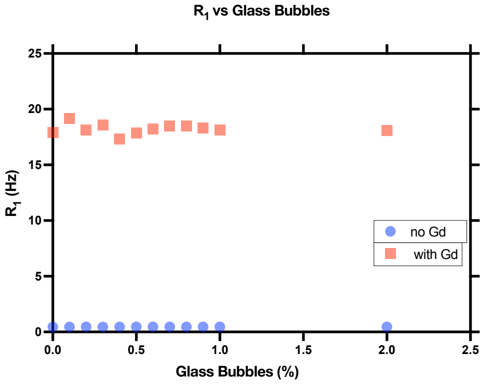

**Figure 4.7 Relaxation rate of $R_1$ for the phantom with and without gadolinium.**

### 4.4.Discussion

The initial objective of this study was to produce an $R_2'$ phantom for quality assurance of $R_2'$ measurements across different quantitative BOLD MRI acquisition approaches and for multicenter harmonization. To this extent, microscopic glass bubbles were investigated to generate $R_2'$ contrast in a phantom by inducing subvoxel magnetic susceptibility variation that mimics the qBOLD MRI signal. In addition, multiparametric qBOLD acquisitions between two MRI vendors were also compared using the newly produced phantom. A strong $R_2'$ contrast was found as a function of glass bubble volume fraction, suggesting that the presence of glass bubbles significantly influences the $R_2'$ parameter, which could be attributed to an alteration in the local magnetic environment caused by the air-filled spaces of the glass bubbles. Furthermore, the phantom showed consistent construction and repeatability of MRI measurements. These results support the reliability of the experimental procedures and emphasise the significance of reproducibility, a crucial aspect in phantom construction [188]. Additionally, the microscopic glass bubbles used in this study offer a cost-effective option compared to precision polystyrene microspheres which have been used previously [189]. The glass bubble cost is approximately £100 for 2 liters, whereas precision polystyrene microspheres cost around £120,000 for 2 liters. Moreover, the size of the glass bubble (60 μm) has more advantages in achieving the targeted sub-voxel magnetic susceptibility variation compared to 280 μm fishing line used in previous work [46].

**Phantom Developments**

The impact of the volume fraction percentage (Vf %) of glass bubbles on $R_2'$ values is clearly demonstrated by the data. As the percentage of glass bubbles increases, there is a significant rise in $R_2'$ values, ranging from 17.82 Hz at a volume fraction of 1% to 56.39 Hz at 3%. Hence, it was possible to achieve targeted $R_2'$ values that replicate those typically observed in the human brain [49], ranging from 1.8 Hz to 4.8 Hz, by using very low volume fractions, such as 0.1%-0.3%.

As $R_2'$ is acalculated as $R_2^*$ - $R_2$, it is important to investigate the behaviour of these two parameters in the produced phantom. $R_2^*$ values were approximately in the range of a normal healthy brain ($R_2^*$= 4.94-51.61), which is typically in the human brain between 15 Hz and 18.3 Hz for grey matter [193]. However, $R_2$ values were found to be very small $R_2$= 1.93-5.66 Hz. Hence $R_2^*$ measurements in this phantom are dominated by $R_2'$ contrast. In an attempt to obtain more typical brain $R_2$ values, the gel was doped with gadolinium which is known to increase $R_2$ and shorten $T_2$ [194]. Hence, more realistic $R_2$ values (12.68-29.77 Hz) were achieved. $R_2$ values in the human brain around 6.4-13.2 Hz for grey matter [193].

**Commented [AA11]:** Comment 11.

Phantom stability over time is an important feature to ensure reliability and consistent measurement [188]. The produced phantom has a promising stability feature; though $R_2'$ values were lower after a month for larger volume fractions, the correlation between the one-week scan after phantom preparation and the scan after a month was good. However, the observed lower $R_2'$ values after a month maybe due to the glass bubble precipitation to the top. One potential solution to address the precipitation issue could involve identifying the ideal gel viscosity to evenly suspend the glass bubbles and prevent them from settling or clustering over time, although it may be challenging to achieve. Another beneficial solution would be exploring the use of a surfactant as a stabilizing agent to prevent the glass bubbles from settling or clustering such as Tween-20 [195].

Characterizing $R_1$ in the phantom, despite its primary design for the study of $R_2'$, provides several benefits. These include a comprehensive understanding of relaxation processes, insights into the inter-relationship of relaxation rates, and potential future applications. The $R_1$ values observed in Figure 4.7 with and without gadolinium showed consistent values and no correlation with the glass bubble fraction, which aligns with the expected outcomes, despite the increased variability introduced by the gadolinium, possibly due to increased magnetic susceptibility caused by the addition of the gadolinium. Furthermore, after the introduction of gadolinium, the $R_1$ values became so small that they no longer reflect typical values found in the human brain, which is due to the gadolinium effect on $R_1$ [194]. At this stage, having a very short $R_1$ is advantageous as it is crucial for eliminating contamination in $T_2/R_2$ measurements. Controlling $R_1$ and $R_2$ independently was demonstrated by Schneiders [196] by selecting appropriate pairs of paramagnetic ions. Specifically, they used solutions of manganese chloride ($MnCl_2$) and nickel chloride ($NiCl_2$) to match target $R_1$ and $R_2$ values. Their results showed that these solutions successfully achieved the desired relaxation rates with minimal error and may be an option for targeting values of $R_1$ and $R_2$ consistent with the human brain.

### Phantom validation across qBOLD acquisitions and MRI vendors.

The results of our study indicate the effective use of the newly developed phantom for assessing $R_2'$ contrast. By scanning the phantom across two different MRI vendor platforms and employing mp-qBOLD and GESSE qBOLD acquisition approaches, we were able to evaluate the phantom's performance under a range of conditions that reflect the diversity encountered in clinical and research settings. The good consistency of $R_2'$ values obtained from these scans highlights the phantom's reliability and its potential role as a consistent tool for quality assurance and calibration for qBOLD acquisitions. However, the addition of gadolinium to the phantom has led to a slight decrease in $R_2'$ values. This could be due to an increase in gel susceptibility, reducing the susceptibility difference between the air inside the glass bubbles and the gel and hence reducing the $R_2'$ effect. $R_2^*$ measurements showed reasonable agreement between mGRE datasets in both cases with and without gadolinium.

$R_2$ measurements showed poor agreements between datasets without gadolinium, but the addition of the gadolinium improved the consistency across $R_2$ values from 3D-GRASE-Philips, mSE-GE and GESSE. Despite this improvement, there was a lack of agreement with the reference data (TSE), which suggests that these clinical sequences may be fundamentally limited in their ability to accurately quantify $R_2$. This limitation is particularly critical for qBOLD applications, as $R_2$ is essential for calculating $R_2'$ ($R_2^*$ - $R_2$) and subsequently OEF. Any systematic error in $R_2$ directly propagates into the OEF calculation,

**Commented [AA12]:** Comment 12.

potentially affecting the validity of oxygen extraction measurements. The discrepancies may also be due to the unique characteristics of TSE, which involves complex echo pathways from multiple refocusing pulses [197] and it's sensitivity to $B_1$ inhomogeneities, especially in such a phantom, could affect $R_2$ quantification [198]. In addition, it is important to note that some degree of discrepancy between quantitative $T_2$ measurements obtained from different MRI pulse sequences is expected and has been highlighted in the literature [187], but researchers should be aware of how these differences might impact the validity of OEF quantification in clinical applications.

### 4.5.Strength and limitations

Our phantom design using glass bubbles (60 μm) presents some limitations compared to brain capillaries (5-10 μm). While both fall within Yablonskiy's mesoscopic regime (5-200 μm) [7,46], our larger bubbles may overestimate mesoscopic effects and cause faster signal decay than typical brain tissue. Additionally, we used spherical bubbles to model cylindrical blood vessels, with volume fractions (0-2%) lower than physiological blood volume fractions ( ~3%). This discrepancy stems from the higher magnetic susceptibility of glass bubbles compared to deoxygenated haemoglobin. To address these issues, we focused on matching expected $R_2'$ values of gray matter rather than replicating exact blood vessel volume fractions. Despite these limitations, our approach offers a practical method for creating controlled $R_2'$ contrast for qBOLD calibration and standardisation.

While adding gadolinium improved $R_2$ values to the expected range in the human brain, it resulted in unrealistically shortened $T_1$ values. One potential solution would be to consider using two compartments to control $R_1$ and $R_2$ independently as suggested by Schneiders [196]. Nonetheless, these findings highlight the challenges in precisely replicating tissue properties in phantom studies and emphasise the importance of careful interpretation when extrapolating phantom results to in vivo conditions.

Another limitation of this study was the persistent discrepancy in $R_2$ measurements between the reference TSE sequence and other sequences (3D-GRASE, mSE-GE, and GESSE), even after gadolinium addition. Future work may consider conducting a systematic comparison of $R_2$ measurements across multiple sequences (TSE, GRASE, GESSE, mSE-GE) using a range of well-characterised phantoms and in vivo tissues. This could help identify consistent patterns in how TSE differs from other sequences. In addition, investigation into how modifying TSE parameters (e.g., echo train length, refocusing pulse flip angles, echo spacing) affects $R_2$ measurements could lead to an optimised TSE protocol that produces results more consistent with other sequences.

Improving stability over time is still an issue in the produced phantom. Accounting for agents that control any growth of bacteria was not considered in this study and is recommended to improve phantom use for a longer time. Another solution to prolong the lifespan of the phantom and avoid glass bubble precipitation is heating the tubes and mixing them using a vortex mixer. However, it is important to note that vigorous mixing might generate bubbles, which also affect $R_2'$. Also, future work should include other sequences that provide a direct measurement of $R_2'$, such as asymmetric spin echo (ASE).

### 4.6. Future implications

The development of such a phantom holds significant future implications for the clinical application of qBOLD techniques. As qBOLD techniques can yield a wide range of $R_2'$ values (2.60 – 8.10Hz) [199], with some techniques providing estimates at the lower end of the scale, such as ASE, and others provides estimates at the higher end, such as mp-qBOLD, creating a phantom with fixed, unchanging $R_2'$ values will have a significant impact on quality assurance. By enabling the use of various acquisition methods and ensuring consistent, unchangeable measurements, this phantom will enhance the reliability and accuracy of qBOLD. Serving as a robust tool for quality assurance, it will accelerate the clinical transition and adoption of this technique, ultimately improving patient outcomes and advancing the field of medical imaging.

### 4.7. Conclusion

Phantom measurements have the advantage of providing unchanging values for parameters, hence, this study aimed to develop and validated an MRI $R_2'$ contrast phantom. To this extent a phantom was developed using glass bubbles. This phantom was investigated with two common qBOLD acquisitions (GESSE, mp-qBOLD) on systems from two different vendors. The study found a linear relationship between the $R_2$' contrast and the glass bubble volume fraction. In addition, the results showed a good agreement in $R_2$' measurements across the different qBOLD acquisitions and vendors when the $R_2$ is reduced to in vivo levels by the addition of gadolinium. The phantom accurately replicated the known in vivo $R_2$' values for the human brain. The study suggests that this phantom could be a valuable tool for site qualification in clinical trials, acceptance testing, and periodic quality assurance for qBOLD applications aimed at quantifying OEF. Additionally, it could help to harmonize qBOLD data collected as part of multi-center clinical trials.

# 5.Improving oxygen extraction fraction estimation with a robust deoxygenated blood volume quantification under hyperoxia condition and multiparametric qBOLD approach.

**Acknowledgements:**

Sebastian Rieger (University of Oxford) for helping with building the gas delivery system, Susan Francis (University of Nottingham) for setting up the TRUST protocol, and Gabriel Hoffman and Stefan Kaczmarz (Technische Universität München) for their insightful thoughts and discussion about merging the techniques of mp-qBOLD and hyperoxia-BOLD.

## 5.1.Introduction

The oxygen extraction fraction (OEF) of brain tissue reports on the balance between oxygen delivery and consumption and can be used to evaluate variations in physiological homeostasis. Subtle changes in OEF may reflect physiological disturbance, and an approach to rapidly and noninvasively assess this parameter should be useful for the clinical assessment of brain homeostasis. The quantitative blood oxygenation level dependant (qBOLD) technique reflects focal changes in OEF. The qBOLD technique can be performed using different acquisition approaches such as the asymmetric spin echo (ASE) and gradient echo sampling of the spin echo (GESSE) techniques. However, ASE and GESSE acquisitions require high SNR, which leads to long acquisition times. In addition, it has previously been reported that DBV is overestimated using ASE [51] leading to lower OEF estimates. The qBOLD method for measuring deoxygenated blood volume (DBV) is vulnerable to various potential confounding factors, such as signals that come from intravascular blood [50], the effects of diffusion narrowing [79] and signals that originate from macro-molecules [52]. Regardless of the specific factors causing the overestimation of DBV, it is crucial to improve the precision of DBV measurements to enhance the accuracy of oxygen extraction fraction (OEF) measurements using qBOLD. A potential solution to these problems is to replace the qBOLD estimate of DBV with a separate independent measure of cerebral blood volume (CBV) by utilising the dynamic susceptibility contrast (DSC) perfusion imaging technique, an idea originally introduced in the multiparametric-qBOLD (mp-qBOLD) approach [200]. DBV, however, represents the deoxygenated blood volume, with veins typically being the major contributor. As a result, there is a disparity between CBV from DSC, which is sensitive to all vessel types and can be thought of as a measure of total blood volume, and DBV, which is localised to vessels holding deoxygenated blood, such as veins and the pre-venous part of the capillaries [75]. One alternative option to DSC based measurements of CBV is to use hyperoxia-BOLD contrast to measure venous CBV (CBVv). It has been demonstrated that the fractional increase in the BOLD signal in response to the administration of oxygen is specific to CBVv and can be scaled to deliver quantitative estimates using a heuristic model [164]. The importance of precise DBV measurement in qBOLD-based OEF quantification was emphasized in Stone and Blockley's work [51,166,182]. They found that measuring DBV separately resulted in significantly better agreement with a $T_2$-Relaxation-Under-Spin-Tagging (TRUST) measurement of global OEF, when compared to those obtained using DBV values estimated from the ASE signal alone. However, the ASE technique is not widely available, whereas the multiparametric approach (mp-qBOLD) has wide clinical availability. Therefore, the aim of this study is to improve OEF estimation with a robust DBV quantification that is suitable for clinical research by using widely available pulse sequences and more precise non-invasive measurements of DBV. Hence, the first objective of this study is to implement a more clinically applicable measurement of OEF by using independent measurements of DBV via hyperoxia-BOLD, which provides a robust and non-invasive way to measure DBV combined, with the application of the mp-qBOLD approach, which is the most common technique used in clinical settings per the scoping review findings (Chapter 2). The second objective is to assess the accuracy of this new approach, Hyperoxia-mp-qBOLD (hmqBOLD), by comparing measurements of OEF with the GESSE approach and TRUST imaging. Additionally, calculating the DBV-based hyperoxia was investigated with the GESSE technique.

## 5.2.Methods

A variety of non-invasive MRI scanning techniques were used as part of this study, including $T_2$-Spin echo, $T_2$*-Gradient echo to calculate the mp-qBOLD data, anatomical brain data, BOLD echo planar imaging (EPI) data for the hyperoxia experiment, TRUST to assess the global OEF level of the brain, and GESSE for direct measurement for $R_2'$. TRUST and GESSE allow us to make comparisons and validations for our new approach. MRI scanning and respiratory stimuli were performed simultaneously. The total time for the experiment was 40 minutes.

Fifteen healthy participants (aged 18-40 years median=28 years, female=8, male=7) were scanned for the hmqBOLD study at the Sir Peter Mansfield Imaging Centre (SPMIC), Nottingham, United Kingdom, under ethical approval from the Faculty of Medicine & Health Sciences Research Ethics Committee. Written consent was obtained from all participants before the experiment. Exclusion criteria consist of contraindications for MRI, pregnancy, chronic obstructive pulmonary disease (COPD), and use of medications.

### Gas stimulus

Participants underwent a mild respiratory stimulus; hyperoxia – an elevated oxygen ($O_2$) level in the blood caused by breathing gas with an elevated oxygen content. In this study, the hyperoxia respiratory stimulus consisted of 100% oxygen for an initial period (60 s) of the oxygen block to accelerate the transition to a steady state and then a switch to a 50:50 mix of air and oxygen (60.5% oxygen) for the plateau period (60 s). Inspired gases were delivered to a face mask at a rate of 15 L/min via a unidirectional breathing circuit adapted from [201] using parts from Intersurgical (Wokingham, UK) (Figure 5.1b). A gas analyser (ML206, ADInstruments, NZ) and data acquisition system (PowerLab 4/35, ADInstruments, NZ) were connected to the face mask via a sampling line and used to obtain continuous recordings of inspired and expired oxygen and carbon dioxide ($CO_2$) concentration throughout the scan (Figure 5.1a). This produced a full respiratory trace from which end-tidal values were subsequently obtained.

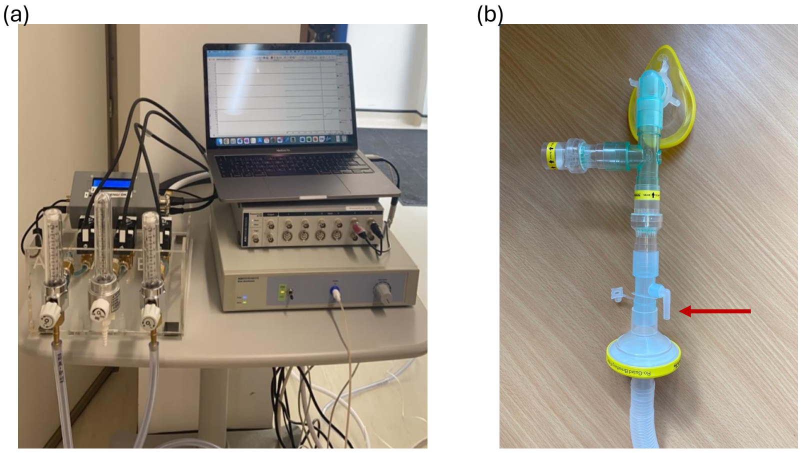

**Figure 5.1 Hyperoxia experiment set up.**(a) A gas analyser and data acquisition system are connected to (b) the face mask via a sampling line and used to obtain continuous recordings of inspired and expired oxygen and $CO_2$ concentration throughout the scan. Red arrow indicates the oxygen hose port for fresh gas delivery.

The gas delivery system consisted of two cylinders: one containing synthetic medical air, and the other containing medical oxygen. Each cylinder was equipped with a pressure regulator and was connected to a variable area flow meter through a solenoid valve. The solenoid valves were controlled by an automated valve controller that was built in-house, programmed with the respiratory paradigm, and activated directly by the MRI scanner. The gases from the flow meters were then directed into the breathing circuit via oxygen hosing (red arrow) as illustrated in Figure 5.1b.

The breathing circuit included a disposable anaesthetic face mask that covers the participant's mouth and nose. The mask was secured by a harness and connected to a sampling port by puncturing it and attaching a barbed luer lock connector. The sampling line was subsequently connected to a data acquisition system for continuous measurement of gas concentrations. The mask was connected to a disposable elbow piece, which was then connected to a disposable T-piece. The T-piece was connected to a one-way outlet valve for expired air and a one-way inlet valve for inhaled fresh gas. A connector for the gas delivery hose was attached to the inlet valve. To prevent cross-contamination, a medical-grade breathing filter was placed at the connection between the disposable circuit and the fixtures. Additionally, the circuit is open to room air through a lengthy corrugated tubing section that acts as a gas reservoir, allowing participants to continue breathing safely in the case of unexpected gas flow interruptions or insufficiencies.

### Imaging

**Commented [AA13]:** Comment 13.

All imaging was acquired using a 3T Ingenia (Philips Healthcare, Best, NL) using the 32-channel head receive coil and body transmit coil. For each participant, foam padding was utilised to stabilise the head and minimise motion. The participants were instructed not to fall asleep during the experiment to prevent any changes in cerebral blood flow and venous oxygenation. Total scan time was 40 minutes.

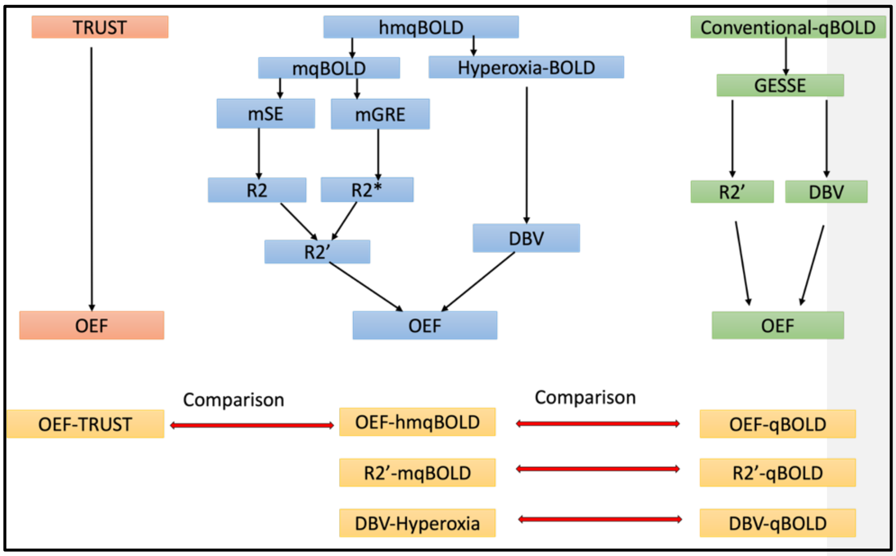

**Figure 5.2 An overview of applied MRI sequences and derived parameters**

**mp-qBOLD**

*3D-GRASE-II:* following the same parameters as [71]. 16 echoes, TE1 = ΔTE= 10 ms; TR= 487 ms; over sampling 1.3; EPI-factor = 7; TSE-factor = 16; α = 90°; 180° refocusing control; 30 slices; voxel size 2.0 x 2.1 x 3.0 $mm^3$; matrix 112 x 91; acquisition time 4:09 min.

***mGRE**:* following the same parameters as [71] 12 echoes, TE1 =ΔTE = 5 ms, TR = 1950 ms, α= 30°, 30 slices, matrix 112 x 92, voxel size 2.0 x 2.0 x 3.0 $mm^3$, total acquisition time 6:08 min.

**Hyperoxia-BOLD**:

Data were acquired using a single-shot EPI acquisition with the following parameters: TR = 3000ms, TE = 30ms, flip angle= 90°, matrix 112 x 110, voxel size 2.0 x 2.0 x 2.0 $mm^3$. The hyperoxia challenge was generated using an electronically controlled gas delivery system (Figure 5.1a) which was automatically triggered by the scanner to adjust oxygen percentage between normoxic and hyperoxic conditions The respiratory paradigm consisted of a two-minute block of normoxia ($O_2$=21 %) interleaved with a two-minute block of hyperoxia ($O_2$=60.5%) repeated twice i.e. normoxia (2 min) – hyperoxia (2 min) – normoxia (2 min) – hyperoxia (2 min) – Normoxia (2 min) Total acquisition scan time 10:12 min. Data were also acquired with a reversed blip direction to be used for distortion correction.

**TRUST**: Acquisition parameters were as the following: TR = 3s, TE = 2.9ms, Bandwidth = 3252 Hz/px, field of view (FOV) = 230 $mm^2$, 64 x 64 matrix.

**T1- weighted**: A 3D-high-resolution structural image was acquired using the following parameters: TR=8 ms, TE = 3.7, flip angle =8°, voxel size 1.0 x 1.1 x 1.0 $mm^3$; matrix 256 x 256; acquisition time 3:43 min

**GESSE**: Following the same parameters as [202], a GESSE sequence was utilized with the following parameters: a field of view (FOV) = 224 x 224 x 59 mm, voxel size= 2 x 2 mm, TE= 80ms, $\Delta$T=0.6ms, number of echoes=75 and TR= 5000 ms. The slice parameters included a thickness of 2 mm, with a 1 mm gap between slices, totalling 20 slices.

**Analysis:**

*Preprocessing:*

The preprocessing steps were performed by a custom shell script to handle the complexities of such multiparametric MRI data, ensuring that the different modalities were aligned and in the same spatial orientation for subsequent analysis. The preprocessing workflow includes several key steps. First, brain extraction was performed on the high-resolution structural image T1-weighted (T1w) image using the bet command from the FMRIB Software Library (FSL) [172].This step isolates the brain from surrounding non-brain tissues, facilitating more accurate registration and segmentation processes. Subsequently, the script aligns the multi-echo spin-echo (3D-GRASE-II) image to the T1w image using the flirt command from FSL. This linear registration process creates a transformation matrix that is later used to convert the T1w mask to 3D-GRASE-II space. To ensure that the transformation is reversible, the script inverts the matrix using the convert_xfm command. Following the registration of 3D-GRASE-II to T1w, the T1w brain mask is transformed to 3D-GRASE-II space and dilated to create a more inclusive mask. This dilated mask is then used in the registration of the multi-echo gradient echo (mGRE) image to the 3D-GRASE-II image, a process that mirrors the 3D-GRASE-II-to-T1w registration.

The script also includes steps for segmentation, where the T1w brain images were segmented into grey matter, white matter and CSF regions of interest (ROI) using the FAST tool from FSL [203]. Additionally, the T1w image is registered to the standard MNI152 space (a common brain template used for spatial normalisation), and the resulting transformation matrix is inverted to allow for the transformation of the MNI cortical atlas to the subject's T1w brain space. To ensure that the different MRI modalities are aligned and in the same spatial orientation, the script applies the appropriate transformations to the grey matter segmentation and the MNI atlas, moving them from standard space to the subject's native space as needed.

Finally, the script prepares the BOLD data and the GESSE data for analysis by registering them to the 3D-GRASE-II image. This alignment is crucial for integrating BOLD and structural information and for the subsequent creation of combined masks that focus on specific regions of interest, such as gray matter.

*Mp-qBOLD data:* Quantitative $T_2$ and $T_2$* maps were calculated using a home-built Matlab script. The script employs a least-squares fitting approach to estimate $T_2$ and $T_2$* from the data acquired using 3D-GRASE-II and mGRE sequences. The relationship between the MRI signal intensity and the echo time (TE) for $T_2$ and $T_2$* relaxation times is modelled by an exponential decay function:

$$\boldsymbol{S(t) = S_0\, exp\,(\frac{-TE}{T_2})} \quad \textbf{Equation 5.1}$$

$$\boldsymbol{S(t) = S_0\, exp\,(\frac{-TE}{T_2^*})} \quad \textbf{Equation 5.2}$$

To facilitate the fitting process, we linearize these models by taking the natural logarithm of both sides:

$$\boldsymbol{ln(S(t)) = ln(S_0) - (\frac{TE}{T_2})} \quad \textbf{Equation 5.3}$$

$$\boldsymbol{ln(S(t)) = ln(S_0) - (\frac{TE}{T_2^*})} \quad \textbf{Equation 5.4}$$

This transformation enables us to use a linear least-squares fitting method, which we implement using the lscov function in MATLAB. This function minimizes the sum of squared differences between observed and predicted values, accounting for errors in both variables.

In both cases, the fitting process yields estimates for the initial signal intensity ($S_0S_0$) and the respective relaxation rates ($1/T_2$ or $1/T_2^*$). Based on $T_2$ and $T_2^*$ maps, maps of $R_2'$ were then calculated using the equation:

$$\boldsymbol{R_2' = \frac{1}{T_2^*} - \frac{1}{T_2}}$$ **Equation 5.5**

*Hyperoxia-BOLD:* For BOLD data, the pre-processing was done using FSL software tools for motion correction (MCFLIRT) [172] and brain extraction [204]. High pass temporal filtering with a cut-off of 240 s and spatial smoothing with a Gaussian kernel with a full width half maximum of 5 mm were applied to the data. The BOLD signal response due to hyperoxia was analysed by using the end-tidal partial pressure of oxygen ($PETO_2$) time-course as a regressor. The recorded $PETO_2$ data were exported from LabChart software as Excel files for further analysis. These files were then imported into MATLAB, where a custom script was developed to identify and extract the $PETO_2$ values along with their corresponding time points. The extracted values were processed to create a regressor aligned with the fMRI data's time points and normalized for use in the General Linear Model (GLM) within the FEAT tool from the FSL. This enabled the prediction and modelling of BOLD signal changes in response to the varying oxygen levels during the experiment, capturing the physiological effects of the hyperoxia stimuli. Then, DBV was calculated from voxel-wise estimates of percentage BOLD signal change ($\delta$S) using Equation 5.6, where A=27 ms, B=0.2, C=245.1 mmHg and D=0.1 [164].

$$\boldsymbol{DBV = \left(\frac{A}{TE} + B\right)\left(\frac{C}{\Delta P_{ET}O_2} + D\right).\partial S}$$ **Equation 5.6**

OEF was then calculated by combining DBV and $R_2'$ parametric maps using Equation 5.7. with known or assumed constants for the susceptibility difference between oxygenated and deoxygenated red blood cells ($\Delta\chi_0 = 0.264 \times 10^{-6}$ [40]) and haematocrit in small vessels (Hct = 0.34 [205]).

$$\boldsymbol{OEF = \frac{R_2'}{DBV.\gamma.\frac{4}{3}.\pi.\Delta\chi_0.Hct.B_0}}$$ **Equation 5.7**

Due to extreme outliers also observed in previous work [51], particularly in the OEF maps, the median values of $R_2'$, DBV and OEF were estimated from voxels in the cortical GM ROIs.

GESSE: data were analysed using a custom-made MATLAB script. The process involved calculating mean signal intensities across echo times for voxels within the brain mask. The spin echo time point (TE(38)) was identified as tau = 0 ms, with the signal split into pre-spin echo (TE(37:1)) and post-spin echo (TE(39:75)) components. $R_2$ ($1/T_2$) was calculated from the ratio of these symmetric gradient echo pairs, followed by removing $R_2$ decay effects. $R_2'$ ($1/T_2'$) was then estimated by fitting the $R_2$-removed signal to tau, where $\tau$ is the time relative to the spin echo point. DBV was calculated from the mismatch between the fitted curve and the actual signal at the spin echo point (tau = 0 ms) (Figure 5.3). Combining $R_2'$ and DBV measurements, estimates of baseline brain oxygenation OEF can be made (Equation 5.7). In addition, DBV-hyperoxia maps were combined with $R_2'$ measurements from GESSE data to calculate OEF-based hyperoxia-GESSE.

**Commented [AA14]:** Comment 14.

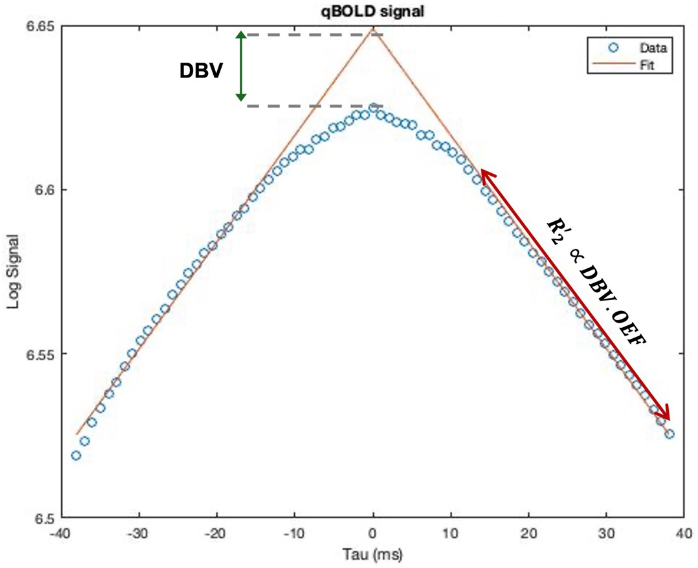

**Figure 5.3 . qBOLD model.** The signal decay according to the qBOLD model and the fitting for a quadratic model to estimate $R_2'$ values, DBV, and OEF.

TRUST

The tag-control images were first corrected for motion using the MCFLIRT tool, which is a linear motion correction tool [206]. Following this, the tag-control images were subtracted from each other in pairs, and the four repetitions at each eTE were averaged. The difference image at eTE = 0 ms was used to identify the four voxels with the highest signal in the superior sagittal sinus (SSS) through an automated registration and masking process, which then defined a region of interest (ROI). Using this SSS ROI, the average difference signal ($\Delta S$) was calculated for each eTE. To determine the $T_2$ of blood ($T_2b$), $\Delta S$ was plotted against eTE and fitted to Equation 5.8 to derive the exponent C [207].

$$\boldsymbol{\Delta S = S_0\ e^{eTE.C}} \quad \textbf{Equation 5.8}$$

$T_{2b}$ was then calculated from C using Equation 5.9 [208], with the assumption that the $T_1$ of blood ($T_{1b}$) is 1624 ms.

$$\boldsymbol{T_{2b} = \frac{1}{\frac{1}{T_{1b}} - C}} \quad \textbf{Equation 5.9}$$

Given a value for haematocrit in large vessels (Hct = 0.42 [209]), $T_{2b}$ can be converted into venous blood oxygenation ($Y_v$) based on the established relationship between oxygenation and $T_{2b}$ [210]. Assuming that arterial blood is fully saturated, an estimate of the whole brain OEF can be obtained by $1-Y_v$.

Quantitative maps of OEF, $R_2'$ and DBV were acquired from conventional qBOLD (GESSE) and Hyperoxia-GESSE (h-GESSE) and compared with the same maps from the newly proposed method hmqBOLD, and whole brain OEF values from TRUST. Figure 5.2 presents an overview of the imaging data acquired, the parameters derived from this imaging data and the main comparisons performed in this study.

*Statistical analysis:*

The statistical analysis was performed using GraphPad Prism (version 10). A one-way ANOVA was conducted to test the null hypothesis of no difference between the OEF estimates from the three measurement methods (TRUST, hmqBOLD, GESSE). If the ANOVA was significant ($p < 0.05$), post-hoc tests (Tukey's HSD) were conducted to determine which specific methods varied from each other. Additionally, Pearson's correlation coefficients were calculated to further explore the relationships between the methods. These correlations assessed the strength and direction of the linear relationship between OEF values obtained using each pair of methods (TRUST vs. hmqBOLD, TRUST vs. GESSE, hmqBOLD vs. GESSE). Bland-Altman plots were used to visually assess correlation and agreement.

## 5.3. Results

**Commented [AA15]:** Comment 16.

Seven participant's data were analysed for OEF and DBV, and 14 participant's data for $R_2$'. A total of 8 participant's data were excluded (movement=1 in hyperoxia-BOLD, failed stim=2 in hyperoxia-BOLD, poor registration=4 and susceptibility artifacts =1 in BOLD data). The median values for $R_2$', OEF, and DBV maps were reported. For OEF, the group mean (±standard deviation) of the TRUST measurements was 35.9±2.1%, the hmqBOLD group mean was 85.9 ± 22.2% and the GESSE group mean was 19.4±2.6%. The hyperoxia-GESSE group mean was 38.1±8.3%. For DBV the group mean of the hmqBOLD measurements was 2.09±0.52% whereas for GESSE the group mean DBV was 3.09±0.55%.

**OEF:**

The one-way ANOVA showed a statistically significant difference between one or more of the TRUST, hmqBOLD, GESSE, and Hyperoxia-GESSE methods for measuring OEF. The results showed that TRUST (mean OEF: 35.9 ± 2.1%, CV: 0.06 %) differed significantly from hmqBOLD (mean OEF: 85.9 ± 22.2%, CV: 0.25%), GESSE (mean OEF: 19.4% ± 2.6%, CV: 0.13) and Hyperoxia-GESSE (mean OEF: 38.08%± 8.30%, CV: 0.21).

Pearson's correlation analysis was carried out to assess the relationships between OEF values obtained using the different methods. The analysis revealed no significant correlation between TRUST and hmqBOLD (r = 0.17, p = 0.7) and between hmqBOLD and GESSE (r = 0.25, p = 0.5). A positive correlation was found between TRUST and GESSE (r = 0.72, p = 0.06) that approached but did not reach statistical significance. The correlation between TRUST and Hyperoxia-GESSE showed a positive relationship (r = 0.53, p = 0.2) that was also not statistically significant. Analysis of the mean differences showed a large positive bias between hmqBOLD and TRUST (OEF hmqBOLD – OEF TRUST = 139.0%). GESSE demonstrated a negative bias compared to TRUST (OEF GESSE – OEF TRUST = -

49.8%), while Hyperoxia-GESSE showed a smaller positive bias (OEF Hyperoxia-GESSE – OEF TRUST = 5.9%).

| | OEF % | | | |
|---|---|---|---|---|
| **Subject No.** | **TRUST** | **hmqBOLD** | **GESSE** | **h-GESSE** |
| **2** | 37.4 | 65.0 | 19.7 | 30.1 |
| **3** | 33.0 | 61.2 | 17.3 | 27.8 |
| **8** | 39.2 | 77.5 | 23.1 | 44.2 |
| **9** | 34.3 | 77.8 | 14.8 | 32.4 |
| **10** | 36.9 | 124.7 | 19.7 | 50.8 |
| **13** | 36.4 | 98.6 | 21.0 | 41.0 |
| **14** | 34.1 | 96.3 | 20.2 | 39.9 |
| **Mean** | 35.9 | 85.9 | 19.4 | 38.08 |
| **std** | 2.1 | 22.2 | 2.6 | 8.30 |
| **CV** | 0.06 | 0.25 | 0.13 | 0.21 |

**Table 5.1 OEF and DBV measurements.** .Values across three methods; hmqBOLD, GESSE, h-GESSE and TRUST. (std):Standard deviation, (CV) coefficient of variation.

**DBV:**

The paired t-test revealed a statistically significant difference ($p<0.05$) between the DBV values obtained using the GESSE and hyperoxia-BOLD methods (mean difference = 1.0%, 95% confidence interval: 0.35– 1.65%). This suggests that the two methods do not yield interchangeable results for DBV measurements. The Bland-Altman analysis further supported this finding, mean bias 1.0% (Figure 5.5), indicating that on average, the GESSE method tended to measure higher DBV compared to hmqBOLD. The limits of agreement (LOA) were wide, ranging from -0.37 to 2.38%, suggesting a significant variability in the difference between the two methods.

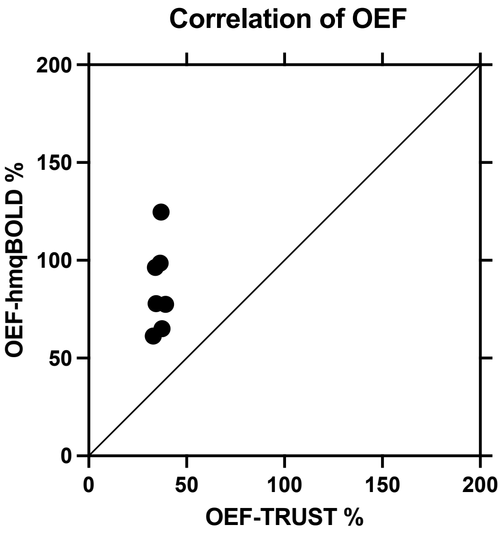

**Figure 5.4 OEF-TRUST versus hyperoxia-mp-qBOLD.** Poor correlation between OEF measurements obtained by TRUST versus hyperoxia-mp-qBOLD (r = 0.17, p = 0.7)). The solid line represents the line of unity. Note that the figure axes extend beyond the physiological range of OEF to accommodate all data points, particularly the overestimated values from hyperoxia-mp-qBOLD.

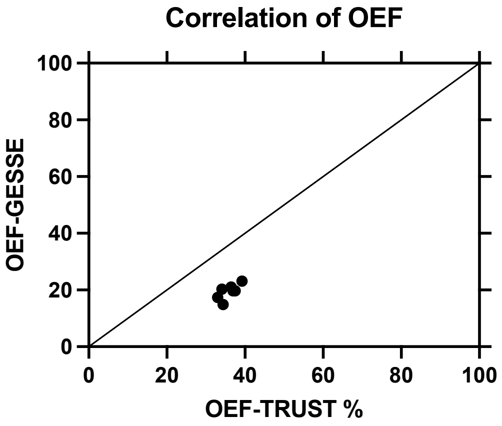

**Figure 5.5 OEF-TRUST versus OEF- GESSE.** Moderate positive correlation between OEF measurements obtained by TRUST versus GESSE data (r = 0.72, p = 0.06). The solid line represents the line of unity.

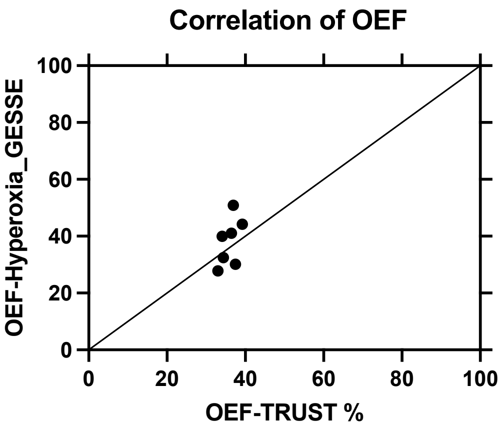

**Figure 5.6 OEF from TRUST versus hyperoxia-GESSE.** . A moderate positive correlation between OEF measurements obtained by TRUST versus hyperoxia-GESSE (r = 0.53, p = 0.2), though not statistically significant. The solid line represents the line of unity.

| **Subject No.** | **DBV- Hyperoxia-BOLD (%)** | **DBV-GESSE (%)** |
|---|---|---|
| **2** | 2.5 | 2.8 |
| **3** | 2.7 | 3.2 |
| **8** | 2.4 | 3.9 |
| **9** | 2.1 | 2.5 |
| **10** | 1.5 | 3.7 |
| **13** | 1.5 | 2.5 |
| **14** | 1.5 | 2.7 |
| **Mean** | 2.09 | 3.09 |
| **SD** | 0.52 | 0.55 |
| **CV** | 0.24 | 0.17 |

**Table 5.2 DBV values.** Mean and standard deviation. DBV maps acquired via Hyperoxia-BOLD and via GESSE data. (SD) standard deviation, (CV) coefficient of variation.

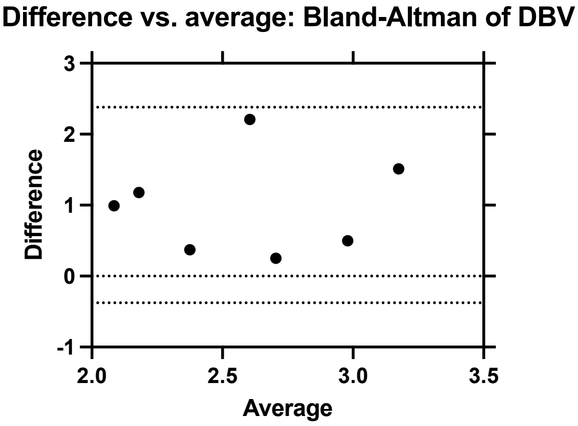

**Figure 5.7 Bland-Altman plot comparing DBV measure of GESSE with DBV measures of hyperoxia-BOLD.** . Mean bias 1.0% and limits of agreement - -0.37 to 2.38%.

### $R_2$'

Analysis of $R_2$' measurements revealed a substantial discrepancy between the GESSE and hmqBOLD methods. The paired t-test demonstrated a highly significant difference (p-value < 0.0001) between the two techniques. On average, the GESSE method yielded $R_2$' values 3.34 Hz lower than hmqBOLD (mean difference = 3.34 Hz). The Bland-Altman analysis supports this observation, the mean bias of -3.34 Hz. This difference is further underscored by the wide limits of agreement (-4.24 to -2.43 Hz). This wide range highlights the significant variability in how much lower the GESSE measurements might be compared to hmqBOLD for individual measurements. Pearson's correlation analysis revealed a statistically significant moderate to strong positive correlation (r = 0.6589, p = 0.0198.) between $R_2$'-GESSE and $R_2$'-mp.

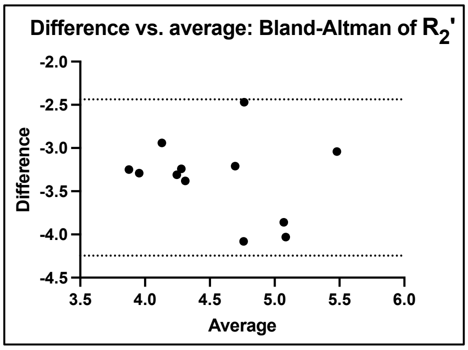

**Figure 5.8 Bland-Altman plot comparing the measure of $R_2$' values of GESSE and the multiparametric qBOLD.** . Mean bias -3.34 Hz and limits of agreement -4.24 to -2.43 Hz.

| Subject No. | $R_2$' GESSE (Hz) | $R_2$' mp-qBOLD (Hz) |
|---|---|---|
| **1** | 3.0 | 6.3 |
| **2** | 2.6 | 5.6 |
| **3** | 2.6 | 5.9 |
| **4** | 2.7 | 6.8 |
| **5** | 3.0 | 7.1 |
| **8** | 3.5 | 6.0 |
| **9** | 2.5 | 5.9 |
| **10** | 3.1 | 7.0 |
| **11** | 2.6 | 6.0 |
| **12** | 3.9 | 7.0 |
| **13** | 2.2 | 5.5 |
| **14** | 2.3 | 5.6 |
| **Mean** | 3.2 | 6.2 |
| **SD** | 0.5 | 0.5 |
| **CV** | 0.15 | 0.08 |

**Table 5.3 $R_2$' values of GESSE and the multiparametric qBOLD.** . (SD) standard deviation, (CV) coefficient of variation.

## 5.4.Discussion

### OEF Estimation

This study explored the use of combining hyperoxia-BOLD, which offers an independent measure of deoxygenated blood volume (DBV), with the mp-qBOLD technique, which is better suited for clinical settings, to generate parametric maps of OEF. To calculate parametric maps of OEF, this technique, referred to here as hyperoxia-mp-qBOLD or hmqBOLD, combines multiparametric relaxometry-based independent measures of the transverse relaxation rates $R_2$ and $R_2$* before calculating the reversible transverse relaxation rate ($R_2$'). Through combining hyperoxia-BOLD derived parametric maps of DBV with mp-qBOLD derived parametric maps of $R_2$', the measures of OEF derived from hmp-qBOLD (ranging from 61.2% to 124.7%) exceed physiological norms (>100%) in the grey matter cortex of healthy individuals, which typically fall between 35% and 55% [211,212]. While the mean OEF value of 85.9% is high but potentially within physiological limits, some individual values exceeded 100% are physiologically implausible. This overestimation might be attributed to several factors. First, the higher $R_2$' values obtained from mp-qBOLD compared to GESSE (mean difference of 3.34 Hz) could contribute to OEF overestimation, as $R_2$' is directly proportional to OEF in the qBOLD model (Equation 5.7). Second, the hyperoxia-BOLD method resulted in lower DBV estimates (mean 1.8% ± 0.6%) compared to GESSE (3.3% ± 0.7%). Given the inverse relationship between DBV and OEF in the qBOLD model (Equation 5.7), underestimation of DBV could lead to OEF overestimation. Third, the lack of isocapnic control during hyperoxia might have induced vasoconstriction [37], potentially altering CBF and affecting the DBV and OEF calculations. Furthermore, the relatively high coefficient of variation in hmp-qBOLD (CV: 0.25) and hyperoxia-GESSE (CV: 0.21) OEF measurements compared to TRUST (CV: 0.06) and GESSE (CV: 0.13) indicates greater variability in these newer techniques, which may be due to the complexity of combining multiple measurements or the sensitivity to physiological variations during the hyperoxia challenge.

### DBV Quantification

The measurements of blood volume across groups using hyperoxia-BOLD (CV=0.24) demonstrate high variability compared to the GESSE-derived DBV measurements (CV=0.17) (Table. 5.2). The range of both approaches (hyperoxia-BOLD =1.5-2.7, GESSE=2.5-3.9 in this study) are reasonably consistent with previous measurements, with hyperoxia-BOLD (ranging from DBV = 1.8 – 2.8 % [164]), and GESSE-derived DBV (ranging from DBV = 3.0 – 4.4, [51]). The DBV obtained through hyperoxia-BOLD was significantly different from that derived from GESSE methods (mean difference = 1.0%, $p<0.05$), indicating that these techniques are not equivalent. The Bland-Altman analysis revealed limits of agreement (-0.37 to 2.38%), suggesting substantial variability between the two methods. It could be that the lower DBV values from hyperoxia-BOLD due to the vasoconstrictive effects of hyperoxia.

**$R_2$' Measurements**

$R_2$' values from GESSE fall within the range of 2.2 - 3.9 Hz, and mp-qBOLD values ranged from 5.5 - 7.1 Hz (Table 5.3). Both of these ranges fall within the values reported in the literature (2.7 for GESSE [49] and 7.2 for mp-qBOLD [71]. In addition, a moderate to strong positive correlation was found between $R_2$' -GESSE and $R_2$' -mp ($r = 0.6589$, $p = 0.0198$), indicating that these measurements tend to increase together. However, the significant difference in $R_2$' measurements between GESSE and hmp-qBOLD (mean difference = 3.34 Hz, $p<0.0001$) remains an important result, even though it was anticipated. This difference likely stems from the inherent characteristics of each method, such as different sensitivities to magnetic field inhomogeneities or microstructural effects [49]. The consistently higher $R_2$' values observed in mp-qBOLD likely contributed to the overestimation of OEF, as previously discussed. This highlights the need for careful consideration of $R_2$' quantification methods in qBOLD approaches. Additionally, researchers and clinicians must be cautious when interpreting absolute OEF values derived from qBOLD techniques, as the choice of $R_2$' quantification method can significantly impact the results, despite the correlation between methods.

**Validation**

The OEF of the whole brain can be measured with minimal assumptions using the Kety-Schmidt method [213]. To do this, venous blood is extracted from the jugular bulb and arterial blood is obtained from the femoral or brachial arteries. For the validation of newly developed MRI techniques, this procedure is rarely feasible due to its invasive nature. The T2-relaxation-under-spin-tagging (TRUST) technique is one alternative. MR-based TRUST is a well-established technique for inferring blood oxygenation levels that have been optimised (Lu et al., 2012; Xu et al., 2012) and tested (Jiang et al., 2018). Thus, TRUST provides a global measurement that is both robust and convenient, and that can be used to benchmark the development of novel methods for mapping brain oxygenation.

The comparison of OEF measurements showed significant differences between the various methods. Hyperoxia mp-qBOLD consistently overestimated OEF compared to TRUST, as indicated by a large positive bias. On the other hand, GESSE showed a negative bias, suggesting an underestimation of OEF compared to TRUST. Importantly, the hyperoxia-GESSE method demonstrated a smaller positive bias, indicating improved accuracy compared to GESSE alone. This highlights the potential advantages of incorporating hyperoxia-based measurements into the GESSE technique, as previously reported using ASE pulse sequence for hyperoxia-qBOLD [166]. However, this approach may not be applicable when using mp-qBOLD, as indicated by the current findings from this study.

**Hyperoxia impact**

The hyperoxic challenge applied in this study was performed without controlling for changes in $PETCO_2$, which may have significant implications for our results, particularly in the estimation of DBV and consequently, OEF.  When subjects breathe high concentrations of oxygen without $CO_2$ regulation (isocapnia), it typically leads to hypocapnia - a decrease in arterial $CO_2$ levels, which is the main driver of cerebral blood flow (CBF) changes during hyperoxia [214]. Similarly, hyperoxia might influence cerebral metabolism ($CMRO_2$) affecting oxygen consumption [215]. Additionally, the resulting hypocapnia can induce a decrease in total cerebral blood volume (CBV) [216]. However, its effect on DBV is more complex as DBV primarily represents the venous and capillary compartments, which may respond differently to hypocapnia compared to the arterial compartment. Nonetheless, the venous compartment may also constrict to some degree, potentially reducing DBV. Hypocapnia could potentially increase the OEF [39], affecting the oxygenated to deoxygenated blood ratio in the venous compartment. Furthermore, the uncontrolled $CO_2$ levels may introduce an additional source of variability in our measurements. Individual differences in respiratory response to hyperoxia could result in varying degrees of hypocapnia, contributing to the high inter-subject variability in our OEF estimates.

**Impact of Analysis Methodology**

Although GESSE-derived $R_2'$ and DBV maps were consistent with the literature [52,79], OEF measurements in this study are considered to be systematically low (ranging from 14.8 – 23%) (Table 5.1) compared to previous work-based GESSE ( around 38%). This may be due to some methodological changes made in this study. Firstly, in this study $R_2'$ maps were calculated following Cox, Gowland [202] which use a simpler model focusing primarily on $T_2$ and $T_2'$ measurements, whereas He, Yablonskiy [52] approach is more comprehensive, incorporating a more complex tissue model and aiming to extract additional physiological parameters beyond just $R_2'$. Secondly, DBV and OEF quantification was derived from a simplified model of the qBOLD signal, inspired by the streamlined approach of Stone, Blockley [51]. The simplification in this analytical approach offers advantages in terms of computational efficiency and ease of implementation, potentially making it more suitable for clinical applications. However, this simplicity may come at the cost of reduced accuracy of OEF measurements. These findings highlight the sensitivity of OEF measurements to specific acquisition and analysis choices, underscoring the need for standardized protocols in qBOLD technique.

## 5.5.Limitations and Future Directions

**Commented [AA16]:** Comment 18.

This study has several limitations that should be considered when interpreting the results. Initially, the sample size was small (n=7), which limits the statistical power and generalizability of the findings. Based on power analysis calculations for correlation studies, assuming a moderate effect size (r=0.5) and standard statistical thresholds (α=0.05, β=0.20), a sample size of approximately 28-30 participants would be needed to reliably detect correlations between different OEF measurement methods. Future studies should aim for this larger sample size to ensure adequate statistical power.

The results presented in this study may have been substantially influenced by the limited sample size, which affected statistical power and reliability. Technical factors, including susceptibility artifacts and failed respiratory stimuli, likely contributed additional variability to the measurements. The combination of restricted sample size and technical challenges can significantly compromise data quality and potentially obscure genuine physiological relationships between different measurement methodologies. While lack of isocapnic control during hyperoxia remains an important physiological consideration, addressing sample size limitations and resolving technical factors may be equally crucial for improving measurement accuracy. Future studies should incorporate larger cohorts and

**Commented [AA17]:** Comment 17.

implement robust quality control procedures to identify and mitigate these technical issues.

$R_2$' measurements, which are susceptible to macroscopic $B_0$ inhomogeneities, were not corrected in this study. Corrections can be achieved either prospectively through methods such as the z-shimming [51,73] or retrospectively by utilizing a high-resolution field map [52]. However, it can be argued that the effect of magnetic field inhomogeneity is reduced by the higher resolution we used (matrix 112 × 92, voxel size 2.0 × 2.0 × 3.0 mm³). This smaller voxel size potentially minimises within-voxel field variations, thereby mitigating distortion effects on $R_2$' measurements without requiring additional correction steps. Furthermore, the presence of partial volumes of cerebrospinal fluid (CSF) was not corrected, which could result in an overestimated measurement of $R_2$' [51]. Future studies should address this by implementing CSF suppression techniques, such as a FLAIR preparation module in the mp-qBOLD sequence, and quantifying the impact on $R_2$’ measurements.

In addition, the significant positive correlation between $R_2$' measurements from GESSE and mp-qBOLD methods and the systematic difference in their values highlights both a limitation and an opportunity for future research. The moderate to strong correlation suggests that a scaling approach could potentially harmonise these measurements. Future studies could explore the possibility of scaling $R_2$'-mp-qBOLD results to match those of TRUST. This harmonisation could improve the accuracy and consistency of OEF estimations across different qBOLD techniques. A calibration study comparing these methods against TRUST measurements in a larger cohort would help establish appropriate scaling factors and validate this approach.

Another limitation is that we only considered the brain at rest. Since OEF is expected to be similar across healthy participants in resting state, our data is likely clustered around a single point, making it challenging to observe a clear linear correlation between different measurement techniques. Future studies should include pharmacological challenges such as acetazolamide administration (targeting a 30-40% increase in CBF) or controlled hypercapnia (5% $CO_2$) to modulate blood flow. These interventions would provide a broader range of OEF values, enabling more robust method comparison and validation.

### 5.6.Conclusion

This study explored the integration of mp-qBOLD and hyperoxia-BOLD to develop more accurate, non-invasive and clinically implementable technique for mapping OEF. These improvements should facilitate the use of the qBOLD technique in clinical settings. Despite the current overestimation, the hmqBOLD method demonstrates the potential for non-invasive OEF quantification. The combination of mp-qBOLD for $R_2'$ measurement and hyperoxia BOLD for DBV estimation addresses some limitations of standard qBOLD, such as the interdependence of $R_2'$ and DBV measurements. The observed overestimation suggests high sensitivity to oxygenation changes, which could be advantageous if properly calibrated. Future work should focus on addressing the identified limitations, particularly the need for larger sample sizes, as well as controlling for physiological confounds during hyperoxia and investigating the accuracy of $R_2'$ measurements in the mp-qBOLD technique.

# 6.Conclusion and future work

The primary aim of this thesis was to enhance the clinical applicability of quantitative Blood Oxygenation Level Dependent (qBOLD) MRI techniques for measuring brain oxygenation. The specific objectives were as follows: first, to comprehensively map the current landscape of qBOLD literature through a scoping review. Second, to develop and validate a phantom for qBOLD measurements, enabling quality assurance and multi-centre harmonisation. Third, to explore the combination of hyperoxia-BOLD and multiparametric qBOLD (mp-qBOLD) techniques to improve oxygen extraction fraction (OEF) estimation in a clinically translatable manner.

## 6.1.Summary of Findings

A scoping review of qBOLD studies in humans was carried out in Chapter 3 and revealed the progress of the technique towards clinical translation. The review identified 93 studies including 3,239 subjects, demonstrating the growing application of qBOLD. The technique showed potential for measuring tissue oxygenation non-invasively and was applied in various clinical populations, particularly in cerebrovascular diseases and brain tumours, indicating its biological validity. qBOLD measurements, particularly OEF, showed sensitivity to pathological changes in conditions such as ischaemic stroke, gliomas, and sickle cell anaemia. This indicates that the technique could be useful in detecting disease-related alterations in tissue oxygenation and potentially monitoring disease progression or treatment response. Four main qBOLD acquisition methods were identified: multiparametric (mp-qBOLD), asymmetric spin echo (ASE), gradient echo (GRE), and gradient echo sampling of spin echo (GESSE). mp-qBOLD was the most commonly used technique, likely due to its easier implementation in clinical settings. However, the review revealed a variety of methodologies across the literature, leading to variability in measurements. Significant variability was found in $R_2'$ measurements across different acquisition techniques, highlighting the need for standardization. For instance, $R_2'$ estimates from mp-qBOLD were 47% higher than those from GESSE, while ASE measurements were 34% lower. Similar variability was observed in deoxygenated blood volume (DBV) measurements. The review emphasized the need for standardization in qBOLD acquisition and analysis methods to improve comparability between studies and support its clinical translation.

Building on the insights gained from the scoping review in Chapter 3, which revealed variability in $R_2$' measurements across different qBOLD acquisition techniques, Chapter 4 focuses on the development and validation of a qBOLD phantom using glass microspheres to generate $R_2$' contrast. The phantom demonstrated a strong linear relationship between $R_2$' contrast and glass bubble volume fraction, achieving targeted $R_2$' values mimicking human brain tissue at low volume fractions. While initial $R_2$ values were low, the addition of gadolinium improved them to a more realistic range. $R_2$* values were found to be in the range of normal healthy brain tissue. The phantom showed good reproducibility in construction and repeatability in MRI measurements, with promising stability over time. It was successfully validated across two MRI vendor platforms (Philips and GE) and different qBOLD acquisition approaches (mp-qBOLD and GESSE), showing good consistency in $R_2$' values. This validation demonstrated the phantom's potential for standardizing and validating qBOLD measurements across different acquisition methods and MRI vendors.

Chapter 5 detailed the development and evaluation of combining multiparametric quantitative BOLD (mp-qBOLD) and hyperoxia-BOLD techniques to map OEF, referred to as hyperoxia-mp-qBOLD (hmqBOLD). The study compared hmqBOLD with established methods such as TRUST and GESSE. Results showed that hmqBOLD significantly overestimated OEF compared to TRUST, with values ranging from 61.2% to 124%. In contrast, GESSE underestimated OEF, while hyperoxia-GESSE showed improved accuracy. DBV estimates from hyperoxia-BOLD were lower than those from GESSE, with a significant difference between the two methods. $R_2$' measurements from mp-qBOLD were consistently higher than those from GESSE, with a moderate to strong positive correlation between the two.

## 6.2.Contributions to the qBOLD Field

While previous reviews have focused on MRI-based OEF measurement techniques in general [59] or specifically on BOLD-based techniques for quantifying brain hemodynamic and metabolic properties [43], the scoping review performed in this thesis provides the first comprehensive overview of qBOLD experiments across various organs and pathologies. One of its main contributions to the field is that it identifies the prevalent acquisition methods and analysis approaches, highlighting areas of consensus and aspects that need validation and harmonization. For example, the review reveals the need for better standardization of qBOLD acquisition techniques, more consistent reporting of methodology, and further investigation into the sources of variability in $R_2$' and DBV measurements across different qBOLD approaches.

Addressing the need for standardization, the development of a qBOLD phantom using glass microspheres (Chapter 4) represents a significant step forward, offering a cost-effective tool for quality assurance and multi-centre harmonisation [185]. However, the challenge of matching $R_2$ values to the human brain range necessitated the addition of gadolinium, which, while successful in increasing $R_2$ values, introduced new complexities due to extreme $T_1$ shortening.

The exploration of the hmqBOLD approach, while requiring further refinement, represents a new attempt to improve OEF estimation while maintaining clinical feasibility. This study contributes to the field by advancing the integration of hyperoxia-BOLD and mp-qBOLD techniques, building upon previous work on DBV measurement improvements methods [51,54,164]. It provides valuable insights into the complexities of combining multiple qBOLD techniques and highlights the importance of physiological control during hyperoxia challenges in OEF quantification. The potential high sensitivity of hmqBOLD to oxygenation changes, if properly calibrated, could be advantageous in detecting subtle physiological alterations.

### 6.3.Limitations

A potential limitation of this thesis is the absence of the ASE pulse sequence in both the phantom and hyperoxia studies due to challenges in implementing the sequence. Since ASE is commonly used in qBOLD techniques, its absence limits our ability to directly compare our results with a substantial portion of the existing qBOLD literature.

The phantom study encountered challenges in accurately replicating physiological properties, particularly in balancing $R_2$ and $T_1$ values. The long-term stability of the phantom remains a challenge, with reduced $R_2$' values observed after a month, especially for higher bead fractions, likely due to the precipitation of glass bubbles. This settling or clustering of bubbles may impact the consistency and reliability of measurements (Fieremans and Lee, 2018).

In the hyperoxia-mp-qBOLD study, poor registration between high and low resolution images resulted in the exclusion of several datasets, leading to a reduced sample size. The use of 'stepping-stone' images (intermediate resolution images that bridge the gap between high and low resolution data) could potentially improve registration accuracy. While this approach was not feasible in our current dataset as intermediate resolution images were not acquired, future studies could benefit from including such intermediate resolution acquisitions in their imaging protocol to potentially improve registration accuracy and reduce the number of datasets excluded due to poor registration.

**Commented [AA18]:** Comment 15.

### 6.4.Future work

Several important areas for future research have appeared in this work. Refining the phantom design is crucial, focusing on improving long-term stability and more accurately mimicking physiological conditions. This could involve exploring the use of stabilising agents and investigating methods to achieve ideal gel viscosity for even suspension of glass bubbles. To address the $T_1$ shortening issue, alternative contrast agents or multi-compartment models should be explored to control $R_1$ and $R_2$ independently. Standardisation efforts are crucial for translating qBOLD to clinical settings. Following the model of the QIBA Diffusion-Weighted Imaging Profile, developing consensus protocols and establishing guidelines for acquisition, reconstruction, and analysis can ensure consistent and reliable qBOLD measurements across different sites and scanner platforms. Establishing standardised quality control measures, such as the use of quantitative phantoms, is essential for multi-centre harmonisation. This standardisation would enable reliable multi-centre trials and facilitate broader clinical adoption of qBOLD techniques, ultimately improving the comparability and reproducibility of qBOLD measurements across different sites and studies.

The hmqBOLD method requires further optimisation to address OEF overestimation, particularly by implementing isocapnic control during hyperoxic challenges. Exploring scaling approaches to harmonise $R_2'$ measurements across different techniques could improve consistency in OEF estimations. This could be achieved by developing technique-specific calibration factors based on comparative studies. For instance, $R_2'$ measurements from various qBOLD techniques (e.g., ASE, GESSE, mp-qBOLD) could be collected on a cohort of subjects and compared to global OEF values obtained from a validated method like TRUST. By analysing the relationships between these measurements, scaling factors could be derived to adjust $R_2'$ values from different techniques, bringing them into closer alignment with each other and with TRUST-based OEF estimates. These scaling factors could then be implemented in qBOLD analysis software to automatically adjust $R_2'$ measurements, potentially leading to more consistent OEF estimation across techniques. In addition, future research could benefit from simulating pathological conditions, such as inducing hypocapnia or using pharmacological interventions to lower CBF. These manipulations could provide valuable insights into the sensitivity and reliability of hmp-qBOLD technique across a broader range of physiological states, more closely representing the conditions that might be encountered in patient populations, while also allowing for better testing of correlations across a larger range of OEF values.

In summary, this thesis has made important contributions to advancing the clinical applicability of qBOLD imaging. By providing a comprehensive and systematic literature review, developing a quality assurance tool, and investigating a new combined approach for improving the OEF estimation accuracy and practicality, this work has laid an important foundation for future advancements in qBOLD imaging. Given the continuous development of the field, the knowledge and tools obtained from this research will play a crucial role in moving qBOLD closer to clinical application.

## References

1. Maldonado KA, Alsayouri K. Physiology, Brain. In: *StatPearls*. StatPearls Publishing
Copyright © 2024, StatPearls Publishing LLC.; 2024.
2. Ishii K, Kitagaki H, Kono M, Mori E. Decreased medial temporal oxygen metabolism in Alzheimer's disease shown by PET. *The Journal of Nuclear Medicine*. 1996;37(7):1159.
3. Derdeyn CP, Videen TO, Yundt KD, et al. Variability of cerebral blood volume and oxygen extraction: stages of cerebral haemodynamic impairment revisited. *Brain*. 2002;125(3):595-607.
4. Leenders K. PET: blood flow and oxygen consumption in brain tumors. *Journal of neuro-oncology*. 1994;22:269-273.
5. Ito H, Kanno I, Kato C, et al. Database of normal human cerebral blood flow, cerebral blood volume, cerebral oxygen extraction fraction and cerebral metabolic rate of oxygen measured by positron emission tomography with 15O-labelled carbon dioxide or water, carbon monoxide and oxygen: a multicentre study in Japan. *European journal of nuclear medicine and molecular imaging*. 2004;31(5):635-643.
6. Ogawa S, Lee T-M, Kay AR, Tank DW. Brain magnetic resonance imaging with contrast dependent on blood oxygenation. *proceedings of the National Academy of Sciences*. 1990;87(24):9868-9872.
7. Yablonskiy DA, Haacke EM. Theory of NMR signal behavior in magnetically inhomogeneous tissues: the static dephasing regime. *Magnetic resonance in medicine*. 1994;32(6):749-763.
8. Feinberg DA, Oshio K. GRASE (gradient-and spin-echo) MR imaging: a new fast clinical imaging technique. *Radiology*. 1991;181(2):597-602.
9. Yablonskiy DA, Haacke EM. An MRI method for measuring T2 in the presence of static and RF magnetic field inhomogeneities. *Magnetic resonance in medicine*. 1997;37(6):872-876.
10. Ma J, Wehrli FW. Method for image-based measurement of the reversible and irreversible contribution to the transverse-relaxation rate. *Journal of Magnetic Resonance, Series B*. 1996;111(1):61-69.
11. Wismer G, Buxton R, Rosen B, et al. Susceptibility induced MR line broadening: applications to brain iron mapping. *Journal of computer assisted tomography*. 1988;12(2):259-265.
12. Lacerte M, Mesfin F. Hypoxic brain injury. 2019.
13. Kety SS, Schmidt CF. The nitrous oxide method for the quantitative determination of cerebral blood flow in man: theory, procedure and normal values. *The Journal of clinical investigation*. 1948;27(4):476-483.
14. Nicoll D, Lu CM, Pignone M, McPhee SJ. In: *Pocket Guide to Diagnostic Tests, 6e*. New York, NY: The McGraw-Hill Companies; 2012.
15. Powers WJ, Grubb Jr RL, Darriet D, Raichle ME. Cerebral blood flow and cerebral metabolic rate of oxygen requirements for cerebral function and viability in humans. *Journal of Cerebral Blood Flow & Metabolism*. 1985;5(4):600-608.

16. Heiss W-D. The Ischemic Penumbra: Correlates in Imaging and Implications for Treatment of Ischemic StrokeThe Johann Jacob Wepfer Award 2011. *Cerebrovascular Diseases*. 2011;32(4):307-320.
17. Gerstner ER, Zhang Z, Fink JR, et al. ACRIN 6684: assessment of tumor hypoxia in newly diagnosed glioblastoma using 18F-FMISO PET and MRI. *Clinical Cancer Research*. 2016;22(20):5079-5086.
18. Stadlbauer A, Zimmermann M, Kitzwogerer M, et al. MR Imaging-derived Oxygen Metabolism and Neovascularization Characterization for Grading and IDH Gene Mutation Detection of Gliomas. *Radiology*. 2017;283(3):798-808.
19. Ogawa S, Tank DW, Menon R, et al. Intrinsic signal changes accompanying sensory stimulation: functional brain mapping with magnetic resonance imaging. *Proceedings of the National Academy of Sciences*. 1992;89(13):5951-5955.
20. Ogawa S, Menon R, Tank D, et al. Functional brain mapping by blood oxygenation level-dependent contrast magnetic resonance imaging. A comparison of signal characteristics with a biophysical model. *Biophysical journal*. 1993;64(3):803-812.
21. Kwong KK, Belliveau JW, Chesler DA, et al. Dynamic magnetic resonance imaging of human brain activity during primary sensory stimulation. *Proceedings of the National Academy of Sciences*. 1992;89(12):5675-5679.
22. Devlin JT, Matthews PM, Rushworth MF. Semantic processing in the left inferior prefrontal cortex: a combined functional magnetic resonance imaging and transcranial magnetic stimulation study. *Journal of cognitive neuroscience*. 2003;15(1):71-84.
23. Biswal B, Zerrin Yetkin F, Haughton VM, Hyde JS. Functional connectivity in the motor cortex of resting human brain using echo-planar MRI. *Magnetic resonance in medicine*. 1995;34(4):537-541.
24. Smith SM, Fox PT, Miller KL, et al. Correspondence of the brain's functional architecture during activation and rest. *Proceedings of the national academy of sciences*. 2009;106(31):13040-13045.
25. Huettel SA, Song AW, McCarthy G. *Functional magnetic resonance imaging*. Vol 1: Sinauer Associates Sunderland, MA; 2004.
26. Buxton RB, Uludağ K, Dubowitz DJ, Liu TT. Modeling the hemodynamic response to brain activation. *Neuroimage*. 2004;23 Suppl 1:S220-233.
27. Pittman RN. The circulatory system and oxygen transport. In: *Regulation of Tissue Oxygenation*. Morgan & Claypool Life Sciences; 2011.
28. Schenck JF. Magnetic resonance imaging of brain iron. *Journal of the neurological sciences*. 2003;207(1):99-102.
29. Simon AB, Buxton RB. Understanding the dynamic relationship between cerebral blood flow and the BOLD signal: Implications for quantitative functional MRI. *Neuroimage*. 2015;116:158-167.
30. Buxton RB. *Introduction to functional magnetic resonance imaging: principles and techniques*. Cambridge university press; 2009.
31. Uludag K, Ugurbil K, Berliner L. *fMRI: From nuclear spins to brain functions*. Vol 30: Springer; 2015.

32. Davis TL, Kwong KK, Weisskoff RM, Rosen BR. Calibrated functional MRI: mapping the dynamics of oxidative metabolism. *Proceedings of the National Academy of Sciences*. 1998;95(4):1834-1839.
33. Grubb Jr RL, Raichle ME, Eichling JO, Ter-Pogossian MM. The effects of changes in PaCO2 cerebral blood volume, blood flow, and vascular mean transit time. *Stroke*. 1974;5(5):630-639.
34. Chen JJ, Pike GB. MRI measurement of the BOLD-specific flow–volume relationship during hypercapnia and hypocapnia in humans. *Neuroimage*. 2010;53(2):383-391.
35. Mark CI, Pike GB. Indication of BOLD-specific venous flow-volume changes from precisely controlled hyperoxic vs. hypercapnic calibration. *Journal of Cerebral Blood Flow & Metabolism*. 2012;32(4):709-719.
36. Chiarelli PA, Bulte DP, Wise R, Gallichan D, Jezzard P. A calibration method for quantitative BOLD fMRI based on hyperoxia. *Neuroimage*. 2007;37(3):808-820.
37. Bulte DP, Chiarelli PA, Wise RG, Jezzard P. Cerebral perfusion response to hyperoxia. *Journal of Cerebral Blood Flow & Metabolism*. 2007;27(1):69-75.
38. Bulte D, Chiarelli P, Wise R, Jezzard P. Measurement of cerebral blood volume in humans using hyperoxic MRI contrast. *Journal of Magnetic Resonance Imaging*. 2007;26(4):894-899.
39. Xu F, Uh J, Brier MR, et al. The influence of carbon dioxide on brain activity and metabolism in conscious humans. *Journal of Cerebral Blood Flow & Metabolism*. 2011;31(1):58-67.
40. Spees WM, Yablonskiy DA, Oswood MC, Ackerman JJ. Water proton MR properties of human blood at 1.5 Tesla: Magnetic susceptibility, T1, T2, T, and non-Lorentzian signal behavior. *Magnetic Resonance in Medicine: An Official Journal of the International Society for Magnetic Resonance in Medicine*. 2001;45(4):533-542.
41. Kiselev VG, Posse S. Analytical theory of susceptibility induced NMR signal dephasing in a cerebrovascular network. *Physical Review Letters*. 1998;81(25):5696.
42. Fujita N, Shinohara M, Tanaka H, Yutani K, Nakamura H, Murase K. Quantitative mapping of cerebral deoxyhemoglobin content using MR imaging. *Neuroimage*. 2003;20(4):2071-2083.
43. Yablonskiy DA, Sukstanskii AL, He X. Blood oxygenation level-dependent (BOLD)-based techniques for the quantification of brain hemodynamic and metabolic properties - theoretical models and experimental approaches. *NMR in Biomedicine*. 2013;26(8):963-986.
44. Sukstanskii AL, Yablonskiy DA. Theory of FID NMR signal dephasing induced by mesoscopic magnetic field inhomogeneities in biological systems. *Journal of magnetic resonance*. 2001;151(1):107-117.
45. Dickson JD, Ash TW, Williams GB, Sukstanskii AL, Ansorge RE, Yablonskiy DA. Quantitative phenomenological model of the BOLD contrast mechanism. *Journal of Magnetic Resonance*. 2011;212(1):17-25.
46. Yablonskiy DA. Quantitation of intrinsic magnetic susceptibility-related effects in a tissue matrix. Phantom study. *Magnetic resonance in medicine*. 1998;39(3):417-428.

47. Sedlacik J, Reichenbach JR. Validation of quantitative estimation of tissue oxygen extraction fraction and deoxygenated blood volume fraction in phantom and in vivo experiments by using MRI. *Magn Reson Med*. 2010;63(4):910-921.
48. He X, Zhu M, Yablonskiy DA. Validation of oxygen extraction fraction measurement by qBOLD technique. *Magn Reson Med*. 2008;60(4):882-888.
49. Ni W, Christen T, Zun Z, Zaharchuk G. Comparison of R2' measurement methods in the normal brain at 3 Tesla. *Magn Reson Med*. 2015;73(3):1228-1236.
50. An H, Lin W. Impact of intravascular signal on quantitative measures of cerebral oxygen extraction and blood volume under normo- and hypercapnic conditions using an asymmetric spin echo approach. *Magn Reson Med*. 2003;50(4):708-716.
51. Stone AJ, Blockley NP. A streamlined acquisition for mapping baseline brain oxygenation using quantitative BOLD. *Neuroimage*. 2017;147:79-88.
52. He X, Yablonskiy DA. Quantitative BOLD: Mapping of human cerebral deoxygenated blood volume and oxygen extraction fraction: Default state. *Magnetic Resonance in Medicine*. 2007;57(1):115-126.
53. An H, Lin W. Cerebral oxygen extraction fraction and cerebral venous blood volume measurements using MRI: Effects of magnetic field variation. *Magnetic Resonance in Medicine*. 2002;47:958-966.
54. Christen T, Schmiedeskamp H, Straka M, Bammer R, Zaharchuk G. Measuring brain oxygenation in humans using a multiparametric quantitative blood oxygenation level dependent MRI approach. *Magnetic Resonance in Medicine*. 2012;68(3):905-911.
55. Feng X, Deistung A, Reichenbach JR. Quantitative susceptibility mapping (QSM) and R2* in the human brain at 3 T: Evaluation of intra-scanner repeatability. *Zeitschrift für Medizinische Physik*. 2018;28(1):36-48.
56. Hubertus S, Thomas S, Cho JH, Zhang S, Wang Y, Schad LR. Comparison of gradient echo and gradient echo sampling of spin echo sequence for the quantification of the oxygen extraction fraction from a combined quantitative susceptibility mapping and quantitative BOLD (QSM plus qBOLD) approach. *Magnetic Resonance in Medicine*. 2019;82(4):1491-1503.
57. Yamaguchi T, Kanno I, Uemura K, et al. Reduction in regional cerebral metabolic rate of oxygen during human aging. *Stroke*. 1986;17(6):1220-1228.
58. Nagata K, Maruya H, Yuya H, et al. Can PET data differentiate Alzheimer's disease from vascular dementia? *Annals of the New York Academy of Sciences*. 2000;903(1):252-261.
59. Jiang D, Lu H. Cerebral oxygen extraction fraction MRI: Techniques and applications. *Magnetic resonance in medicine*. 2022;88(2):575-600.
60. Gauthier CJ, Hoge RD. Magnetic resonance imaging of resting OEF and CMRO2 using a generalized calibration model for hypercapnia and hyperoxia. *Neuroimage*. 2012;60(2):1212-1225.
61. Bulte DP, Kelly M, Germuska M, et al. Quantitative measurement of cerebral physiology using respiratory-calibrated MRI. *Neuroimage*. 2012;60(1):582-591.
62. Thulborn KR, Waterton JC, Matthews PM, Radda GK. Oxygenation dependence of the transverse relaxation time of water protons in whole blood at high field. *Biochimica et Biophysica Acta (BBA)-General Subjects*. 1982;714(2):265-270.

63. Li W, van Zijl PC. Quantitative theory for the transverse relaxation time of blood water. *NMR in Biomedicine.* 2020;33(5):e4207.
64. Weisskoff RM, Kiihne S. MRI susceptometry: image-based measurement of absolute susceptibility of MR contrast agents and human blood. *Magnetic resonance in medicine.* 1992;24(2):375-383.
65. Haacke E, Tang J, Neelavalli J, Cheng Y. Susceptibility mapping as a means to visualize veins and quantify oxygen saturation. *Journal of Magnetic Resonance Imaging.* 2010;32(3):663-676.
66. Zhang J, Liu T, Gupta A, Spincemaille P, Nguyen TD, Wang Y. Quantitative mapping of cerebral metabolic rate of oxygen (CMRO2) using quantitative susceptibility mapping (QSM). *Magnetic resonance in medicine.* 2015;74(4):945-952.
67. An HY, Lin WL. Quantitative measurements of cerebral blood oxygen saturation using magnetic resonance imaging. *Journal of Cerebral Blood Flow and Metabolism.* 2000;20(8):1225-1236.
68. Arksey H, O'Malley L. Scoping studies: towards a methodological framework. *International journal of social research methodology.* 2005;8(1):19-32.
69. Wiestler B, Kluge A, Lukas M, et al. Multiparametric MRI-based differentiation of WHO grade II/III glioma and WHO grade IV glioblastoma. *Scientific Reports.* 2016;6:6.
70. Sohlin M, Schad LR. Theoretical prediction of parameter stability in quantitative BOLD MRI: dependence on SNR and sequence parameters. Paper presented at: Proceedings of 18th Annual Meeting of ISMRM2009.
71. Kaczmarz S, Hyder F, Preibisch C. Oxygen extraction fraction mapping with multi-parametric quantitative BOLD MRI: Reduced transverse relaxation bias using 3D-GraSE imaging. *Neuroimage.* 2020;220:9.
72. Kaczmarz S, Goettler J, Zimmer C, Hyder F, Preibisch C. Characterizing white matter fiber orientation effects on multi-parametric quantitative BOLD assessment of oxygen extraction fraction. *Journal of Cerebral Blood Flow and Metabolism.* 2020;40(4):760-774.
73. Blockley NP, Stone AJ. Improving the specificity of R2' to the deoxyhaemoglobin content of brain tissue: Prospective correction of macroscopic magnetic field gradients. *Neuroimage.* 2016;135:253-260.
74. Preibisch C, Volz S, Anti S, Deichmann R. Exponential excitation pulses for improved water content mapping in the presence of background gradients. *Magn Reson Med.* 2008;60(4):908-916.
75. Yablonskiy DA, Sukstanskii AL, Luo J, Wang X. Voxel spread function method for correction of magnetic field inhomogeneity effects in quantitative gradient-echo-based MRI. *Magnetic resonance in medicine.* 2013;70(5):1283-1292.
76. Ulrich X, Yablonskiy DA. Separation of Cellular and BOLD Contributions to T2* Signal Relaxation. *Magnetic Resonance in Medicine.* 2016;75(2):606-615.
77. Stone AJ, Holland NC, Berman AJ, Blockley NP. Simulations of the effect of diffusion on asymmetric spin echo based quantitative BOLD: An investigation of the origin of deoxygenated blood volume overestimation. *Neuroimage.* 2019;201:116035.
78. Kiselev V, Posse S. Analytical model of susceptibility-induced MR signal dephasing: effect of diffusion in a microvascular network. *Magnetic Resonance*

*in Medicine: An Official Journal of the International Society for Magnetic Resonance in Medicine*. 1999;41(3):499-509.
79. Dickson JD, Ash TWJ, Williams GB, et al. Quantitative BOLD: The effect of diffusion. *Journal of Magnetic Resonance Imaging*. 2010;32(4):953-961.
80. Levac D, Colquhoun H, O'Brien KK. Scoping studies: advancing the methodology. *Implementation science*. 2010;5(1):1-9.
81. Rumrill PD, Fitzgerald SM, Merchant WR. Using scoping literature reviews as a means of understanding and interpreting existing literature. *Work (Reading, Mass)*. 2010;35(3):399-404.
82. Brien SE, Lorenzetti DL, Lewis S, Kennedy J, Ghali WA. Overview of a formal scoping review on health system report cards. *Implementation Science*. 2010;5(1):1-12.
83. Davis K, Drey N, Gould D. What are scoping studies? A review of the nursing literature. *International journal of nursing studies*. 2009;46(10):1386-1400.
84. Tricco AC, Lillie E, Zarin W, et al. PRISMA extension for scoping reviews (PRISMA-ScR): checklist and explanation. *Annals of internal medicine*. 2018;169(7):467-473.
85. Moher D, Liberati A, Tetzlaff J, Altman DG, PRISMA Group* t. Preferred reporting items for systematic reviews and meta-analyses: the PRISMA statement. *Annals of internal medicine*. 2009;151(4):264-269.
86. Bennani-Baiti B, Pinker K, Zimmermann M, et al. Non-Invasive Assessment of Hypoxia and Neovascularization with MRI for Identification of Aggressive Breast Cancer. *Cancers*. 2020;12(8):14.
87. Bouvier J, Detante O, Tahon F, et al. Reduced CMRO2 and Cerebrovascular Reserve in Patients With Severe Intracranial Arterial Stenosis: A Combined Multiparametric qBOLD Oxygenation and BOLD fMRI Study. *Human Brain Mapping*. 2015;36(2):695-706.
88. Stadlbauer A, Mouridsen K, Doerfler A, et al. Recurrence of glioblastoma is associated with elevated microvascular transit time heterogeneity and increased hypoxia. *Journal of Cerebral Blood Flow and Metabolism*. 2018;38(3):422-432.
89. Stadlbauer A, Marhold F, Oberndorfer S, et al. Metabolic tumor microenvironment characterization of contrast enhancing brain tumors using physiologic mri. *Metabolites*. 2021;11.
90. Stadlbauer A, Oberndorfer S, Heinz G, et al. Hypoxia and Microvascular Alterations Are Early Predictors of IDH-Mutated Anaplastic Glioma Recurrence. *Cancers*. 2021;13(8):17.
91. Stadlbauer A, Zimmermann M, Doerfler A, et al. Intratumoral heterogeneity of oxygen metabolism and neovascularization uncovers 2 survival-relevant subgroups of IDH1 wild-type glioblastoma. *Neuro-Oncology*. 2018;20(11):1536-1546.
92. Stadlbauer A, Zimmermann M, Bennani-Baiti B, et al. Development of a Non-invasive Assessment of Hypoxia and Neovascularization with Magnetic Resonance Imaging in Benign and Malignant Breast Tumors: Initial Results. *Molecular Imaging and Biology*. 2019;21(4):758-770.
93. Heynold E, Zimmermann M, Hore N, et al. Physiological MRI Biomarkers in the Differentiation Between Glioblastomas and Solitary Brain Metastases. *Molecular Imaging and Biology*. 2021;23(5):787-795.

94. Stadlbauer A, Heinz G, Oberndorfer S, et al. Physiological MRI of microvascular architecture, neovascularization activity, and oxygen metabolism facilitate early recurrence detection in patients with IDH-mutant WHO grade 3 glioma. *Neuroradiology.* 2022;64(2):265-277.
95. Stadlbauer A, Kinfe TM, Eyupoglu I, et al. Tissue Hypoxia and Alterations in Microvascular Architecture Predict Glioblastoma Recurrence in Humans. *Clinical Cancer Research.* 2021;27(6):1641-1649.
96. Stadlbauer A, Marhold F, Oberndorfer S, et al. Radiophysiomics: Brain Tumors Classification by Machine Learning and Physiological MRI Data. *Cancers.* 2022;14(10):23.
97. Bauer S, Wagner M, Seiler A, et al. Quantitative T2 '-Mapping in Acute Ischemic Stroke. *Stroke.* 2014;45(11):3280-3286.
98. Seiler A, Deichmann R, Pfeilschifter W, Singer OC, Wagner M. Oxygen-sensitive MRI in unilateral carotid high-grade occlusive disease: No relationship between signal alterations in quantitative T2' mapping and cerebral blood volume within perfusion-restricted tissue. *European Stroke Journal.* 2016;1:497.
99. Seiler A, Lauer A, Deichmann R, et al. Complete Restitution of the Ischemic Penumbra after Successful Thrombectomy A Pilot Study Using Quantitative MRI. *Clinical Neuroradiology.* 2019;29(3):415-423.
100. Stadlbauer A, Merkel A, Zimmermann M, et al. Intraoperative Magnetic Resonance Imaging of Cerebral Oxygen Metabolism During Resection of Brain Lesions. *World Neurosurgery.* 2017;100:388-394.
101. Gersing AS, Ankenbrank M, Schwaiger BJ, et al. Mapping of cerebral metabolic rate of oxygen using dynamic susceptibility contrast and blood oxygen level dependent MR imaging in acute ischemic stroke. *Neuroradiology.* 2015;57(12):1253-1261.
102. Gottler J, Kaczmarz S, Kallmayer M, et al. Flow-metabolism uncoupling in patients with asymptomatic unilateral carotid artery stenosis assessed by multi-modal magnetic resonance imaging. *Journal of Cerebral Blood Flow and Metabolism.* 2019;39:2132-2143.
103. Kaczmarz S, Gottler J, Petr J, et al. Hemodynamic impairments within individual watershed areas in asymptomatic carotid artery stenosis by multimodal MRI. *Journal of Cerebral Blood Flow and Metabolism.* 2021;41(2):380-396.
104. Kufer J, Preibisch C, Epp S, et al. Imaging effective oxygen diffusivity in the human brain with multiparametric magnetic resonance imaging. *Journal of Cerebral Blood Flow and Metabolism.* 2021.
105. Toth V, Preibisch C, Den Hollander J, Forschler A, Kooijman H, Zimmer C. MR imaging of hypoxia in brain tumors. *Interventional Neuroradiology.* 2011;1:207.
106. Geisler BS, Brandhoff F, Fiehler J, et al. Blood-oxygen-level-dependent MRI allows metabolic description of tissue at risk in acute stroke patients. *Stroke.* 2006;37(7):1778-1784.
107. Holst B, Siemonsen S, Finsterbusch J, et al. T2 ' imaging indicates decreased tissue metabolism in frontal white matter of MS patients. *Multiple Sclerosis.* 2009;15(6):701-707.
108. Reitz LY, Inglese M, Fiehler J, et al. Quantitative T2' imaging in patients with clinically isolated syndrome. *Acta Neurologica Scandinavica.* 2012;126(5):357-363.

109. Saitta L, Heese O, Forster AF, et al. Signal intensity in T2' magnetic resonance imaging is related to brain glioma grade. *European Radiology.* 2011;21(5):1068-1076.
110. Seiler A, Blockley NP, Deichmann R, et al. The relationship between blood flow impairment and oxygen depletion in acute ischemic stroke imaged with magnetic resonance imaging. *Journal of Cerebral Blood Flow and Metabolism.* 2019;39(3):454-465.
111. Winkler L, Inglese M, Fiehler J, et al. Quantitative T2'-imaging in patients with clinically isolated syndrome. *Multiple Sclerosis.* 2010;1:S104-S105.
112. Preibisch C, Shi K, Kluge A, et al. Characterizing hypoxia in human glioma: A simultaneous multimodal MRI and PET study. *NMR in Biomedicine.* 2017;30.
113. Reilander A, Pilatus U, Schure J-R, et al. Impaired oxygen extraction and adaptation of intracellular energy metabolism in cerebral small vessel disease. *Cerebral circulation - cognition and behavior.* 2023;4:100162.
114. Seiler A, Deichmann R, Pfeilschifter W, Hattingen E, Singer OC, Wagner M. T2-Imaging to Assess Cerebral Oxygen Extraction Fraction in Carotid Occlusive Disease: Influence of Cerebral Autoregulation and Cerebral Blood Volume. *Plos One.* 2016;11(8):16.
115. Wagner M, Magerkurth J, Volz S, et al. T2 '- and PASL-based perfusion mapping at 3 Tesla: influence of oxygen-ventilation on cerebral autoregulation. *Journal of Magnetic Resonance Imaging.* 2012;36(6):1347-1352.
116. An HY, Ford AL, Chen YS, et al. Defining the Ischemic Penumbra Using Magnetic Resonance Oxygen Metabolic Index. *Stroke.* 2015;46(4):982-988.
117. An HY, Sen S, Chen YS, Powers WJ, Lin WL. Noninvasive Measurements of Cerebral Blood Flow, Oxygen Extraction Fraction, and Oxygen Metabolic Index in Human with Inhalation of Air and Carbogen using Magnetic Resonance Imaging. *Translational Stroke Research.* 2012;3(2):246-254.
118. Bao DP, Zhou JH, Hao Y, et al. The Effects of Fatiguing Aerobic Exercise on the Cerebral Blood Flow and Oxygen Extraction in the Brain: A Piloting Neuroimaging Study. *Frontiers in Neurology.* 2019;10:7.
119. Cherukara MT, Stone AJ, Chappell MA, Blockley NP. Model-based Bayesian inference of brain oxygenation using quantitative BOLD. *Neuroimage.* 2019;202:11.
120. Fields ME, Guilliams KP, Ragan D, et al. Hydroxyurea reduces cerebral metabolic stress in patients with sickle cell anemia. *Blood.* 2019;133(22):2436-2444.
121. Ford AL, Chin VW, Fellah S, et al. Lesion evolution and neurodegeneration in RVCL-S: A monogenic microvasculopathy. *Neurology.* 2020;95:e1918-e1931.
122. Guilliams KP, Fields ME, Ragan DK, et al. Red cell exchange transfusions lower cerebral blood flow and oxygen extraction fraction in pediatric sickle cell anemia. *Blood.* 2018;131(9):1012-1021.
123. Sen S, An HY, Menezes P, et al. Increased Cortical Cerebral Blood Flow in Asymptomatic Human Immunodeficiency Virus-Infected Subjects. *Journal of Stroke & Cerebrovascular Diseases.* 2016;25(8):1891-1895.
124. Stone AJ, Harston GWJ, Carone D, Okell TW, Kennedy J, Blockley NP. Prospects for investigating brain oxygenation in acute stroke: Experience with a non-contrast quantitative BOLD based approach. *Human Brain Mapping.* 2019;40(10):2853-2866.

125. Fields ME, Mirro AE, Binkley MM, et al. Cerebral oxygen metabolic stress is increased in children with sickle cell anemia compared to anemic controls. *American Journal of Hematology*. 2022;97(6):682-690.
126. Sen S, An H, Sollman M, et al. Reduction in cerebral oxygen metabolism in subcortical regions may be a biomarker of cognitive decline in people living with human immunodeficiency virus. *European Journal of Neurology*. 2022;29(4):1062-1074.
127. Zheng J, Hasting MK, Zhang XD, et al. A pilot study of regional perfusion and oxygenation in calf muscles of individuals with diabetes with a noninvasive measure. *Journal of Vascular Surgery*. 2014;59(2):419-426.
128. Zheng J, Li R, Zayed MA, Yan Y, An HY, Hastings MK. Pilot study of contrast-free MRI reveals significantly impaired calf skeletal muscle perfusion in diabetes with incompressible peripheral arteries. *Vascular Medicine*. 2021;26(4):367-373.
129. Zheng J, Sorensen C, Li R, et al. Deteriorated regional calf microcirculation measured by contrast-free MRI in patients with diabetes mellitus and relation with physical activity. *Diabetes and Vascular Disease Research*. 2021;18(4).
130. Wang CY, Zhang R, Zhang XD, et al. Noninvasive measurement of lower extremity muscle oxygen extraction fraction under cuff compression paradigm. *Journal of Magnetic Resonance Imaging*. 2016;43(5):1148-1158.
131. Yin YY, Zhang YY, Gao JH. Dynamic measurement of oxygen extraction fraction using a multiecho asymmetric spin echo (MASE) pulse sequence. *Magnetic Resonance in Medicine*. 2018;80(3):1118-1124.
132. Lee H, Englund EK, Wehrli FW. Interleaved quantitative BOLD: Combining extravascular R2 ' - and intravascular R-2-measurements for estimation of deoxygenated blood volume and hemoglobin oxygen saturation. *Neuroimage*. 2018;174:420-431.
133. Waddle SL, Garza M, Ying CW, et al. Vascular space occupancy asymmetric spin echo (VASO-ASE) for non-invasive quantification of cerebral oxygen extraction fraction. *Magnetic Resonance in Medicine*. 2023;90(1):211-221.
134. Lu L, Eldeniz C, An HY, et al. Quantification of myocardial oxygen extraction fraction: A proof-of-concept study. *Magnetic Resonance in Medicine*. 2021;85(6):3318-3325.
135. An HY, Lin WL, Celik A, Lee YZ. Quantitative measurements of cerebral metabolic rate of oxygen utilization using MRI: a volunteer study. *Nmr in Biomedicine*. 2001;14(7):441-447.
136. Domsch S, Mie MB, Wenz F, Schad LR. Non-invasive multiparametric qBOLD approach for robust mapping of the oxygen extraction fraction. *Zeitschrift Fur Medizinische Physik*. 2014;24(3):231-242.
137. Domsch S, Murle B, Weingartner S, Zapp J, Wenz F, Schad LR. Oxygen extraction fraction mapping at 3 Tesla using an artificial neural network: A feasibility study. *Magnetic Resonance in Medicine*. 2018;79(2):890-899.
138. Wang ZX, Xiao JX, Xie S, et al. MR evaluation of cerebral oxygen metabolism and blood flow in stroke-like episodes of MELAS. *Journal of the Neurological Sciences*. 2012;323(1):173-177.
139. Xie S, Xiao J, Duan H, Fu L, Mo D, Zhang X. Quantitative measurement of oxygen extraction fraction by MRI in patients with cerebrovascular disease: pre- and post-surgery. *Turkish neurosurgery*. 2015;25:21-28.

140. Yu L, Xie S, Xiao JX, Wang ZX, Zhang XD. Quantitative Measurement of Cerebral Oxygen Extraction Fraction Using MRI in Patients with MELAS. *Plos One*. 2013;8(11):7.
141. Cho J, Kee Y, Spincemaille P, et al. Cerebral metabolic rate of oxygen (CMRO2) mapping by combining quantitative susceptibility mapping (QSM) and quantitative blood oxygenation level-dependent imaging (qBOLD). *Magnetic Resonance in Medicine*. 2018;80(4):1595-1604.
142. Cho J, Nguyen TD, Huang W, et al. Brain oxygen extraction fraction mapping in patients with multiple sclerosis. *Journal of Cerebral Blood Flow and Metabolism*. 2021.
143. Cho J, Spincemaille P, Nguyen TD, Gupta A, Wang Y. Temporal clustering, tissue composition, and total variation for mapping oxygen extraction fraction using QSM and quantitative BOLD. *Magnetic Resonance in Medicine*. 2021;

:12.
144. Cho J, Zhang J, Spincemaille P, et al. QQ-NET - using deep learning to solve quantitative susceptibility mapping and quantitative blood oxygen level dependent magnitude (QSM+qBOLD or QQ) based oxygen extraction fraction (OEF) mapping. *Magnetic Resonance in Medicine*. 2022;87(3):1583-1594.
145. Cho J, Zhang S, Kee Y, et al. Cluster analysis of time evolution (CAT) for quantitative susceptibility mapping (QSM) and quantitative blood oxygen level-dependent magnitude (qBOLD)-based oxygen extraction fraction (OEF) and cerebral metabolic rate of oxygen (CMRO2) mapping. *Magnetic Resonance in Medicine*. 2020;83(3):844-857.
146. Cho JH, Lee J, An HY, Goyal MS, Su Y, Wang Y. Cerebral oxygen extraction fraction (OEF): Comparison of challenge-free gradient echo QSM plus qBOLD (QQ) with O-15 PET in healthy adults. *Journal of Cerebral Blood Flow and Metabolism*. 2021;41(7):1658-1668.
147. Hubertus S, Thomas S, Cho J, Zhang S, Wang Y, Schad LR. Using an artificial neural network for fast mapping of the oxygen extraction fraction with combined QSM and quantitative BOLD. *Magnetic Resonance in Medicine*. 2019;82(6):2199-2211.
148. Wengler K, Wang JH, Sosa MS, et al. Mapping hepatic blood oxygenation by quantitative BOLD (qBOLD) MRI. *Magnetic Resonance in Medicine*. 2019;81(5):3272-3282.
149. Wu D, Zhou Y, Cho J, et al. The Spatiotemporal Evolution of MRI-Derived Oxygen Extraction Fraction and Perfusion in Ischemic Stroke. *Frontiers in Neuroscience*. 2021;15.
150. Zhang S, Cho JH, Nguyen TD, et al. Initial Experience of Challenge-Free MRI-Based Oxygen Extraction Fraction Mapping of Ischemic Stroke at Various Stages: Comparison With Perfusion and Diffusion Mapping. *Frontiers in Neuroscience*. 2020;14:11.
151. Zhao Y, Wen J, Cross AH, Yablonskiy DA. On the relationship between cellular and hemodynamic properties of the human brain cortex throughout adult lifespan. *Neuroimage*. 2016;133:417-429.
152. Baazaoui H, Hubertus S, Maros ME, et al. Artificial Neural Network-Derived Cerebral Metabolic Rate of Oxygen for Differentiating Glioblastoma and Brain Metastasis in MRI: A Feasibility Study. *Applied Sciences-Basel*. 2021;11(21):13.

153. Zhang QH, Sui CF, Cho JH, et al. Assessing Cerebral Oxygen Metabolism Changes in Patients With Preeclampsia Using Voxel-Based Morphometry of Oxygen Extraction Fraction Maps in Magnetic Resonance Imaging. *Korean Journal of Radiology.* 2023;24(4):324-337.
154. Zhuang HW, Cho JH, Chiang GCY, et al. Cerebral oxygen extraction fraction declines with ventricular enlargement in patients with normal pressure hydrocephalus. *Clinical Imaging.* 2023;97:22-27.
155. Yang L, Cho J, Chen T, et al. Oxygen extraction fraction (OEF) assesses cerebral oxygen metabolism of deep gray matter in patients with pre-eclampsia. *European Radiology.* 2022;32(9):6058-6069.
156. Chiang GC, Cho J, Dyke J, et al. Brain oxygen extraction and neural tissue susceptibility are associated with cognitive impairment in older individuals. *Journal of Neuroimaging.* 2022;32(4):697-709.
157. Ellingson BM, Woodworth DC, Leu K, Salamon N, Holly LT. Spinal Cord Perfusion MR Imaging Implicates Both Ischemia and Hypoxia in the Pathogenesis of Cervical Spondylosis. *World Neurosurgery.* 2019;128:E773-E781.
158. Oughourlian TC, Yao JW, Hagiwara A, et al. Relative oxygen extraction fraction (rOEF) MR imaging reveals higher hypoxia in human epidermal growth factor receptor (EGFR) amplified compared with non-amplified gliomas. *Neuroradiology.* 2021;63(6):857-868.
159. Lee JM, Vo KD, An HY, et al. Magnetic resonance cerebral metabolic rate of oxygen utilization in hyperacute stroke patients. *Annals of Neurology.* 2003;53(2):227-232.
160. Eker OF, Ameli R, Makris N, et al. MRI Assessment of Oxygen Metabolism and Hemodynamic Status in Symptomatic Intracranial Atherosclerotic Stenosis: A Pilot Study. *Journal of Neuroimaging.* 2019;29(4):467-475.
161. Seiler A, Deichmann R, Noth U, et al. Oxygenation-Sensitive Magnetic Resonance Imaging in Acute Ischemic Stroke Using T2 '/ R2 ' Mapping Influence of Relative Cerebral Blood Volume. *Stroke.* 2017;48(6):1671-+.
162. Qiu J, Wu K, Zhu M, et al. Using quantitative MRI to study the association of isocitrate dehydrogenase (IDH) status with oxygen metabolism and cellular structure changes in glioma. *European Journal of Radiology.* 2022;155:8.
163. Cho J, Ma Y, Spincemaille P, Pike GB, Wang Y. Cerebral oxygen extraction fraction: Comparison of dual-gas challenge calibrated BOLD with CBF and challenge-free gradient echo QSM+qBOLD. *Magn Reson Med*. 2021;85(2):953-961.
164. Blockley NP, Griffeth VEM, Germuska MA, Bulte DP, Buxton RB. An analysis of the use of hyperoxia for measuring venous cerebral blood volume: Comparison of the existing method with a new analysis approach. *NeuroImage.* 2013;72:33-40.
165. Lee H, Wehrli FW. Whole-brain 3D mapping of oxygen metabolism using constrained quantitative BOLD. *Neuroimage.* 2022;250:12.
166. Stone AJ, Blockley NP. Improving qBOLD based measures of oxygen extraction fraction using hyperoxia-BOLD derived measures of blood volume. *bioRxiv.* 2020:2020.2006. 2014.151134.
167. An H, Ford AL, Eldeniz C, et al. Magnetic resonance oxygen metabolic index distinguishes infarct from peri-infarct tissue better than adc and pwi in hyperacute ischemic stroke patients. *Stroke Conference.* 2012;43(2).

168. Wang Y, Fellah S, Fields ME, et al. Cerebral Oxygen Metabolic Stress, Microstructural Injury, and Infarction in Adults With Sickle Cell Disease. *Neurology.* 2021;97:e902-e912.
169. Hirsch NM, Toth V, Forschler A, Kooijman H, Zimmer C, Preibisch C. Technical considerations on the validity of blood oxygenation level-dependent-based MR assessment of vascular deoxygenation. *NMR in Biomedicine.* 2014;27(7):853-862.
170. Goettler J, Kaczmarz S, Zimmer C, Sorg C, Preibisch C, Hyder F. Uncoupling of cerebral blood flow and oxidative metabolism in patients with asymptomatic high-grade carotid artery stenosis assessed by multi-modal MRI. *Journal of Cerebral Blood Flow and Metabolism.* 2019;39:49-50.
171. Toth V, Forschler A, Hirsch NM, et al. MR-based hypoxia measures in human glioma. *Journal of Neuro-Oncology.* 2013;115(2):197-207.
172. Jenkinson M, Beckmann CF, Behrens TE, Woolrich MW, Smith SM. Fsl. *Neuroimage.* 2012;62(2):782-790.
173. Penny W, Ashburner J, Kiebel S, et al. Statistical parametric mapping: An annotated bibliography. Wellcome Department of Cognitive Neurology, University College London. In:2001.
174. Zheng J, An H, Coggan AR, et al. Noncontrast skeletal muscle oximetry. *Magnetic Resonance in Medicine.* 2014;71(1):318-325.
175. Guilliams K, Fieldssup ME, Ragan D, et al. Anemic hypoxia causes ischemic vulnerability in the watershed of children with sickle cell disease. *Annals of Neurology.* 2018;84:S264-S265.
176. Wharton S, Bowtell R. Fiber orientation-dependent white matter contrast in gradient echo MRI. *Proceedings of the National Academy of Sciences.* 2012;109(45):18559-18564.
177. Sati P, van Gelderen P, Silva AC, et al. Micro-compartment specific T2* relaxation in the brain. *Neuroimage.* 2013;77:268-278.
178. Wu L, Wu W, Tali ET, Yuh WT. Oligemia, penumbra, infarction: understanding hypoperfusion with neuroimaging. *Neuroimaging Clinics.* 2018;28(4):599-609.
179. An H, Ford AL, Eldeniz C, et al. Magnetic Resonance Oxygen Metabolic Index Distinguishes infarct from peri-infarct tissue better than ADC and PWI In hyperacute ischemic Stroke Patients. In: Am Heart Assoc; 2012.
180. Guadagno JV, Donnan GA, Markus R, Gillard JH, Baron J-C. Imaging the ischaemic penumbra. *Current Opinion in Neurology.* 2004;17(1):61-67.
181. Jiang D, Lin Z, Liu P, et al. Normal variations in brain oxygen extraction fraction are partly attributed to differences in end-tidal CO2. *Journal of Cerebral Blood Flow & Metabolism.* 2020;40(7):1492-1500.
182. Stone AJ, Blockley NP. Improving qBOLD based measures of brain oxygenation using hyperoxia BOLD derived measures of blood volume. Paper presented at: Proceedings of the 25th Annual Meeting of ISMRM2017.
183. Craig M, Irving B, Chappell M, Croal P, Zhao M. Quantiphyse tool Images © 2017-2019 University of Oxford
. Published 2019. Accessed.
184. Christen T, Lemasson B, Pannetier N, et al. Evaluation of a quantitative blood oxygenation level-dependent (qBOLD) approach to map local blood oxygen saturation. *NMR Biomed.* 2011;24(4):393-403.

185. Keenan KE, Ainslie M, Barker AJ, et al. Quantitative magnetic resonance imaging phantoms: a review and the need for a system phantom. *Magnetic resonance in medicine*. 2018;79(1):48-61.
186. Bane O, Hectors SJ, Wagner M, et al. Accuracy, repeatability, and interplatform reproducibility of T1 quantification methods used for DCE-MRI: results from a multicenter phantom study. *Magnetic resonance in medicine*. 2018;79(5):2564-2575.
187. Cercignani M, Dowell NG, Tofts PS. *Quantitative MRI of the brain: principles of physical measurement*. 2018.
188. Fieremans E, Lee H-H. Physical and numerical phantoms for the validation of brain microstructural MRI: A cookbook. *Neuroimage*. 2018;182:39-61.
189. Weisskoff RM, Zuo CS, Boxerman JL, Rosen BR. Microscopic susceptibility variation and transverse relaxation: theory and experiment. *Magn Reson Med*. 1994;31(6):601-610.
190. Sohlin MC, Schad LR. Susceptibility-related MR signal dephasing under nonstatic conditions: experimental verification and consequences for qBOLD measurements. *Journal of Magnetic Resonance Imaging*. 2011;33(2):417-425.
191. MRIcroGL. MRIcroGL. https://www.nitrc.org/projects/mricrogl/. Accessed 22 June 2024.
192. Prism G. *GraphPad Prism software* 10 ed. Boston, Massachusetts USA: GraphPad Software; 10.
193. Sedlacik J, Boelmans K, Löbel U, Holst B, Siemonsen S, Fiehler J. Reversible, irreversible and effective transverse relaxation rates in normal aging brain at 3 T. *Neuroimage*. 2014;84:1032-1041.
194. Lee M-J, Kim M-J, Yoon C-S, Song SY, Park K, Kim WS. The T2-shortening effect of gadolinium and the optimal conditions for maximizing the CNR for evaluating the biliary system: a phantom study. *Korean journal of radiology*. 2011;12(3):358-364.
195. Wang X, Chu X. Role of surfactant in the formation of zein/Tween-20 nanoparticles studied by fluorescence and circular dichroism. *Colloids and Surfaces A: Physicochemical and Engineering Aspects*. 2018;558:110-116.
196. Schneiders NJ. Solutions of two paramagnetic ions for use in nuclear magnetic resonance phantoms. *Medical physics*. 1988;15(1):12-16.
197. Hennig J, Nauerth A, Friedburg H. RARE imaging: a fast imaging method for clinical MR. *Magnetic resonance in medicine*. 1986;3(6):823-833.
198. Poon CS, Henkelman RM. Practical T2 quantitation for clinical applications. *Journal of Magnetic Resonance Imaging*. 1992;2(5):541-553.
199. Alzaidi AA, Panek R, Blockley NP. Quantitative BOLD (qBOLD) imaging of oxygen metabolism and blood oxygenation in the human body: A scoping review. *Magn Reson Med*. 2024.
200. Christen T, Lemasson B, Pannetier N, et al. Is T2* enough to assess oxygenation? Quantitative blood oxygen level–dependent analysis in brain tumor. *Radiology*. 2012;262(2):495-502.
201. Suri S, Bulte D, Chiesa ST, et al. Study Protocol: The Heart and Brain Study. *Frontiers in Physiology*. 2021;12.

202. Cox EF, Gowland PA. Simultaneous quantification of T2 and T' 2 using a combined gradient echo-spin echo sequence at ultrahigh field. *Magnetic resonance in medicine*. 2010;64(5):1440-1445.
203. Zhang Y, Brady M, Smith S. Segmentation of brain MR images through a hidden Markov random field model and the expectation-maximization algorithm. *IEEE transactions on medical imaging*. 2001;20(1):45-57.
204. Smith SM. Fast robust automated brain extraction. *Human brain mapping*. 2002;17(3):143-155.
205. Eichling JO, Raichle ME, Grubb Jr RL, Larson KB, Ter-Pogossian M. In vivo determination of cerebral blood volume with radioactive oxygen-15 in the monkey. *Circulation research*. 1975;37(6):707-714.
206. Jenkinson M, Bannister P, Brady M, Smith S. Improved optimization for the robust and accurate linear registration and motion correction of brain images. *Neuroimage*. 2002;17(2):825-841.
207. Lu H, Ge Y. Quantitative evaluation of oxygenation in venous vessels using T2-relaxation-under-spin-tagging MRI. *Magnetic Resonance in Medicine: An Official Journal of the International Society for Magnetic Resonance in Medicine*. 2008;60(2):357-363.
208. Lu H, Clingman C, Golay X, Van Zijl PC. Determining the longitudinal relaxation time (T1) of blood at 3.0 Tesla. *Magnetic Resonance in Medicine: an Official Journal of the International Society for Magnetic Resonance in Medicine*. 2004;52(3):679-682.
209. Peng S-L, Dumas JA, Park DC, et al. Age-related increase of resting metabolic rate in the human brain. *Neuroimage*. 2014;98:176-183.
210. Lu H, Xu F, Grgac K, Liu P, Qin Q, Van Zijl P. Calibration and validation of TRUST MRI for the estimation of cerebral blood oxygenation. *Magnetic resonance in medicine*. 2012;67(1):42-49.
211. Marchal G, Rioux P, Petit-Taboué M-C, et al. Regional cerebral oxygen consumption, blood flow, and blood volume in healthy human aging. *Archives of neurology*. 1992;49(10):1013-1020.
212. Donahue MJ, Achten E, Cogswell PM, et al. Consensus statement on current and emerging methods for the diagnosis and evaluation of cerebrovascular disease. *Journal of Cerebral Blood Flow & Metabolism*. 2017;38(9):1391-1417.
213. Kety SS, Schmidt CF. The effects of altered arterial tensions of carbon dioxide and oxygen on cerebral blood flow and cerebral oxygen consumption of normal young men. *The Journal of clinical investigation*. 1948;27(4):484-492.
214. Iscoe S, Fisher JA. Hyperoxia-induced hypocapnia: an underappreciated risk. *Chest*. 2005;128(1):430-433.
215. Xu F, Liu P, Pascual JM, Xiao G, Lu H. Effect of hypoxia and hyperoxia on cerebral blood flow, blood oxygenation, and oxidative metabolism. *Journal of Cerebral Blood Flow & Metabolism*. 2012;32(10):1909-1918.
216. Ito H, Kanno I, Ibaraki M, Hatazawa J, Miura S. Changes in human cerebral blood flow and cerebral blood volume during hypercapnia and hypocapnia measured by positron emission tomography. *Journal of Cerebral Blood Flow & Metabolism*. 2003;23(6):665-670.

## Appendices

### Appendix (A)

Database search strategy (Embase)

| | |
|---|---|
| 1 | (oxygen adj3 (extraction or saturation or metabolism)).ti,ab. |
| 2 | (qbold or quantitative bold).ti,ab. |
| 3 | MR_OEF.ti,ab. |
| 4 | (mri or "mr imaging" or "magnetic resonance" or "mr measurement*").ti,ab. |
| 5 | 1 and 4 |
| 6 | 2 or 3 |
| 7 | 5 or 6 |
| 8 | limit 7 to (english language and yr="1994 -Current") |

**Appendix (B)**

## Standard Operating Procedure (SOP)

Hydroxyethyl-cellulose (HEC) phantoms
Procedure to be followed:
1.Bring a beaker, add the water (80 ml) and put it on the hot plate (DO NOT turn the heat On)
2. put the magnetic stirrer inside the beaker
3.Add first NaCl (0.62g) to the water
4.Afterwards under rigorous stirring slowly add the HEC (2.48g).
5.After 10 mins add slowly glass beads every tube has different Beads fractions
(See excel sheet)

- Beads fractions >> expected $R_2$'
    - 0.1 % beads =0.0160 g. >> 2.822
    - 0.2 % beads = 0.0320. >> 4.799
    - 0.3% beads = 0.0481 >> 6.777
    - 0.4 % beads = 0.0642 >> 8.754
    - 0.5 % beads = 0.0804 >> 10.732
    - 0.6 % beads = 0.0965 >> 12.709
    - 1% % beads = 0.1616 >> 20.691
- Also make tubes with 0 beads

6.Stir for (5-10) mins or until the solution clears and thickens.
7.Pour the gel in the tubes.